INTERNATIONAL RELATIVISTIC ASTROPHYSICS IRAP Ph.D.
ERASMUS MUNDUS PROGRAM

Finite Temperature Effects in the White Dwarf Structure and Neutron Star Cooling in General Relativity

Thesis Advisor
Prof. Jorge Armando Rueda

Ph.D. Student
Sheyse Martins de Carvalho

Sapienza University of Rome Academic Year 2010–2013

Contents

List of Figures

List of Tables

Chapter 1

Introduction

This thesis is in the context of the physics astrophysics of compact stars. In this work we explore in particular the thermal properties of white dwarfs and neutron stars.

As we will show in chapter 3, the mass-radius relation of white dwarfs in the zero-temperature approximation deviates considerably for masses $\lesssim$ 0.7–0.8 $M_\odot$ (see Fig. 3.1). Since the central densities of these white dwarfs are $\lesssim 10^7$ g cm^{-3}, where the degenerate approximation breaks down, it is natural to expect that such deviations are the result of neglecting finite temperature effects. In addition, relativistic binaries formed by a neutron star and an ultra-low mass white dwarf with masses $\lesssim 0.2M_\odot$ have been recently discovered, which are the perfect arena to test the equation of state of white dwarf matter. Thus, besides being interesting on their own, the finite temperature effects on the equation of state and consequently on the mass-radius relation of the white dwarf are very important. In this work, besides to the Coulomb and special relativity effects, we consider also finite temperature in the white dwarf equation of state and use it to construct equilibrium configurations of non-zero temperature white dwarfs.

Turning to neutron stars, it is known that their cooling evolution could reveal crucial information on the properties of matter at high density and pressure. So, the modelling of the thermal structure evolution together with its observation allow us, in a unique manner, to probe the microscopical and macroscopical properties of neutron stars. This in turn might help us to understand better, for example, the phase diagram of baryonic matter. This happens because the observed properties of

neutron stars (mass, radius, rotation velocity, thermal evolution, etc.) are extremely sensitive to the star's composition. In this way, taking into account the analysis of these properties, it is possible to constrain the equation of state of dense matter and its composition. In particular, in this thesis we explore a new model for the inner structure of neutron stars formulated by Belvedere et al. (2012), where it is considered the condition of global charge neutrality of the neutron star instead of local charge neutrality, which as will see significantly changes the star's structure and composition.

Therefore, we divided the thesis in two parts. In the first part of the work we construct the equation of state of white dwarfs in the case of finite temperatures and obtain the white dwarf mass-radius relation by integrating the hydrostatic equilibrium equations. In the chapter 2, we briefly review the most known approaches to model the equation of state of white dwarfs and the relativistic generalization of the Feynman-Metropolis-Teller treatment presented by Rotondo et al. (2011). We describe the extension of this latter treatment to finite temperatures in the chapter 3, where we present the results of the numerical integration of the equations and describe the general properties of the new equation of state. We also construct the mass-radius relation of white dwarfs and apply the results to the description of the ultra-low mass white dwarf orbiting the pulsar PSR J1738+0333.

The second part of the work consists in computing the thermal evolution of the globally neutral neutron stars and to compare them with the locally neutral neutron star cooling curves. So, the second part of the thesis is divided in three chapters. In the chapter 4 we present a introduction about the new treatment of neutron stars, formulated by Belvedere et al.(2012), which fulfills global and not local charge neutrality. We point out there the differences between the structure of the globally neutral neutron star and the locally one. The thermal evolution equations are presented in the chapter 5, and all the main regulators of the cooling theory are also discussed: the neutrino emission processes, the heat capacity and thermal conductivity. Finally, in chapter 6 the details about the cooling stages and the results of our cooling simulations of the globally neutral neutron star are presented. We show the cooling curves considering the isothermal approximation and considering the full

cooling theory, comparing with the observed data taken from Yakovlev et al. (2004).

Chapter 2

The Relativistic FMT treatment for degenerate White Dwarf

In 1926, it was shown that the electrons obey what is now called Fermi-Dirac statistics. Fowler (1926) [9] then, realized that the pressure supporting the white dwarfs against gravity could be supplied by degenerate electrons. This pressure remains even at zero temperatures, due to zero-point motion. This lead to the concept of degenerate stars.

Noticing that at the extreme densities of white dwarfs the velocities of the electrons must become relativistic, Anderson (1929) and Stoner (1930) [10] calculated relativistic corrections to Fowler's equation of state. In 1931, Chandrasekhar [11] discovered that the relativistic "softening" of this equation of state leads to the existence of a limiting mass, now called the "Chandrasekhar limit", over which gravitational forces overwhelm the pressure support, and no stable white dwarfs can exist. Landau [12]arrived, independently, to the same conclusion in 1932. Some of the basic assumptions adopted by Chandrasekhar and Landau in their idealized approach, such as the treatment of the electron as a free gas without taking into account the electromagnetic interactions, as well as the stability of the distribution of the nuclei against the gravitational interaction led to some criticisms by Eddington [13].

Kathori (1931,1936,1938) studied the effects of Coulomb interactions on the equation of state and the structure of non-relativistic white dwarfs. Auluck and Mathur (1959) extended this work by including exchange and correlation effects. Kirzhnits

(1960) presented that the matter in white dwarfs should be in a condensate state and Abrikosov (1961,1962) computed the properties of this crystal lattice phase. In 1961, Salpeter [8] provided a comprehensive discussion of the equation of state, presenting results for energy and pressure of zero-temperature plasma, identifying the Coulomb contributions. He followed an idea originally proposed by Frenkel [14]; to adopt in the study of white dwarfs the concept of a Wigner Seitz cell. Salpeter introduced to the lattice model of a pointlike nucleus surrounded by a uniform cloud of electrons, corrections due to the nonuniformity of the the electron distribution. In this way Salpeter obtained an analytic formula for the total energy in a Wigner Seitz cell and derived the corresponding equation of state of matter composed by such cells, pointing out explicity the relevance of the Coulomb interaction.

The consequences of Coulomb interactions, int the determination of the mass and radius of white dwarfs, was studied in a subsequent paper by Hamada and Salpeter [7] by using the equation of state constructed in [8]. They found that the critical mass of white dwarfs depends in a nontrivial way on the specific nuclear composition: the critical mass of Chandrasekhar-Landau which depends only on the mass to charge ratio of nuclei A/Z, now depends also on the proton number Z.

An alternative approach to the Salpeter treatment of a compressed atom was reconsidered in [15] by applying for the first time to white dwarfs a relativistic Thomas-Fermi treatment of the compressed atom introducing a finite size nucleus within a phenomenological description [16].

The study of compressed atom was revisited in [1] by extending the approach of Feynman, Metropolis and Teller [17] taking into account weak interactions. This treatment takes into account also all the Coulomb contributions duly expressed relativistically without the need of any piecewise description. The relativistic Thomas-Fermi model has been solved by imposing in addition to the electromagnetic interaction also the weak equilibrium between neutrons, protons and electrons self-consistently.

In this chapter we review the most known approaches to model the equation of state and the relativistic generalization of the Feynman-Metropolis-Teller (FMT) treatment presented by Rotondo et al. 2012 [1]. The main of this chapter is to give

a introduction and motivation for the work presented in the chapter 3 where we extended the relativistic FMT treatment to the case with finite temperatures.

2.1 The Equation of State

The equation of state (hereafter EOS) tell us the relationship between pressure and energy, and is fundamental to determining the macroscopic properties of the star. There exists a large variety of approaches to model the equation of state of white dwarf matter, each one characterized by a different way of treating or neglecting the Coulomb interaction inside each Wigner-Seitz cell, which we will briefly review here in order to construct the idea of the relativistic Feynman-Metropolis-Teller (FMT) treatment, that are been used for us.

2.1.1 The Uniform Approximation

In the uniform approximation, the electron distribution as well as the nucleons are assumed to be locally constant and therefore the condition of local charge neutrality

$$n_e = \frac{Z}{A_r} n_N \,, \tag{2.1}$$

where A_r is the average atomic weight of the nucleus, is applied. Here n_N denotes the nucleon number density and Z is the number of protons of the nucleus. The electrons are considered as a fully degenerate free-gas and then described by Fermi-Dirac statistics. Thus, their number density n_e is related to the electron Fermi-momentum P_e^F by

$$n_e = \frac{(P_e^F)^3}{3\pi^2\hbar^3} \,, \tag{2.2}$$

and the total electron energy-density and electron pressure are given by

$$\begin{aligned}
\mathcal{E}_e &= \frac{2}{(2\pi\hbar)^3}\int_0^{P_e^F}\sqrt{c^2p^2+m_e^2c^4}\,4\pi p^2dp \\
&= \frac{m_e^4c^5}{8\pi^2\hbar^3}[x_e\sqrt{1+x_e^2}(1+2x_e^2)-\operatorname{arcsinh}(x_e)]\,, \qquad (2.3)\\
P_e &= \frac{1}{3}\frac{2}{(2\pi\hbar)^3}\int_0^{P_e^F}\frac{c^2p^2}{\sqrt{c^2p^2+m_e^2c^4}}4\pi p^2dp \\
&= \frac{m_e^4c^5}{8\pi^2\hbar^3}[x_e\sqrt{1+x_e^2}(2x_e^2/3-1) \\
&+ \operatorname{arcsinh}(x_e)]\,, \qquad (2.4)
\end{aligned}$$

where we have introduced the dimensionless Fermi momentum $x_e = P_e^F/(m_ec)$ with m_e the electron rest-mass.

The kinetic energy of nucleons is neglected and therefore the pressure is assumed to be only due to electrons. Thus the equation of state can be written as

$$\begin{aligned}
\mathcal{E}_{\text{unif}} &= \mathcal{E}_N+\mathcal{E}_e \approx \frac{A_r}{Z}M_uc^2n_e+\mathcal{E}_e\,, \qquad (2.5)\\
P_{\text{unif}} &\approx P_e\,, \qquad (2.6)
\end{aligned}$$

where $M_u = 1.6604\times10^{-24}$ g is the unified atomic mass and $\mathcal{E}_e$ and P_e are given by Eqs. (2.3)–(2.4).

Within this approximation, the total self-consistent chemical potential is given by

$$\mu_{\text{unif}} = A_rM_uc^2+Z\mu_e\,, \qquad (2.7)$$

where

$$\mu_e = \frac{\mathcal{E}_e+P_e}{n_e} = \sqrt{c^2(P_e^F)^2+m_e^2c^4}\,, \qquad (2.8)$$

is the electron free-chemical potential.

As a consequence of this effective approach which does not take into any account the Coulomb interaction, it is obtained an effective one-component electron-nucleon fluid approach where the kinetic pressure is given by electrons of mass m_e and their gravitational contribution is given by an effective mass $(A_r/Z)M_u$ attached to each electron (see e.g. [18]). This is even more evident when the electron contribution to the energy-density in Eq. (2.5) is neglected and therefore the energy-density is

attributed only to the nuclei. Within this approach followed by Chandrasekhar [11], the equation of state reduces to

$$\mathcal{E}_{\rm Ch} = \frac{A_r}{Z} M_u c^2 n_e \,, \tag{2.9}$$

$$P_{\rm Ch} = P_{\rm unif} = P_e \,. \tag{2.10}$$

2.1.2 The lattice model

The first correction to the above uniform model, corresponds to abandon the assumption of the electron-nucleon fluid through the so-called "lattice" model which introduces the concept of Wigner-Seitz cell: each cell contains a point-like nucleus of charge $+Ze$ with A nucleons surrounded by a uniformly distributed cloud of Z fully-degenerate electrons. The global neutrality of the cell is guaranteed by the condition

$$Z = V_{\rm ws} n_e = \frac{n_e}{n_{\rm ws}} \,, \tag{2.11}$$

where $n_{\rm ws} = 1/V_{\rm ws}$ is the Wigner-Seitz cell density and $V_{\rm ws} = 4\pi R_{\rm ws}^3/3$ is the cell volume.

The total energy of the Wigner-Seitz cell is modified by the inclusion of the Coulomb energy, i.e

$$E_{\rm L} = \mathcal{E}_{\rm unif} V_{\rm ws} + E_C \,, \tag{2.12}$$

being

$$E_C = E_{e-N} + E_{e-e} = -\frac{9}{10}\frac{Z^2 e^2}{R_{\rm ws}} \,, \tag{2.13}$$

where $\mathcal{E}_{\rm unif}$ is given by Eq. (2.5) and E_{e-N} and E_{e-e} are the electron-nucleus and the electron-electron Coulomb energies

$$E_{e-N} = -\int_0^{R_{\rm ws}} 4\pi r^2 \left(\frac{Ze}{r}\right) e n_e dr$$

$$= -\frac{3}{2}\frac{Z^2 e^2}{R_{\rm ws}} \,, \tag{2.14}$$

$$E_{e-e} = \frac{3}{5}\frac{Z^2 e^2}{R_{\rm ws}} \,. \tag{2.15}$$

The self-consistent pressure of the Wigner-Seitz cell is then given by

$$P_{\rm L} = -\frac{\partial E_{\rm L}}{\partial V_{\rm ws}} = P_{\rm unif} + \frac{1}{3}\frac{E_C}{V_{\rm ws}} \,, \tag{2.16}$$

where $P_{\rm unif}$ is given by Eq. (2.6). It is worth to recall that the point-like assumption of the nucleus is incompatible with a relativistic treatment of the degenerate electron fluid (see [19, 20] for details). Such an inconsistency has been traditionally ignored by applying, within a point-like nucleus model, the relativistic formulas (2.3) and (2.4) and their corresponding ultrarelativistic limits (see e.g. [8]).

The Wigner-Seitz cell chemical potential is in this case

$$\mu_{\rm L} = E_{\rm L} + P_{\rm L} V_{\rm ws} = \mu_{\rm unif} + \frac{4}{3} E_C \,. \tag{2.17}$$

By comparing Eqs. (2.6) and (2.16) we can see that the inclusion of the Coulomb interaction results in a decreasing of the pressure of the cell due to the negative lattice energy E_C.

2.1.3 Salpeter approach

A further development to the lattice model came from Salpeter [8] who studied the corrections due to the non-uniformity of the electron distribution inside a Wigner-Seitz cell.

Following the Chandrasekhar [11] approximation, Salpeter also neglects the electron contribution to the energy-density. Thus, the first term in the Salpeter formula for the energy of the cell comes from the nuclei energy (2.9). The second contribution is given by the Coulomb energy of the lattice model (2.13). The third contribution is obtained as follows: the electron density is assumed as $n_e[1+\epsilon(r)]$, where $n_e = 3Z/(4\pi R_{\rm ws}^3)$ is the average electron density as given by Eq. (2.11), and $\epsilon(r)$ is considered infinitesimal. The Coulomb potential energy is assumed to be the one of the point-like nucleus surrounded by a uniform distribution of electrons, so the correction given by $\epsilon(r)$ on the Coulomb potential is neglected. The electron distribution is then calculated at first-order by expanding the relativistic electron kinetic energy

$$\begin{aligned} \epsilon_k &= \sqrt{[cP_e^F(r)]^2 + m_e^2 c^4} - m_e c^2 \\ &= \sqrt{\hbar^2 c^2 (3\pi^2 n_e)^{2/3} [1+\epsilon(r)]^{2/3} + m_e^2 c^4} \\ &- m_e c^2, \end{aligned} \tag{2.18}$$

about its value in the uniform approximation

$$\epsilon_k^{\rm unif} = \sqrt{\hbar^2 c^2 (3\pi^2 n_e)^{2/3} + m_e^2 c^4} - m_e c^2 \,, \tag{2.19}$$

considering as infinitesimal the ratio eV/E_e^F between the Coulomb potential energy eV and the electron Fermi energy

$$E_e^F = \sqrt{[cP_e^F(r)]^2 + m_e^2 c^4} - m_e c^2 - eV \,. \tag{2.20}$$

The influence of the Dirac electron-exchange correction [21] on the equation of state was also considered by Salpeter [8]. However, adopting the general approach of Migdal et al. [22], it has been shown that these effects are negligible in the relativistic regime [1]. We will then consider here only the major correction of the Salpeter treatment.

The total energy of the Wigner-Seitz cell is then given by (see [8] for details)

$$E_{\rm S} = E_{\rm Ch} + E_{\rm C} + E_S^{TF} \,, \tag{2.21}$$

being

$$E_S^{TF} = -\frac{162}{175}\left(\frac{4}{9\pi}\right)^{2/3} \alpha^2 Z^{7/3} \mu_e \,, \tag{2.22}$$

where $E_{\rm Ch} = \mathcal{E}_{\rm Ch} V_{\rm ws}$, E_C is given by Eq. (2.13), μ_e is given by Eq. (2.8), and $\alpha = e^2/(\hbar c)$ is the fine structure constant.

Correspondingly, the self-consistent pressure of the Wigner-Seitz cell is

$$P_{\rm S} = P_{\rm L} + P_{TF}^S \,, \tag{2.23}$$

where

$$P_{TF}^S = \frac{1}{3}\left(\frac{P_e^F}{\mu_e}\right)^2 \frac{E_S^{TF}}{V_{\rm ws}} \,. \tag{2.24}$$

The Wigner-Seitz cell chemical potential can be then written as

$$\mu_{\rm S} = \mu_{\rm L} + E_{TF}^S \left[1 + \frac{1}{3}\left(\frac{P_e^F}{\mu_e}\right)^2\right] \,. \tag{2.25}$$

From Eqs. (2.23) and (2.25), we see that the inclusion of each additional Coulomb correction results in a further decreasing of the pressure. The Salpeter approach is

very interesting in identifying piecewise Coulomb contribution to the total energy, to the total pressure and, to the Wigner-Seitz chemical potential. However, it does not have the full consistency of the global solutions obtained with the Feynman-Metropolis-Teller approach [17] and its generalization to relativistic regimes [1] which we will discuss in detail below.

2.1.4 The classic Feynman-Metropolis-Teller treatment

Feynman, Metropolis and Teller [17] showed how to derive the equation of state of matter at high pressures by considering a Thomas-Fermi model confined in a Wigner-Seitz cell of radius $R_{\rm ws}$.

The Thomas-Fermi equilibrium condition for degenerate non-relativistic electrons in the cell is expressed by

$$E_e^F = \frac{(P_e^F)^2}{2m_e} - eV = \text{constant} > 0\,, \tag{2.26}$$

where V denotes the Coulomb potential and E_e^F denotes the Fermi energy of electrons, which is positive for configurations subjected to external pressure, namely, for compressed cells.

Defining the function $\phi(r)$ by $eV(r) + E_e^F = e^2 Z\phi(r)/r$, and introducing the dimensionless radial coordinate η by $r = b\eta$, where $b = (3\pi)^{2/3}(\lambda_e/\alpha)2^{-7/3}Z^{-1/3}$, being $\lambda_e = \hbar/(m_e c)$ the electron Compton wavelength; the Poisson equation from which the Coulomb potential V is calculated self-consistently becomes

$$\frac{d^2\phi(\eta)}{d\eta^2} = \frac{\phi(\eta)^{3/2}}{\eta^{1/2}}\,. \tag{2.27}$$

The boundary conditions for Eq. (2.27) follow from the point-like structure of the nucleus $\phi(0) = 1$ and, from the global neutrality of the Wigner-Seitz cell $\phi(\eta_0) = \eta_0 d\phi/d\eta|_{\eta=\eta_0}$, where η_0 defines the dimensionless radius of the Wigner-Seitz cell by $\eta_0 = R_{\rm ws}/b$.

For each value of the compression, e.g. η_0, it corresponds a value of the electron Fermi energy E_e^F and a different solution of Eq. (2.27), which determines the self-consistent Coulomb potential energy eV as well as the self-consistent electron

distribution inside the cell through

$$n_e(\eta) = \frac{Z}{4\pi b^3}\left[\frac{\phi(\eta)}{\eta}\right]^{3/2} . \tag{2.28}$$

In the non-relativistic Thomas-Fermi model, the total energy of the Wigner-Seitz cell is given by (see [23, 17] for details)

$$E_{\rm ws} = E_N + E_k^{(e)} + E_C\,, \tag{2.29}$$

being

$$\begin{aligned} E_N &= M_N(Z,A)c^2\,, & (2.30)\\ E_k^{(e)} &= \int_0^{R_{\rm ws}} 4\pi r^2 \mathcal{E}_e[n_e(r)]dr \\ &= \frac{3}{7}\frac{Z^2e^2}{b}\left[\frac{4}{5}\eta_0^{1/2}\phi^{5/2}(\eta_0) - \phi'(0)\right]\,, & (2.31)\\ E_C &= E_{e-N} + E_{e-e} \\ &= -\frac{6}{7}\frac{Z^2e^2}{b}\left[\frac{1}{3}\eta_0^{1/2}\phi^{5/2}(\eta_0) - \phi'(0)\right]\,, & (2.32) \end{aligned}$$

where $M_N(Z,A)$ is the nucleus mass, $\mathcal{E}_e[n_e(r)]$ is given by Eq. (2.3) and E_{e-N} and E_{e-e} are the electron-nucleus Coulomb energy and the electron-electron Coulomb energy, which are given by

$$\begin{aligned} E_{e-N} &= -\int_0^{R_{\rm ws}} 4\pi r^2 \left(\frac{Ze}{r}\right) e n_e(r) dr\,, & (2.33)\\ E_{e-e} &= \frac{1}{2}\int_0^{R_{\rm ws}} 4\pi r^2 e n_e(\vec{r}) dr \\ &\times \int_0^{R_{\rm ws}} 4\pi r'^2 \frac{e n_e(\vec{r}')}{|\vec{r}-\vec{r}'|} dr' . & (2.34) \end{aligned}$$

From Eqs. (2.31) and (2.32) we recover the well-known relation between the total kinetic energy and the total Coulomb energy in the Thomas-Fermi model [23, 17]

$$E_k^{(e)} = E_k^{\rm unif}[n_e(R_{\rm ws})] - \frac{1}{2}E_C\,, \tag{2.35}$$

where $E_k^{\rm unif}[n_e(R_{\rm ws})]$ is the non-relativistic kinetic energy of a uniform electron distribution of density $n_e(R_{\rm ws})$, i.e.

$$E_k^{\rm unif}[n_e(R_{\rm ws})] = \frac{3}{5}Z^*\mu_e(R_{\rm ws})\,, \tag{2.36}$$

with Z^* defined by

$$Z^* = V_{\rm ws} n_e(R_{\rm ws})\,, \tag{2.37}$$

and $\mu_e(R_{\rm ws}) = \hbar^2[3\pi^2 n_e(R_{\rm ws})]^{2/3}/(2m_e)$.

The self-consistent pressure of the Wigner-Seitz cell given by the non-relativistic Thomas-Fermi model is (see [23, 17] for details)

$$P_{\rm TF} = \frac{2}{3}\frac{E_k^{\rm unif}[n_e(R_{\rm ws})]}{V_{\rm ws}}\,. \tag{2.38}$$

The pressure of the Thomas-Fermi model (2.38) is equal to the pressure of a free-electron distribution of density $n_e(R_{\rm ws})$. Being the electron density inside the cell a decreasing function of the distance from the nucleus, the electron density at the cell boundary, $n_e(R_{\rm ws})$, is smaller than the average electron distribution $3Z/(4\pi R_{\rm ws}^3)$. Then, the pressure given by (2.38) is smaller than the one given by the non-relativistic version of Eq. (2.4) of the uniform model of Subsec. 2.1.1. Such a smaller pressure, although faint fully given by the expression of a free-electron gas, contains in a self-consistent fashion all the Coulomb effects inside the Wigner-Seitz cell.

The chemical potential of the Wigner-Seitz cell of the non-relativistic Thomas-Fermi model can be then written as

$$\mu_{\rm TF} = M_N(Z,A)c^2 + Z^*\mu_e(R_{\rm ws}) + \frac{1}{2}E_C\,, \tag{2.39}$$

where we have used Eqs. (2.35)–(2.37).

Integrating by parts the total number of electrons

$$Z = \int_0^{R_{\rm ws}} 4\pi r^2 n_e(r)dr = Z^* + I(R_{\rm ws})\,, \tag{2.40}$$

where

$$I(R_{\rm ws}) = \int_0^{R_{\rm ws}} \frac{4\pi}{3} r^3 \frac{\partial n_e(r)}{\partial r} dr\,, \tag{2.41}$$

we can rewrite finally the following semi-analytical expression of the chemical potential (2.39) of the cell

$$\begin{aligned}\mu_{\rm TF} &= M_N(Z,A)c^2 + Z\mu_e^{\rm unif}\left[1+\frac{I(R_{\rm ws})}{Z}\right]^{2/3} \\ &+ \mu_e^{\rm unif} I(R_{\rm ws})\left[1+\frac{I(R_{\rm ws})}{Z}\right]^{2/3} + \frac{1}{2}E_C\,,\end{aligned} \tag{2.42}$$

where $\mu_e^{\rm unif}$ is the electron free-chemical potential (2.8) calculated with the average electron density, namely, the electron chemical potential of the uniform approximation. The function $I(R_{\rm ws})$ depends explicitly on the gradient of the electron density, i.e. on the non-uniformity of the electron distribution.

In the limit of absence of Coulomb interaction both the last term and the function $I(R_{\rm ws})$ in Eq. (2.42) vanish and therefore in this limit $\mu_{\rm TF}$ reduces to

$$\mu_{\rm TF} \to \mu_{\rm unif}\,, \tag{2.43}$$

where $\mu_{\rm unif}$ is the chemical potential in the uniform approximation given by Eq. (2.7).

2.1.5 The relativistic Feynman-Metropolis-Teller treatment

We briefly describe now the relativistic generalization of the classic FMT treatment of compressed atoms recently achieved in [1]. One of the main differences is that, in order to allow for the presence of a cloud of relativistic electrons (see e.g. [19, 20]), the point-like nucleus approximation must be abandoned. The relativistic equilibrium condition of compressed atoms for the degenerate case is expressed by

$$E_e^F = \sqrt{c^2(P_e^F)^2 + m_e^2c^4} - m_e^2c^2 - eV(r) = \text{constant} > 0, \tag{2.44}$$

where V denotes the Coulomb potential, P_e^F is the electron Fermi momentum and E_e^F denotes the Fermi energy of electrons. In Ref. [1], we adopted a constant distribution of protons confined in a radius $R_c = \Delta\lambda_\pi Z^{\frac{1}{3}}$, where $\lambda_\pi = \hbar/(m_\pi c)$ is the pion Compton wavelength, with m_π the pion rest mass, and Z is the number of protons. The parameters Δ is such that at nuclear density, $\Delta \approx (r_0/\lambda_\pi)(A/Z)^{1/3}$, where $r_0 \approx 1.2$ fm and A is the atomic weight; so in the case of ordinary nuclei $\Delta \approx 1$. The proton density can be then written as

$$n_p(r) = \frac{Z}{\frac{4}{3}\pi R_c^3}\theta(r - R_c), \tag{2.45}$$

where $\theta(r - R_c)$ is the Heaviside function centered at the core/nucleus radius, $r = R_c$. The electron density follows from Fermi-Dirac statistics and is given by

$$n_e(r) = \frac{(P_e^F)^3}{3\pi^2\hbar^3} = \frac{1}{3\pi^2\hbar^3c^3}[\hat{V}^2(r) + 2m_ec^2\hat{V}(r)]^{\frac{3}{2}}, \tag{2.46}$$

where $\hat{V} = e\hat{V} + E_e^F$ and we have used the equilibrium condition (2.44).

By introducing the dimensionless quantities $x = r/\lambda_\pi$, $x_c = R_c/\lambda_\pi$, $\chi/r = \hat{V}(r)/(\hbar c)$ and replacing the particle densities into the Poisson Equation

$$\nabla^2 V = 4\pi e(n_p - n_e), \tag{2.47}$$

we obtain the relativistic Thomas-Fermi equation

$$\frac{1}{3x}\frac{d^2\chi(x)}{dx^2} = -\frac{\alpha}{\Delta^3}\theta(x_c - x) + \frac{4\alpha}{9\pi}\left[\frac{\chi^2(x)}{x^2} + \frac{2m_e}{m_\pi}\frac{\chi(x)}{x}\right]^{\frac{3}{2}}. \tag{2.48}$$

The above differential equation has to be integrated subjected to the boundary conditions

$$\chi(0) = 0, \quad \left.\frac{d\chi}{dx}\right|_{x=0} > 0, \quad \left.\frac{d\chi}{dx}\right|_{x=x_{\rm WS}} = \frac{\chi(x_{\rm WS})}{x_{\rm WS}}, \tag{2.49}$$

where the latter condition ensures the global charge neutrality at the Wigner-Seitz cell radius $R_{\rm WS}$, and $x_{\rm WS} = R_{\rm WS}/\lambda_\pi$ is the dimensionless cell radius.

The total energy of the Wigner-Seitz cell can be written as the sum of three contributions

$$E_{\rm WS} = E_N + E_k + E_C, \tag{2.50}$$

where

$$E_N = M_N(A, Z)c^2, \tag{2.51}$$

$$E_k = \int_0^{R_{\rm WS}} 4\pi r^2(\mathcal{E}_e - m_e n_e)dr, \tag{2.52}$$

$$E_C = \frac{1}{2}\int_{R_c}^{R_{\rm WS}} 4\pi r^2 e[n_p(r) - n_e(r)]V(r)dr, \tag{2.53}$$

are the nucleus, kinetic, and Coulomb energy of the cell. For the nucleus mass, $M_N(A, Z)$, we adopt experimental values, and $\mathcal{E}_e$ is the electron energy density

$$\begin{aligned}\mathcal{E}_e &= \frac{2}{(2\pi\hbar)^3}\int_0^{P_e^F}\sqrt{c^2p^2 + m_e^2c^4}\,4\pi p^2 dp, \\ &= \frac{m_e^4c^5}{8\pi^2\hbar^3}[x_e\sqrt{1 + x_e^2}(1 + 2x_e^2) - \operatorname{arcsinh}(x_e)],\end{aligned} \tag{2.54}$$

where we have avoided double-counting of the electrons rest-energy and the nucleus Coulomb energy which are already accounted for in the experimental values of nuclear masses.

The total pressure at the border of the Wigner-Seitz cell is exerted only by the relativistic degenerate electron gas

$$P_{\rm FMT}^{\rm rel} = \frac{1}{3}\frac{2}{(2\pi\hbar)^3}\int_0^{P_e^{F,\rm WS}} \frac{c^2p^2}{\sqrt{c^2p^2+m_e^2c^4}} 4\pi p^2 dp,$$
$$= \frac{m_e^4c^5}{8\pi^2\hbar^3}[x_e\sqrt{1+x_e^2}(2x_e^2/3-1)+\operatorname{arcsinh}(x_e)] \tag{2.55}$$

where $x_e = P_e^{F,\rm WS}/(m_ec) \equiv P_e^F(R_{\rm WS})/(m_ec)$ is the dimensionless electron Fermi momentum, often called relativistic parameter, evaluated at the radius of the Wigner-Seitz cell, $R_{\rm WS}$.

No analytic expression of the Wigner-Seitz cell chemical potential can be given in this case, so we only write its general expression

$$\mu_{\rm FMT}^{\rm rel} = E_{\rm FMT}^{\rm rel} + P_{\rm FMT}^{\rm rel} V_{\rm ws}\,, \tag{2.56}$$

where $E_{\rm FMT}^{\rm rel}$ and $P_{\rm FMT}^{\rm rel}$ are given by Eqs. (3.7) and (2.55) respectively. The above equation, contrary to the non-relativistic formula (2.39), in no way can be simplified in terms of its uniform counterparts. However, it is easy to check that, in the limit of no Coulomb interaction $n_e(R_{\rm ws}) \to 3Z/(4\pi R_{\rm ws}^3)$, $E_C \to 0$, and $E_k \to \mathcal{E}_{\rm Ch}V_{\rm ws}$ and, neglecting the nuclear binding and the proton-neutron mass difference, we finally obtain

$$\mu_{\rm FMT}^{\rm rel} \to \mu_{\rm unif}\,, \tag{2.57}$$

as it should be expected.

In Fig. 2.1 we see how the relativistic generalization of the Feynman-Metropolis-Teller treatment leads to electron density distributions markedly different from the constant electron density approximation. The electron distribution is far from being uniform as a result of the solution of Eq. (2.48), which takes into account the electromagnetic interaction between electrons and between the electrons and the finite sized nucleus. Additional details are given in [1].

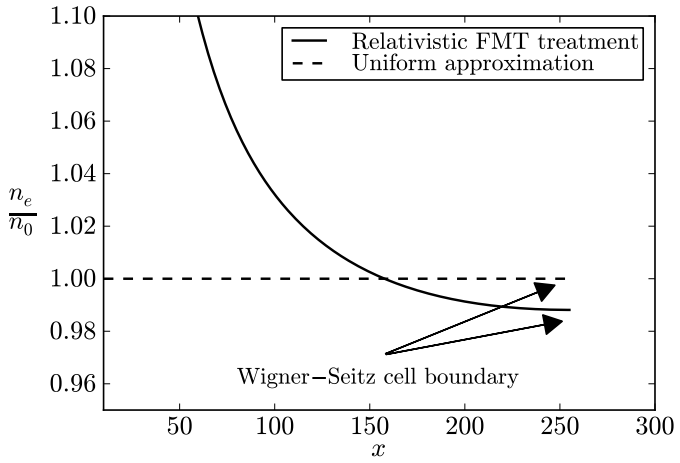

Figure 2.1: The electron number density n_e in units of the average electron number density $n_0 = 3Z/(4\pi R_{\rm ws}^3)$ inside a Wigner-Seitz cell of ^{12}C. The dimensionless radial coordinate is $x = r/\lambda_\pi$ and Wigner-Seitz cell radius is $x_{\rm ws} \approx 255$ corresponding to a density of $\sim 10^8$ g/cm^3. The solid curve corresponds to the relativistic Feynman-Metropolis-Teller treatment and the dashed curve to the uniform approximation. The electron distribution for different levels of compression as well as for different nuclear compositions can be found in [1].

2.2 Mass-Radius Relation

In this section we present the gravitational equilibrium of white dwarfs using the relativistic generalization of the FMT approach presented in the section 2.1.5. The semi realistic formula for the radius of a white dwarf in terms of its mass can be derived by balancing the degeneracy pressure of the electrons against the gravitational pressure from the nucleon mass.

Assuming the spherically symmetric metric

$$ds^2 = e^{\nu(r)}c^2dt^2 - e^{\lambda(r)}dr^2 - r^2d\theta^2 - r^2\sin^2\theta d\varphi^2\,, \tag{2.58}$$

the entire system of equations describing the equilibrium of white dwarf, taking account the weak, the electromagnetic, gravitational interactions and quantum statistics, all expressed consistently in general relativistic is given by [1]

$$\sqrt{g_{00}}\mu_{\rm ws} = e^{\nu(r)/2}\mu_{\rm ws}(r) = \text{constant}\,. \tag{2.59}$$

Outside each Wigner-Seitz cell, the system is strictly neutral and no global electric fields exist. Therefore, we can use the equation of state obtained with the relativistic Feynman-Metropolis-Teller treatment to calculate the structure of the star.

The equations of equilibrium to be integrated are the Einstein equations written in the Tolman-Oppenheimer-Volkoff form [24, 25]

$$\frac{d\nu(r)}{dr} = \frac{2G}{c^2}\frac{4\pi r^3P(r)/c^2 + M(r)}{r^2\left[1-\frac{2GM(r)}{c^2r}\right]}\,, \tag{2.60}$$

$$\frac{dM(r)}{dr} = 4\pi r^2\frac{\mathcal{E}(r)}{c^2}\,, \tag{2.61}$$

$$\frac{dP(r)}{dr} = -\frac{1}{2}\frac{d\nu(r)}{dr}[\mathcal{E}(r)+P(r)]\,, \tag{2.62}$$

where we have introduced the mass enclosed at the distance r through $e^{\lambda(r)} = 1 - 2GM(r)/(c^2r)$, $\mathcal{E}(r)$ is the energy-density and $P(r)$ is the total pressure.

In order to compare with the newtonian cases we study the effects of the relativistic case on the inverse β-decay instability and on the general relativistic instability.

2.2.1 Inverse β-decay instability and general relativistic instability

At high densities and very high electron Fermi pressures, electrons and protons combine to form neutrons. This process, known as inverse beta decay and occurs when the kinetic energy of the electrons exceeds the mass energy difference between a initial nucleus (Z, A) and the final nucleus $(Z-1, A)$. The experimental values of the threshold energy ϵ_Z^β are listed in Table 2.1.

In the uniform approximation, the critical density $\rho > \rho_{\rm crit}^\beta$ to trigger such process is given by

$$\rho_{\rm crit}^{\beta,\rm unif} = \frac{A_r}{Z}\frac{M_u}{3\pi^2\hbar^3c^3}[(\epsilon_Z^\beta)^2 + 2m_ec^2\epsilon_Z^\beta]^{3/2}\,, \tag{2.63}$$

where Eq. (2.9) has been used.

No analytic expression for $\rho_{\rm crit}^\beta$ can be found in the computation of the electron Fermi energy within the relativistic Feynman-Metropolis-Teller approach [1] because involves the numerical integration of the relativistic Thomas-Fermi equation. Then, the critical density $\rho_{\rm crit}^{\beta,\rm relFMT}$ is then obtained numerically by looking for the density at which the electron Fermi energy (2.44) equals ϵ_Z^β.

In Table 2.1 we can see, correspondingly to each threshold energy ϵ_Z^β, the critical density both in the Salpeter case $\rho_{\rm crit}^{\beta,\rm unif}$ given by Eq. (2.63) and in the relativistic Feynman-Metropolis-Teller case $\rho_{\rm crit}^{\beta,\rm relFMT}$.

Then, Rotondo et al.(2011) show that $\rho_{\rm crit}^{\beta,\rm relFMT} > \rho_{\rm crit}^{\beta,\rm unif}$ as one should expect from the fact that, for a given density, the electron density at the Wigner-Seitz cell boundary satisfies $n_e^{\rm relFMT} < n_e^{\rm unif}$. Therefore the electrons within the relativistic Feynman-Metropolis-Teller approach must be subjected to a larger density with respect to the one given by the approximated Salpeter analytic formula (2.63).

The effects of the relativistic FMT treatment on the general relativistic instability was also checked by [1]. For Newtonian white dwarfs the critical mass is reached asymptotically at infinite central densities of the object. One of the most important general relativistic effects is to shift this critical point to some finite density $\rho_{\rm crit}^{\rm GR}$.

This general relativistic effect is an additional source of instability with respect to the already discussed instability due to the onset of inverse β-decay which, contrary to the present general relativistic one, applies also in the Newtonian case by shifting

Decay	ϵ_Z^β	$\rho_{\rm crit}^{\beta,\rm relFMT}$	$\rho_{\rm crit}^{\beta,\rm unif}$
$^4\mathrm{He} \rightarrow {}^3\mathrm{H} + n \rightarrow 4n$	20.596	1.39×10^{11}	1.37×10^{11}
$^{12}\mathrm{C} \rightarrow {}^{12}\mathrm{B} \rightarrow {}^{12}\mathrm{Be}$	13.370	3.97×10^{10}	3.88×10^{10}
$^{16}\mathrm{O} \rightarrow {}^{16}\mathrm{N} \rightarrow {}^{16}\mathrm{C}$	10.419	1.94×10^{10}	1.89×10^{10}
$^{56}\mathrm{Fe} \rightarrow {}^{56}\mathrm{Mn} \rightarrow {}^{56}\mathrm{Cr}$	3.695	1.18×10^{9}	1.14×10^{9}

Table 2.1: Onset of inverse beta decay instability for ^{4}He, ^{12}C, ^{16}O and ^{56}Fe. The experimental inverse β-decay energies ϵ_Z^β are given in MeV and they have been taken from Table 1 of [4]. The corresponding critical density for the uniform electron density model, $\rho_{\rm crit}^{\beta,\rm unif}$ given by Eq. (2.63), is given in g/cm^3 as well as the critical density $\rho_{\rm crit}^{\beta,\rm relFMT}$ for the relativistic Feynman-Metropolis-Teller case. The numerical values of ϵ_Z^β are taken from [5], see also [6]

.

the maximum mass of Newtonian white dwarfs to finite densities (see e.g. [26]).

2.2.2 Numerical Results

The mass-central density relation and the mass-radius relation of general relativistic ^{4}He, ^{12}C, ^{16}O and ^{56}Fe white dwarfs using the relativistic FMT approach were presented in [1]. Here we show the results computed by them for a ^{4}He and ^{12}C Newtonian white dwarf of Hamada and Salpeter [7], for the Newtonian white dwarf of Chandrasekhar [11] and the general relativistic FMT equation of state [1].

Since the relativistic FMT approach takes into account self-consistently both β-decay equilibrium and general relativity, it can be determined if the critical mass is reached due either to inverse β-decay instability or to the general relativistic instability.

A comparison of the numerical value of the critical mass as given by Stoner [10], by Chandrasekhar [11] and Landau [12], by Hamada and Salpeter [7] and, by the relativistic FMT treatment can be found in Table 2.2.

A conclusion obtained from the numerical integrations by Rotondo [1] is that

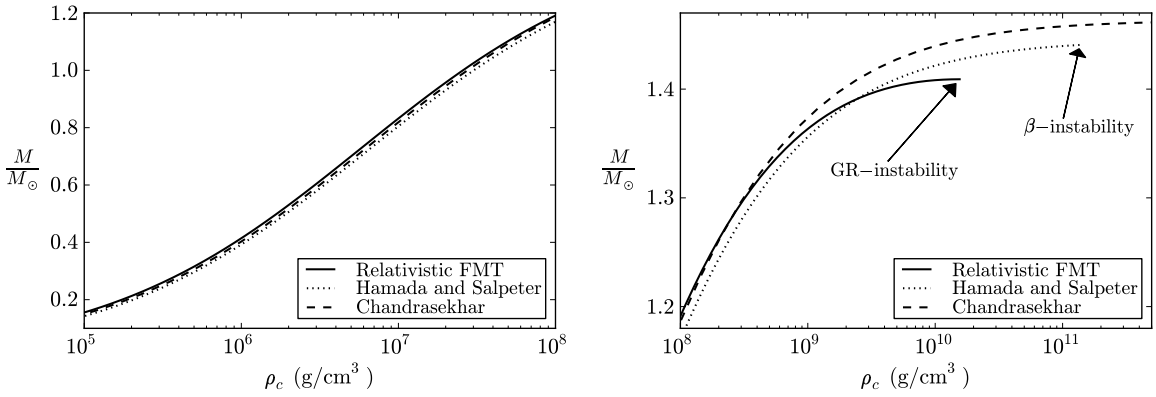

Figure 2.2: Mass in solar masses as a function of the central density in the range (left panel) 10^5–10^8 g/cm^3 and in the range (right panel) 10^8–5×10^{11} g/cm^3 for ^{4}He white dwarfs. The solid curve corresponds to the present work, the dotted curves are the Newtonian configurations of Hamada and Salpeter and the dashed curve are the Newtonian configurations of Chandrasekhar.

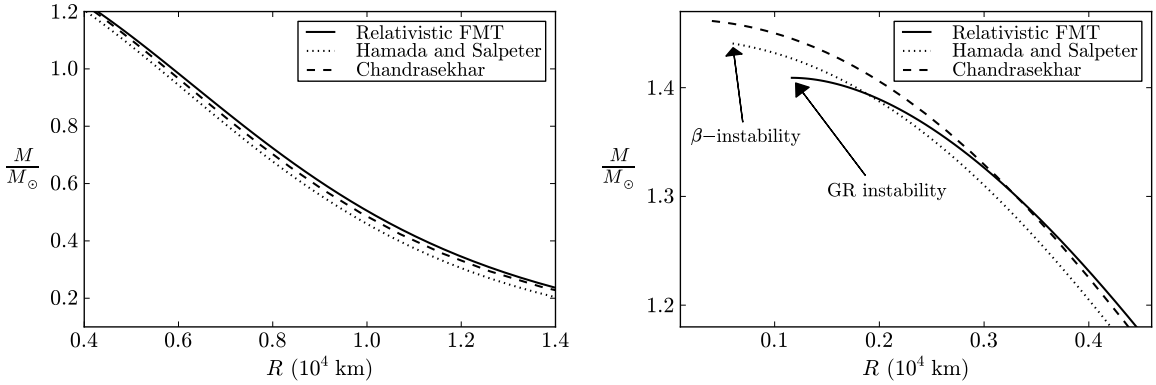

Figure 2.3: Mass as a function of the radius for ^{4}He WDs. They show the configurations for the same range of central densities of the panels of Fig. 2.2. The solid curve corresponds to the relativistic FMT, the dotted curves are the Newtonian configurations of Hamada and Salpeter and the dashed curve are the Newtonian configurations of Chandrasekhar.

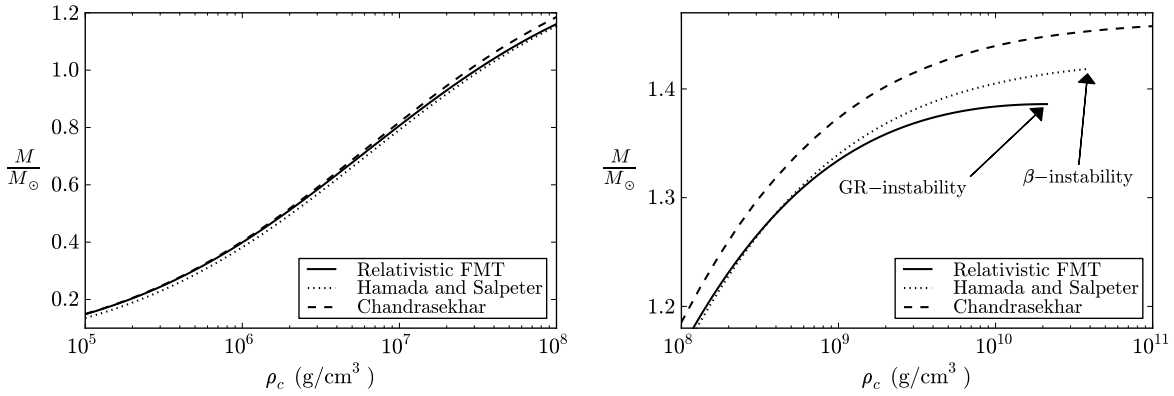

Figure 2.4: Mass in solar masses as a function of the central density in the range (left panel) 10^5–10^8 g/cm^3 and in the range (right panel) 10^8–10^{11} g/cm^3 for ^{12}C white dwarfs. The solid curve corresponds to the present work, the dotted curves are the Newtonian configurations of Hamada and Salpeter and the dashed curve are the Newtonian configurations of Chandrasekhar.

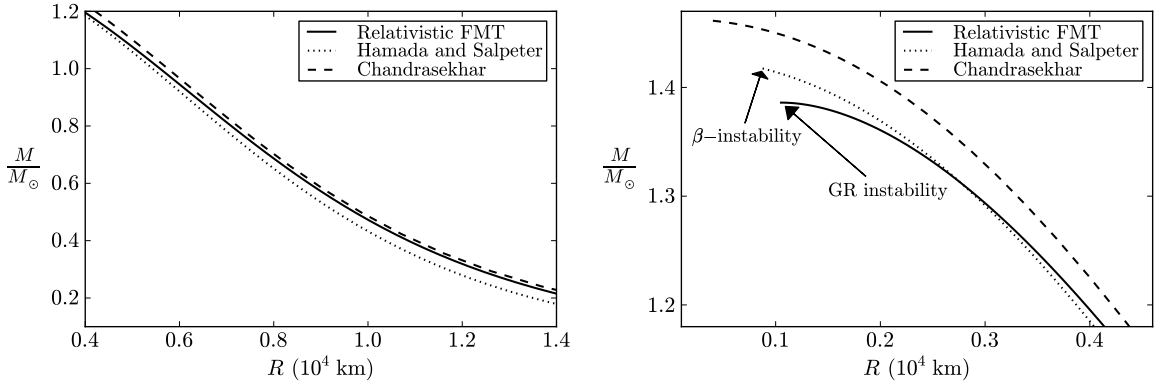

Figure 2.5: Mass in solar masses as a function of the radius in units of 10^4 km for ^{12}C white dwarfs. The left and right panels show the configurations for the same range of central densities of the corresponding panels of Fig. 2.4. The solid curve corresponds to the present work, the dotted curves are the Newtonian configurations of Hamada and Salpeter and the dashed curve are the Newtonian configurations of Chandrasekhar.

	$\rho_{\rm crit}^{\rm H\&S}$	$M_{\rm crit}^{\rm H\&S}/M_\odot$	$\rho_{\rm crit}^{\rm FMTrel}$	$M_{\rm crit}^{\rm FMTrel}/M_\odot$
^{4}He	1.37×10^{11}	1.44064	1.56×10^{10}	1.40906
^{12}C	3.88×10^{10}	1.41745	2.12×10^{10}	1.38603
^{16}O	1.89×10^{10}	1.40696	1.94×10^{10}	1.38024
^{56}Fe	1.14×10^{9}	1.11765	1.18×10^{9}	1.10618

Table 2.2: Critical density and corresponding critical mass for the onset of gravitational collapse of the Newtonian ^{4}He, ^{12}C, ^{16}O and ^{56}Fe white dwarfs of Hamada [7], based on the Salpeter equation of state [8], and of the corresponding general relativistic configurations obtained in this work based on the relativistic Feynman-Metropolis-Teller equation of state [1]. Densities are in g/cm^3 and masses in solar masses. For the sake of comparison, the critical mass of Stoner and of the one of Chandrasekhar-Landau are $M_{\rm crit}^{\rm Stoner} \sim 1.72 M_\odot$ and $M_{\rm crit}^{\rm Ch-L} \sim 1.45 M_\odot$, for the average molecular weight $\mu = A_r/Z = 2$. See [1] for further details.

^{4}He and ^{12}C white dwarfs satisfy $\rho_{\rm crit}^{\rm GR} < \rho_{\rm crit}^{\beta}$ (see Figs. 2.2 and Tables 2.1 and 2.2), so they are unstable with respect to general relativistic effects. The critical density of ^{12}C white dwarfs is $\sim 2.12 \times 10^{10}$ g/cm^3, to be compared with the value 2.65×10^{10} g/cm^3 obtained from calculations based on general relativistic corrections applied to polytropes (see e.g. [6]). And, it is worth to notice that the correct evaluation of general relativistic effects and of the combined contribution of the electrons to the energy-density of the system introduce, for ^{12}C white dwarfs, a critical mass not due to the inverse beta decay. When the contribution of the electrons to the energy-density is neglected (e.g. Chandrasekhar [11] and Hamada and Salpeter [7], see Eq. (2.9)) the critical density for ^{12}C white dwarfs is determined by inverse β-decay irrespective of the effects of general relativity.

2.3 Conclusions

In this chapter we presented the recently description of a compressed atom within the global approach of the relativistic Feynman, Metropolis and Teller [1] consid-

ering a Wigner-Seitz cell and applied to the construction of white dwarfs in the framework of general relativity. This treatment was the first approach of white dwarfs taking account gravitational, weak, strong and electromagnetic interactions. The critical mass can be obtained only through the numerical integration of the general relativistic equations of equilibrium with the equation of state obtained using the relativistic FMT, and no analytic formula can be derived. The critical mass and radius becomes a function of the composition of the star. The results of the relativistic FMT treatment have been compared and contrasted with the results of the non-relativistic models of Chandrasekhar and Hamada and Salpeter [7].

Chapter 3

The relativistic FMT treatment for WD at finite temperatures

In the previous chapter 2, we present the generalization of the classic work of Feynman, Metropolis and Teller (FMT) [17] to relativistic regimes, solving a compressed atom by the Thomas-Fermi equation in a Wigner-Seitz cell [1]. The integration of this equation does not admit any regular solution for a point-like nucleus and both the nuclear radius and the nuclear composition have necessarily to be taken into account [19, 20]. This introduces a fundamental difference from the non-relativistic Thomas-Fermi model where a point-like nucleus is adopted. So, this approach improves in the following aspects all previous treatments of the EOS of a compressed atom, including the classic works based on the uniform approximation by Chandrasekhar [11] and the EOS by Salpeter [8]:

1. in order to guarantee self-consistency with a relativistic treatment of the electrons, the point-like assumption of the nucleus is abandoned introducing a finite sized nucleus;

2. the Coulomb interaction energy is fully calculated without any approximation by solving numerically the relativistic Thomas-Fermi equation for each given nuclear composition;

3. the inhomogeneity of the electron distribution inside each Wigner-Seitz cell,

4. the energy-density of the system is calculated taking into account the contri-

butions of the nuclei, of the Coulomb interactions, as well as of the relativistic electrons to the energy of the Wigner-Seitz cells;

5. the β-equilibrium between neutrons, protons and electrons is also taken into account leading to a self-consistent calculation of the threshold density for triggering the inverse β-decay of a given nucleus.

The computation of the EOS is done by calculating the dependence of all these ingredients on the level of compression inside the star interior. In Ref. [27] has been shown how all these effects together with general relativity are important in the determination of the macroscopic structure of white dwarfs as well as for the determination of their maximum stable mass against gravitational collapse. More recently, the relativistic FMT EOS has been used to determine general relativistic equilibrium configurations of rotating white dwarfs [28].

In Fig. 3.1 we show the mass-radius relation of $T = 0$ white dwarfs for the relativistic FMT, Salpeter, and Chandrasekhar EOS and compare them with the estimated masses and radii of white dwarfs from the Sloan Digital Sky Survey Data Release 4 (SDSS-E06 catalog) [2]. It can be clearly seen that already for masses $\lesssim 0.7$–$0.8\ M_\odot$ deviations from the degenerate treatments are evident. It is natural to expect that such deviations could be related to the neglected effects of finite temperatures on the structure of the white dwarf. Thus, besides being interesting by their own, the finite temperature effects on the EOS and consequently on the mass-radius relation of the white dwarf are very important. Here we are going to extend our previous EOS [1], based on the degenerate relativistic FMT treatment, by introducing the effects of finite temperatures and use it to construct equilibrium configurations of white dwarfs at finite temperatures.

It is very interesting that there have been recently discovered ultra-low mass white dwarfs with masses $\lesssim 0.2 M_\odot$, which are companions of neutron stars in relativistic binaries; see e.g. Refs. [29, 30]. These low-mass white dwarfs represent the perfect arena to testing the EOS of compressed matter since the central densities of these objects are expected to be $\lesssim 10^6$ g cm^{-3}, where the degenerate approximation breaks down and so temperature effects cannot be neglected. Using the mass-radius

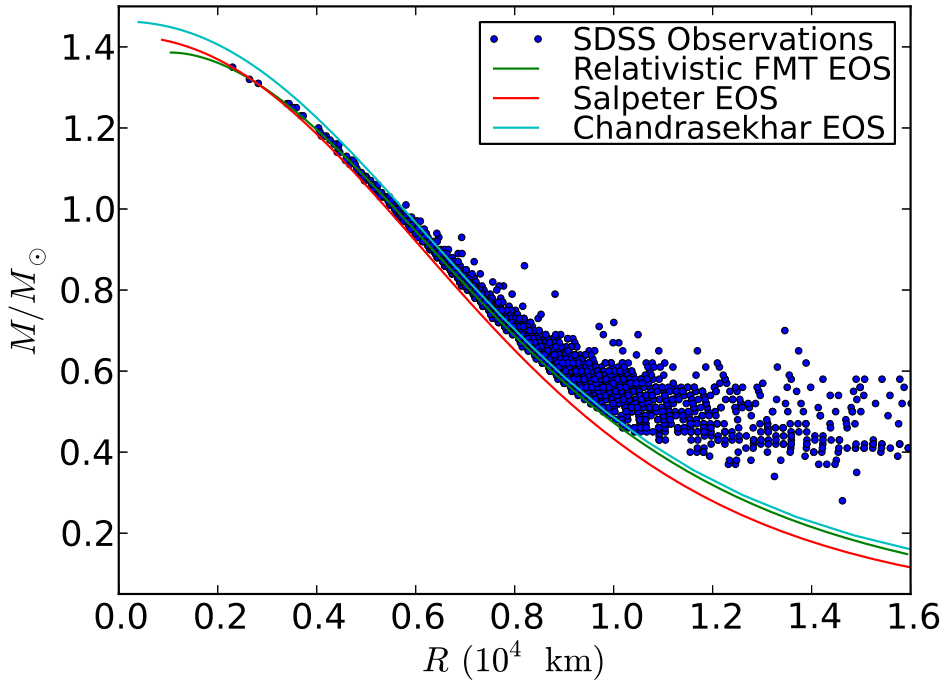

Figure 3.1: Mass-radius relations of white dwarfs obtained with the relativistic FMT, Salpeter, and Chandrasekhar EOS and their comparison with the estimated masses and radii of white dwarfs taken from the Sloan Digital Sky Survey Data Release 4 (SDSS-E06 catalog) [2].

relation at finite temperatures, we analyze in this chapter the structure of the white dwarf orbiting the pulsar PSR J1738+0333. We infer its mass, radius, surface gravity, internal temperature, and compare and contrast them with previous estimates.

The generalization of the relativistic FMT model presented in this chapter will be also useful to extend previous works in which the non-relativistic Thomas-Fermi model has been used to describe the physics of the low density layers of neutron stars including their atmospheres (see e.g. Ref. [31]). The proper treatment of the relativistic and Coulomb effects corrects the over and underestimate of the total pressure at high and low densities respectively, which occurs in non-relativistic Thomas-Fermi models and in the approximate Coulomb corrections of Salpeter [8]; see [1], for further details.

In this chapter we describe the extension of the relativistic FMT treatment to finite temperatures. We summarize the results of the numerical integration of the equations and describe the general properties of the new EOS. Then, we construct the mass-radius relation of white dwarfs, showing specifically the results for ^{4}He composition and we apply these results to the case of the ultra-low mass white dwarf companion of PSR J1738+0333.

3.1 Generalization of the EOS to finite temperatures

We now consider the equations of equilibrium of a relativistic gas of electrons at a temperature $T \neq 0$ surrounding a finite sized and positively charged nucleus of mass and atomic numbers A and Z, respectively. The electron cloud is confined within a radius $R_{\rm WS}$ of a globally neutral Wigner-Seitz cell and the system is isothermal.

Following the chapter 2 (sec.2.1.5), the proton number density can be written as Eq. (2.45). And clearly, the electron number density follows from Fermi-Dirac statistics and is given by

$$n_e = \frac{2}{(2\pi\hbar)^3}\int_0^\infty \frac{4\pi p^2 dp}{\exp\left[\frac{\tilde{E}(p)-\tilde{\mu}_e(p)}{k_B T}\right]+1}, \tag{3.1}$$

where k_B is the Boltzmann constant, $\tilde{\mu}_e$ is the electron chemical potential without the rest-mass, and $\tilde{E}(p) = \sqrt{c^2p^2 + m_e^2c^4} - m_ec^2$, with p and m_e the electron momentum and rest-mass, respectively.

Introducing the degeneracy parameter $\eta = \tilde{\mu}_e/(k_BT)$, $t = \tilde{E}(p)/(k_BT)$, and $\beta = k_BT/(m_ec^2)$, we can write the electron number density as

$$n_e = \frac{8\pi\sqrt{2}}{(2\pi\hbar)^3} m^3c^3\beta^{3/2} \left[F_{1/2}(\eta,\beta) + \beta F_{3/2}(\eta,\beta)\right], \tag{3.2}$$

where

$$F_k(\eta,\beta) \equiv \int_0^\infty \frac{t^k\sqrt{1+(\beta/2)t}}{1+e^{t-\eta}}\, dt \tag{3.3}$$

is the relativistic Fermi-Dirac integral.

We consider temperatures that satisfy $T \ll m_ec^2/k_B \approx 6\times10^9$ K, so we will not take into account the presence of anti-particles. The Thomas-Fermi equilibrium condition for the relativistic electron gas is in this case given by

$$\tilde{\mu}_e(r) - eV(r) = k_BT\eta(r) - eV(r) = \text{constant}, \tag{3.4}$$

where $V(r)$ is the Coulomb potential.

By introducing the dimensionless quantities $x = r/\lambda_\pi$, $x_c = R_c/\lambda_\pi$, $\chi/r = \tilde{\mu}_e/(\hbar c)$ and replacing the above particle densities into the Poisson Equation

$$\nabla^2V(r) = 4\pi e[n_p(r) - n_e(r)], \tag{3.5}$$

we obtain the generalization of the relativistic Thomas-Fermi equation to finite temperatures

$$\frac{d^2\chi(x)}{dx^2} = -4\pi\alpha x\left\{\frac{3}{4\pi\Delta^3}\theta(x_c-x) - \frac{\sqrt{2}}{\pi^2}\left(\frac{m_e}{m_\pi}\right)^3\beta^{3/2}\left[F_{1/2}(\eta,\beta) + \beta F_{3/2}(\eta,\beta)\right]\right\}. \tag{3.6}$$

The Eq. (3.6) must be integrated subjected to the same boundary conditions as in the degenerate case, given by Eq. (2.49).

We turn now to compute the energy of the Wigner-Seitz cell. For the present case of finite temperatures, the total energy of each cell can be split as

$$E_{\rm WS} = E_N + E_k + E_C, \tag{3.7}$$

where

$$E_N = M_N(A,Z)c^2 + U_{\rm th}, \quad U_{\rm th} = \frac{3}{2}k_B T, \tag{3.8}$$

$$E_k = \int_0^{R_{\rm WS}} 4\pi r^2 (\mathcal{E}_e - m_e n_e) dr, \tag{3.9}$$

$$E_C = \frac{1}{2}\int_{R_c}^{R_{\rm WS}} 4\pi r^2 e[n_p(r) - n_e(r)]V(r)dr, \tag{3.10}$$

are the nucleus, kinetic, and Coulomb energy. For the nucleus mass $M_N(A,Z)$ we adopt experimental values, $U_{\rm th}$ is the thermal energy of nuclei which we here adopt as an ideal gas [1], and the electron energy density $\mathcal{E}_e$ is given by

$$\mathcal{E}_e = m_e c^2 n_e + \frac{\sqrt{2}}{\pi^2\hbar^3} m_e^4 c^5 \beta^{5/2} \left[F_{3/2}(\eta,\beta) + \beta F_{5/2}(\eta,\beta)\right]. \tag{3.11}$$

The total density and pressure are then given by

$$\rho = \frac{E_{\rm WS}}{c^2 V_{\rm WS}}, \tag{3.12}$$

$$P = P_N + P_e, \tag{3.13}$$

where

$$P_N = \frac{2}{3}\frac{U_{\rm th}}{V_{\rm WS}} = \frac{k_B T}{V_{\rm WS}}, \tag{3.14}$$

$$P_e = \frac{2^{3/2}}{3\pi^2\hbar^3} m_e^4 c^5 \beta^{5/2} \left[F_{3/2}(\eta_{\rm WS},\beta) + \frac{\beta}{2}F_{5/2}(\eta_{\rm WS},\beta)\right], \tag{3.15}$$

being $\eta_{\rm WS}$ the value of η at the boundary of the Wigner-Seitz cell with volume $V_{\rm WS} = 4\pi R_{\rm WS}^3/3$.

3.2 Numerical integration of the equations and the EOS

For a given chemical composition (Z,A), temperature T (i.e. β), and dimensionless Wigner-Seitz cell radius $x_{\rm WS}$, the relativistic Thomas-Fermi equation (3.6) is

[1] Quantum corrections to the ideal behavior of the ions considered here can be straightforwardly included following previous treatments such as [32, 33, 34]

integrated subjected to the boundary conditions (2.49). We thus obtain both the Coulomb potential and the function η inside the given Wigner-Seitz cell. With the knowledge of $\eta_{\rm WS}$, we proceed to evaluate first the energy of the cell by Eqs. (3.7–3.11) and subsequently the values of the density and pressure through Eqs. (3.12–3.15). For fixed chemical composition and temperature, we repeat the above steps for different cell radii to obtain different compression levels of the system; this leads to different densities and pressures, hence the EOS. These steps can be then performed for different compositions and temperatures; the results are discussed below.

3.2.1 Properties of the EOS

As we showed in Ref. [1], as a result of the Coulomb interaction duly accounted for in the relativistic Thomas-Fermi treatment, the distribution of the electrons inside a Wigner-Seitz cell is not uniform. In order to show the effects of the temperature, in Fig. 3.2 we show as an example the electron number density inside a Wigner-Seitz cell of ^{56}Fe at a density of 30 g cm^{-3} and for temperatures $T = [0, 10^7, 10^{10}]$ K.

We can see in Fig. 3.2 how the effect of the temperature tends to homogenize the electron distribution inside the cell. In addition, we notice that the larger the temperature the larger the value of the electron density at the border of the Wigner-Seitz cell, thus increasing the electron pressure. This effect can be clearly seen in Fig. 3.3 where we show the value of the electron number density evaluated at the cell radius, $R_{\rm WS}$, as a function of the density for the temperatures $T = [10^4, 10^5, 10^6, 10^7, 10^8]$ K, for a given chemical composition, ^{12}C.

The volume of the Wigner-Seitz cell, $V_{\rm WS} = 4\pi R_{\rm WS}^3/3$, determines the density of the system ρ given by Eq. (3.12); the smaller the volume the larger the density. In Fig. 3.4 we show the density of the system as a function of the Wigner-Seitz cell radius $R_{\rm WS}$ for a temperature $T = 10^7$ K and ^{12}C chemical composition. Small deviations of the $R_{\rm WS}^{-3}$ behavior are due to the inhomogeneity of the electron distribution inside the cell and to the contribution of the Coulomb and electron kinetic energy to the density.

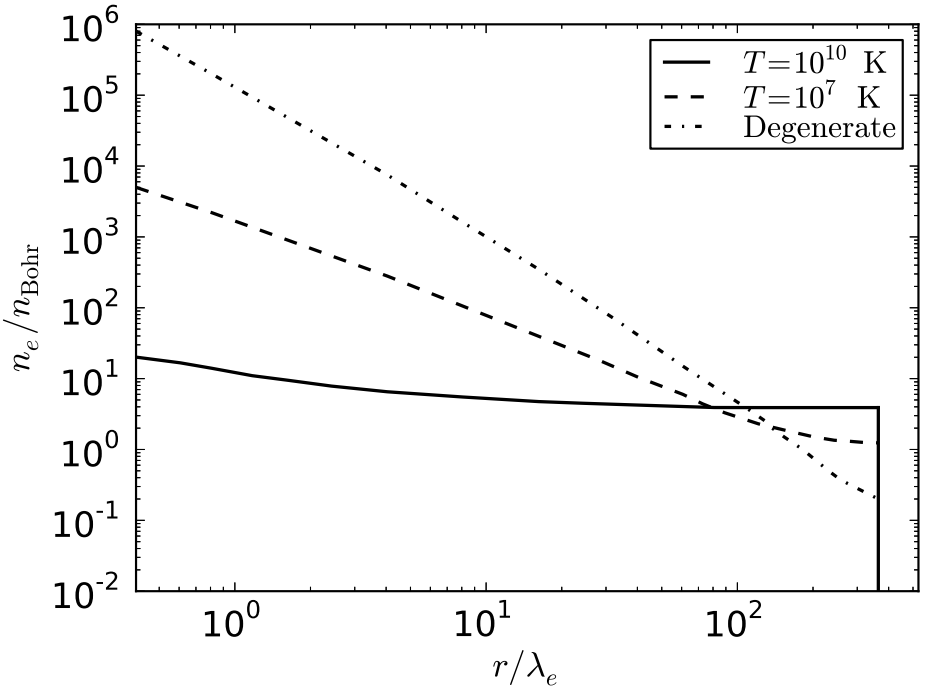

Figure 3.2: Electron number density inside a Wigner-Seitz cell of ^{56}Fe at a density of 30 g cm^{-3} at selected temperatures. Here $n_{\rm Bohr} = 3/(4\pi R_{\rm Bohr}^3) \approx 1.6 \times 10^{24}$ cm^{-3}, where $R_{\rm Bohr} = \hbar/(e^2 m_e) \approx 5.3 \times 10^{-9}$ cm, is the Bohr radius. In this example we have used both low density and high temperatures up to 10^{10} K in order to show an extreme example of electron density flattening.

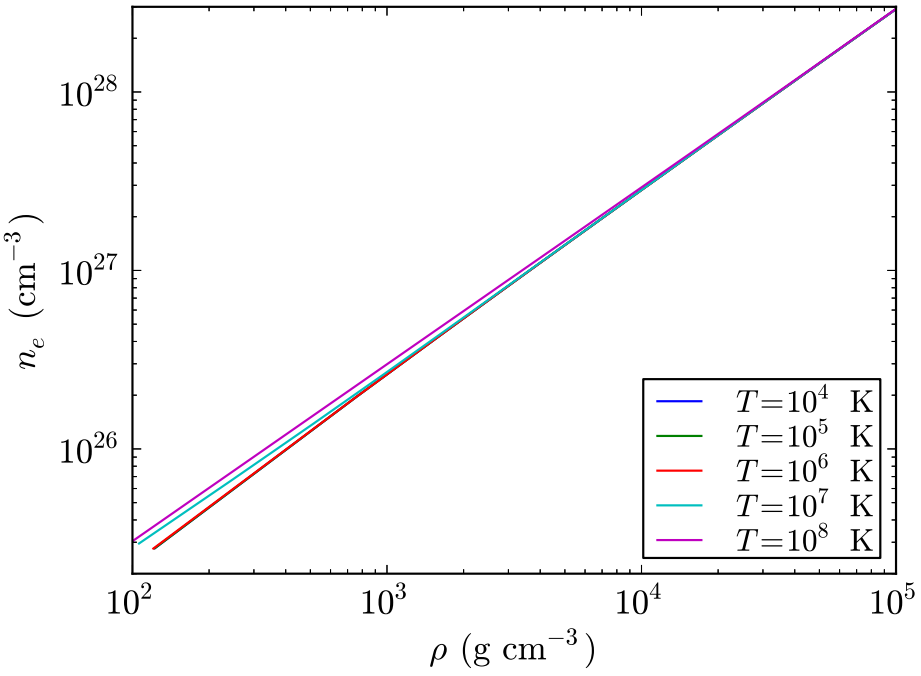

Figure 3.3: Electron number density at the radius of a Wigner-Seitz cell of ^{12}C as a function of the density (3.12) for the selected temperatures $T = [10^4, 10^5, 10^6, 10^7, 10^8]$ K.

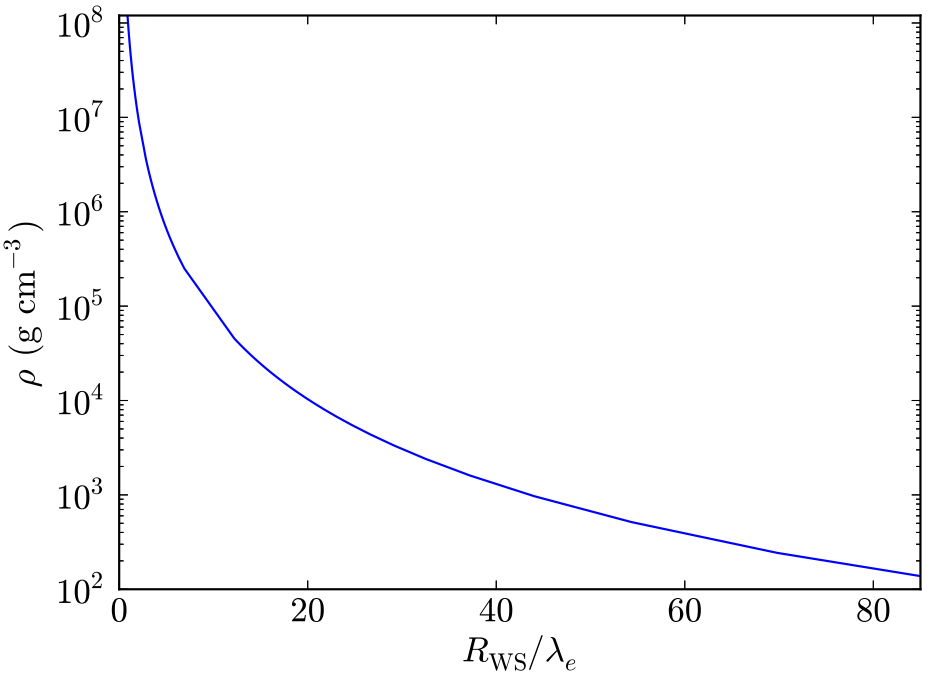

Figure 3.4: Total density (in g cm^{-3}) of the system as a function of the radius of the Wigner-Seitz cell (in units of the electron Compton wavelength $\lambda_e = \hbar/(m_e c) \approx 3.9 \times 10^{-11}$ cm) in the case of ^{12}C at a temperature $T = 10^7$ K.

In this line it is important to mention that often in the literature the density of the system is approximated as

$$\rho = \frac{A}{Z} M_u n_e, \tag{3.16}$$

which corresponds to the rest-mass density of nuclei in the system and where a uniform distribution of electrons is assumed. Here $M_u = 1.6604 \times 10^{-24}$ g is the unified atomic mass. We can see from Eq. (3.7) that this is equivalent to neglect the thermal, kinetic, and Coulomb energy of the cells as well as the inhomogeneity of the electron density. However, as we showed in Refs. [1, 27], the inclusion of the Coulomb and electron kinetic energies are important at low and high densities, respectively. In particular, the contribution of the kinetic energy of the electrons to the energy density is fundamental in the determination of the critical density for the gravitational collapse of ^{12}C white dwarfs [27]. We show in Fig. 3.5 the effect on the EOS of using as density of the system only the nuclei rest-mass, Eq. (3.16), instead of the full mass density given by Eq. (3.12) which accounts for the total energy of the Wigner-Seitz cell given by Eq. (3.7).

The effects of finite temperatures are clearly expected to be important at low densities, where the system looses its degeneracy. The point where the EOS should start to deviate from its degenerate behavior can be estimated by equating the degenerate and ideal gas pressures for the electron component. Assuming the electrons as non-relativistic we have, $n_e k_B T = (3\pi^2)^{2/3} \hbar^2 n_e^{5/3}/m_e$, from which we obtain that temperature effects are important for densities

$$\rho \lesssim 1.5 \times 10^3 \left(\frac{T}{10^7\,\mathrm{K}} \right)^{3/2} \mathrm{g\,cm^{-3}}, \tag{3.17}$$

where we have used $A/Z \approx 2$ and $\rho \approx A M_u n_e/Z$. In Fig. 3.6 we compare the relativistic degenerate FMT EOS [1, 27] and its generalization at finite temperatures presented in this work, for the cases $T = 10^7$ and 10^8 K and ^{12}C chemical composition. For these specific temperatures we see that deviations of the degenerate EOS start at a density $\rho \approx 2 \times 10^4$ g cm^{-3} and $\approx 10^6$ g cm^{-3}, respectively. For the same temperatures, Eq. (3.17) estimate deviations from degeneracy at $\rho \approx 1.5 \times 10^3$ g cm^{-3} and $\approx 4.8 \times 10^4$ g cm^{-3}, respectively. Thus, the lower the temperature

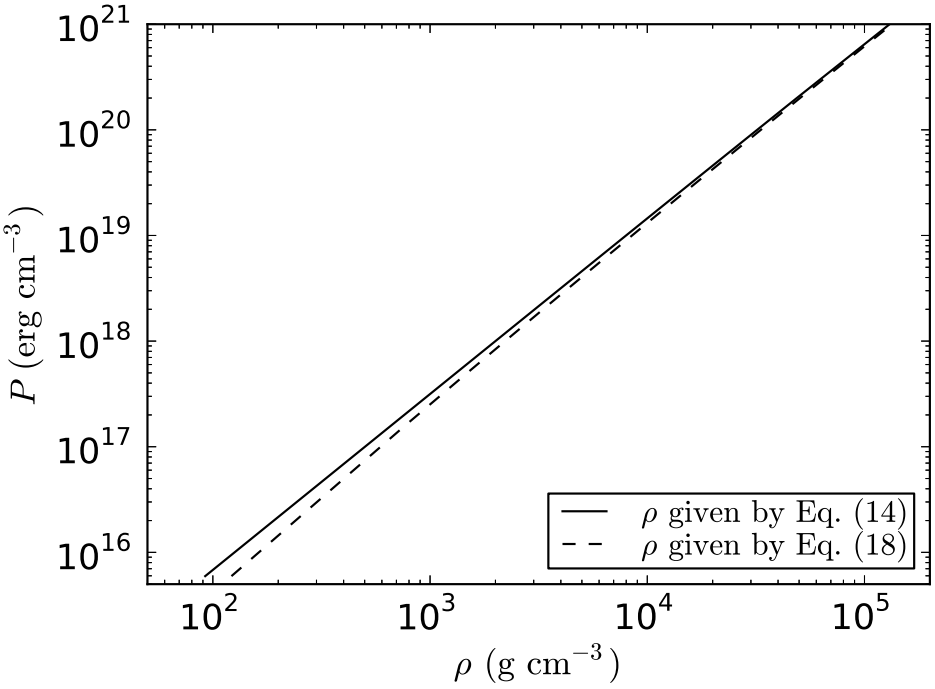

Figure 3.5: Total pressure as a function of the matter density $\rho = AM_u n_e/Z$, given by Eq. (3.16), and $\rho = E_{\rm WS}/(c^2 V_{\rm WS})$ given by Eq. (3.12) which includes the thermal, kinetic, and Coulomb energy in the Wigner-Seitz cell. In this example the composition is ^{12}C and the temperature $T = 10^4$ K.

the better the estimate given by Eq. (3.17); the reason for this is that for larger temperatures the system will loose the degeneracy at larger densities where the non-relativistic approximation for the electrons breaks down.

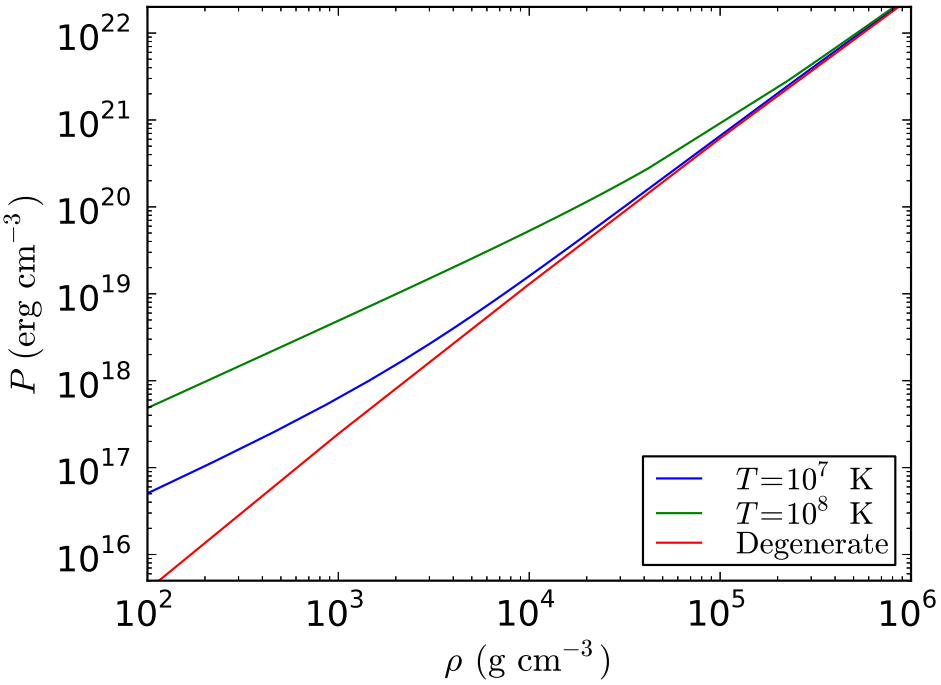

Figure 3.6: Comparison of the EOS for ^{12}C at temperatures $T = [0, 10^7, 10^8]$ K.

In Fig. 3.7, we show the nuclei to electron pressure ratio in cells of ^{12}C as a function of the density and for selected temperatures. It can be seen that for all temperatures the ratio approaches the same constant value in the low density regime. This is due to the fact that at sufficiently low densities also the electron gas becomes an ideal gas and consequently its pressure is approximately given by $P_e^{\rm id} = Zk_BT/V_{\rm WS}$. Therefore, the nuclei to pressure ratio approaches the limit $P_N/P_e^{\rm id} = 1/Z$, where P_N is given by Eq. (3.14). In the example of Fig. 3.7 we have $Z = 6$ so $P_N/P_e^{\rm id} \approx 0.17$. It is clear that the density at which each curve reaches such a constant value increases with the temperature, since at larger temperatures the electrons reach their ideal gas state at higher densities.

We summarize the finite temperature generalization of the relativistic FMT EOS in Fig. 3.8, where we plot as an example the total pressure (3.13) as a function of

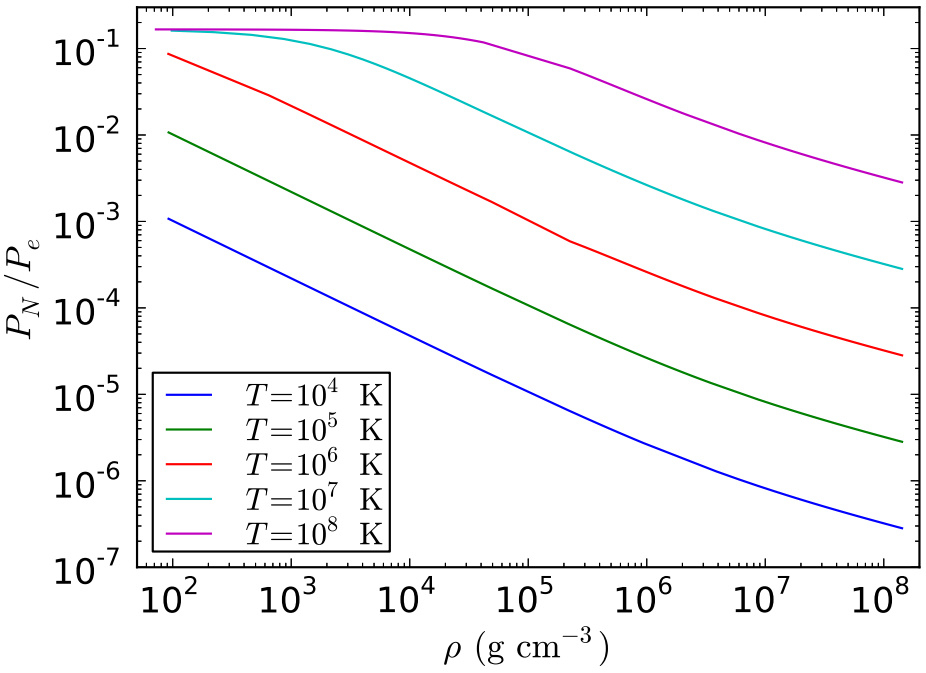

Figure 3.7: Nuclei to electron pressure ratio as a function of the mass density in the case of ^{12} C white dwarf for selected temperatures in the range $T = 10^4$–10^8 K.

the total density of the system (3.12) at temperatures $T = [10^4, 10^5, 10^6, 10^7, 10^8]$ K and for a chemical composition, ^{12}C. All the above features of the EOS are general and therefore applied also to chemical compositions other than ^{12}C.

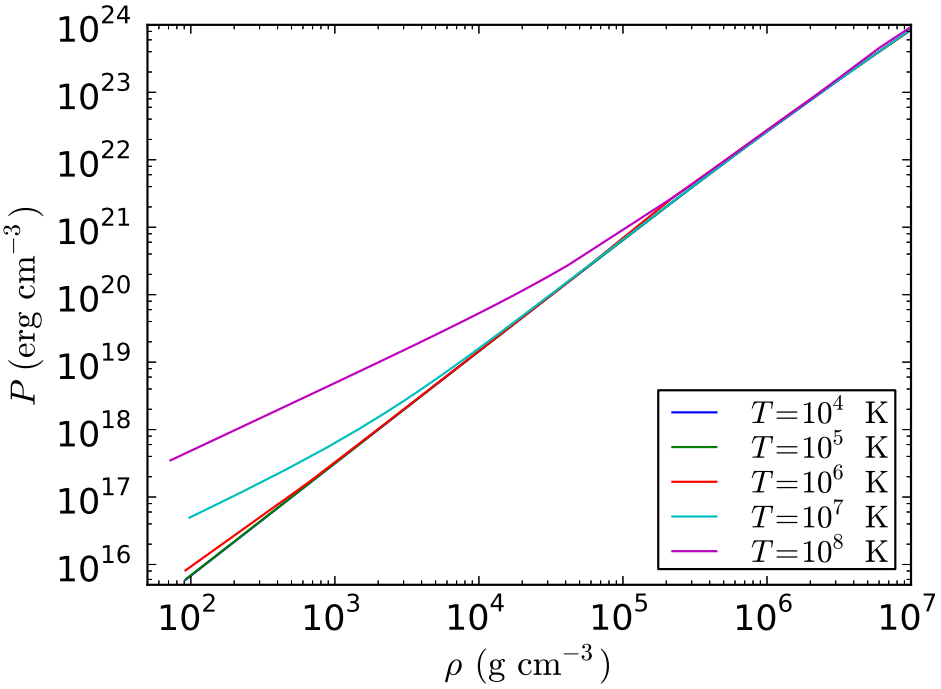

Figure 3.8: Total pressure as a function of the mass density in the case of ^{12} C white dwarf for selected temperatures in the range $T = 10^4$–10^8 K.

3.2.2 Inverse β decay and pycnonuclear reactions

We turn now to the finite temperature effects on the inverse β decay instability. The critical density $\rho^{\beta}_{\rm crit}$ is obtained numerically by looking for the density at which the electron energy equals ϵ^{β}_{Z}. In Table 2.1 we showed that, in the degenerate case, the threshold energies to trigger the inverse β process for ^{4}He, ^{12}C, ^{16}O, and ^{56}Fe are reached at densities, $\rho^{\beta}_{\rm crit} = 1.37 \times 10^{11}$, 3.88×10^{10}, 1.89×10^{10}, and 1.14×10^9 g cm^{-3}, respectively.

For the present finite temperature case, from our numerical integration we found that the critical densities for the occurrence of the inverse β decay instability are not affected so that they are the same as in the degenerate approximation. This is due

to the fact that the effects of temperatures $T \lesssim 10^8$ K become relevant at densities $\rho \lesssim 10^6$ g cm^{-3}, as can be seen from Figs. 3.6 and 3.8.

We turn now to the pycnonuclear reactions. In a nuclei lattice the nuclear reactions proceed with the overcoming of the Coulomb barrier between neighbor nuclei. At zero temperatures, $T = 0$, the Coulomb barrier can be overcome due to the zero-point energy of the nuclei (see e.g. [35, 36])

$$E_p = \hbar\omega_p\,, \qquad \omega_p = \sqrt{\frac{4\pi e^2 Z^2 \rho}{A^2 M_u^2}}\,. \tag{3.18}$$

The number of pycnonuclear reactions per unit volume per unit time increases with the density of the system [35] and any effect that reduces the Coulomb barrier will increase the cross-section of the reaction. The inclusion of the temperature could then lead to thermo-enhanced pycnonuclear rates (see e.g. Refs. [35, 37]). The astrophysical importance of pycnonuclear reactions e.g. in the theory of white dwarfs relies on the fact that for instance the ^{12}C+^{12}C pycnonuclear fusion, leading to ^{24}Mg, is possible in a time scale shorter than a Hubble time, $\tau_{\rm pyc} < 10$ Gyr, for densities $\sim 10^{10}$ g cm^{-3}. Such a density turns to be larger than the critical density $\sim 3 \times 10^9$ g cm^{-3} for the double inverse β decay of ^{24}Mg into ^{24}Ne by electron capture (see e.g. [8, 36]), which destabilize the white dwarf due to sudden decrease of its electron pressure. Under such conditions, ^{12}C+^{12}C fusion will indirectly induce the gravitational collapse of the white dwarf rather than to a supernova explosion.

Following the updated reaction rates of Ref. [37], we recently computed in [28] the critical density for pycnonuclear instability in general relativistic uniformly rotating ^{12}C white dwarfs, at zero temperatures. It comes out that the instability agent of white dwarfs can be either general relativistic effects or inverse β decay or pycnonuclear reactions or rotation through mass-shedding or secular instabilities (see [28], for details).

The electrons around the nuclei screen the positive charge of the nucleus reducing the Coulomb barrier; hence their proper inclusion could in principle increase the reaction rates. On the other hand, we showed in Figs. 3.2 and 3.3 two different effects owing to the finite temperature: 1) it tends to flatten the electron distribution, thus changing the electron screening of the Coulomb potential with respect to the

degenerate case; and 2) it increases the electron density hence the pressure at the border of the cell. These effects clearly could lead not only to qualitative but also to quantitative differences in the estimate of the rates of the pycnonuclear reactions (see e.g. [38]).

However, the inclusion of these combined effects within the pycnonuclear reactions treatment, following a fully relativistic approach of the electron gas and the Coulomb interactions as the one presented here, is a most difficult and complex task that deserves a detailed and separated analysis, and therefore will not be addressed here.

3.3 Mass-Radius relation

General relativistic effects are important in the high density branch of white dwarfs; for instance they lead to the gravitational collapse of the star prior to the trigger of the inverse β decay instability in ^{12}C white dwarfs [27].We here construct the mass-radius relation of white dwarfs in their entire range of stability, so we use the equations of hydrostatic equilibrium within the framework of general relativity given by TOV equations; Eq. (2.62).

These equations can be integrated for a wide range of central densities, temperatures, and for selected chemical compositions, for instance ^{4}He, ^{12}C, ^{16}O, and ^{56}Fe. In Figs. 3.9 and 3.10, we show in particular the mass-central density and mass-radius relations of ^{4}He white dwarfs in the range of densities and radii where finite temperature effects are more important.

The minimum in these plots mark the transition from the ideal to the degenerate behavior of the electron gas: from left to right in the $M-\rho_c$ relation and from left to right in the $M-R$ relation. Thus these minimum can be used to give an estimate of the minimum mass that a star should have to be able to burn stably a given chemical composition since the condition of a stable burning requires that the gas be non-degenerate. Consequently, stable burning requires that the star lies on the branch of solutions on the left-hand side of the minimum of the $M-\rho_c$ diagram or on the right-hand side of the minimum of the $M-R$ diagram. For instance, helium

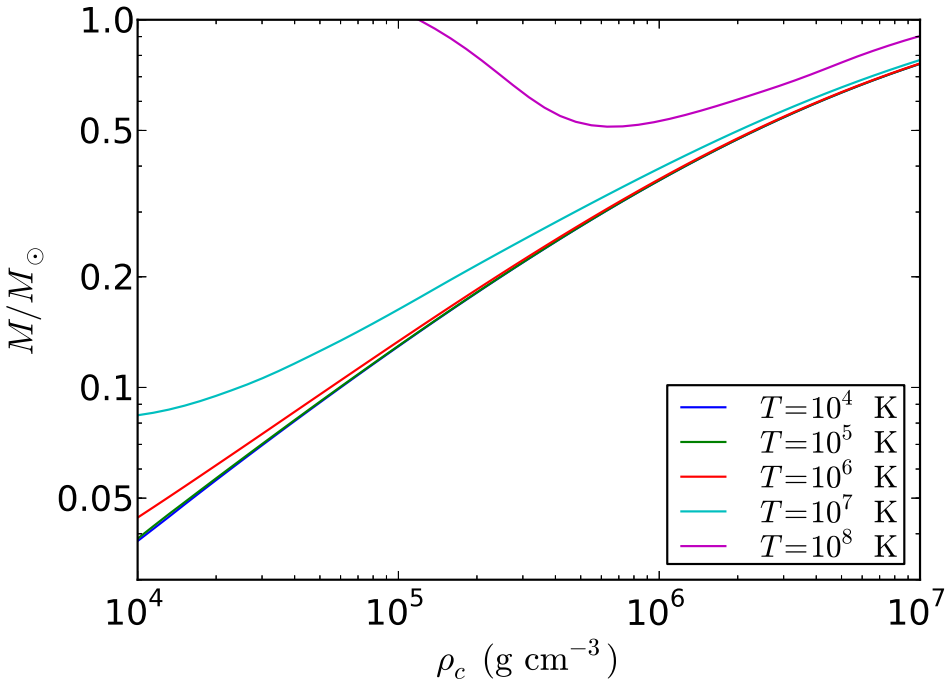

Figure 3.9: Total mass versus radius for ^{4}He white dwarfs for selected temperatures from $T = 10^4$ K to $T = 10^8$ K.

burning is triggered at a temperature $T_{\rm He+He} \approx 10^8$ K, so we can obtain from the solutions shown in Fig. 3.9 that the minimum mass for stable helium burning is $M_{\rm min}^{\rm He+He} \approx 0.51\ M_\odot$. The corresponding radius and density of this configuration is 4.54×10^9 cm$\approx 0.065\ R_\odot$ and 6.59×10^5 g cm^{-3}, respectively. A similar analysis can be done for the other compositions.

3.4 The ultra low-mass white dwarf companion of PSR J1738+0333

It is clear that the effects of the temperature are particularly important at low densities, and hence for low-mass white dwarfs. We analyze here the specific case of the white dwarf companion of the millisecond pulsar PSR J1738+0333. We refer to [30], for details on the observations and technical aspects of the derivation of the binary parameters.

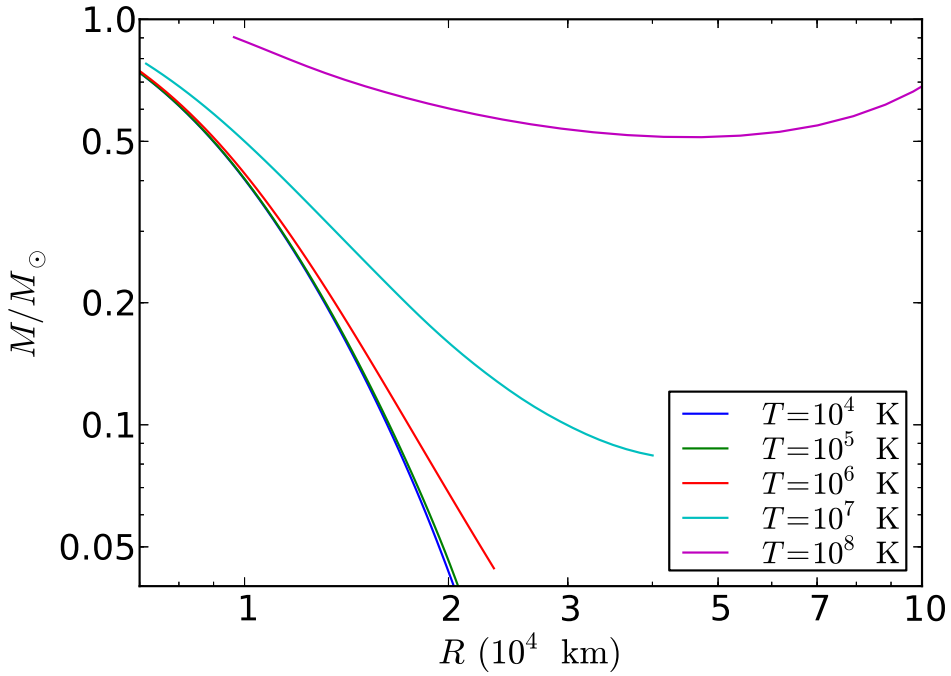

Figure 3.10: Total mass versus central density for ^{4}He white dwarfs for selected temperatures from $T = 10^4$ K to $T = 10^8$ K.

Antoniadis et al. [30] obtained with the the Goodman High Throughput Spectrograph instrument of the Southern Astrophysical Research Telescope (SOAR) at Cerro Pachón, Chile, a photometric radius of the white dwarf, $R_{\rm WD} = 0.042 \pm 0.004 R_\odot$. On the other hand, the analysis of the white dwarf atmosphere spectrum with the models of Ref. [39] led to an effective surface temperature, $T_{\rm eff} = 9130 \pm 150$ K, and a logarithm of the surface gravity, $\log(g) = \log(GM_{\rm WD}/R^2_{\rm WD}) = 6.55 \pm 0.1$. Using the evolutionary mass-radius relation of Painei et al. [40], the mass of the white dwarf was estimated in Ref. [30] to be $M_{\rm WD} = 0.181^{+0.007}_{-0.005}$ M$_\odot$, and a corresponding radius $R_{\rm WD} = 0.037^{+0.004}_{-0.003}\ R_\odot$, in agreement with the photometric value.

A first attempt to obtain the mass of the white dwarf can be done directly from the observed data by combining the spectral and photometric analysis. Assuming the photometric radius as the star radius the mass of the white dwarf would be $M_{\rm WD} = gR^2_{\rm WD}/G \approx 0.23\, M_\odot$, using the central values of $R_{\rm WD}$ and g, which is roughly consistent with the mass derived from the mass-radius relation of Ref. [40].

In order to compare our mass-radius relation at finite temperatures with the above results and infer the internal temperature of the white dwarf, we plotted in Figs. 3.11 and 3.12 our theoretical surface gravity-mass and radius relations for ^{4}He white dwarfs, together with the above observational constraints.

An inspection of Fig. 3.11 does not give us any information on the possible internal temperature of the white dwarf since, in principle, we do not have any a priori information on the mass. However, from Fig. 3.12 we clearly identify that the interior temperature of the white dwarf core should be $T \approx$ 2–3 $\times 10^7$ K. In Fig. 3.13 we plot the mass-radius relation for ^{4}He white dwarfs with the observational constraints of the companion of PSR J1738+0333. We can now compare our results with an estimate obtained for instance using the relation found by Koester in Ref. [41] between the central and surface temperatures of the white dwarf, $T^4_{\rm eff}/g = 2.05 \times 10^{-10} T_c^{2.56}$. Using the value $T_{\rm eff} = 9130$ K and $\log(g) = 6.55$, this relation gives $T_c \approx 2.6 \times 10^7$ K, in full agreement with our inference. In this estimate we have neglected the contribution of the thickness of the envelope to the total surface radius of the white dwarf. However, this approximation does not introduce a large error since the envelope would be in this case at most $\sim 10^{-2}\ R_{\rm WD}$

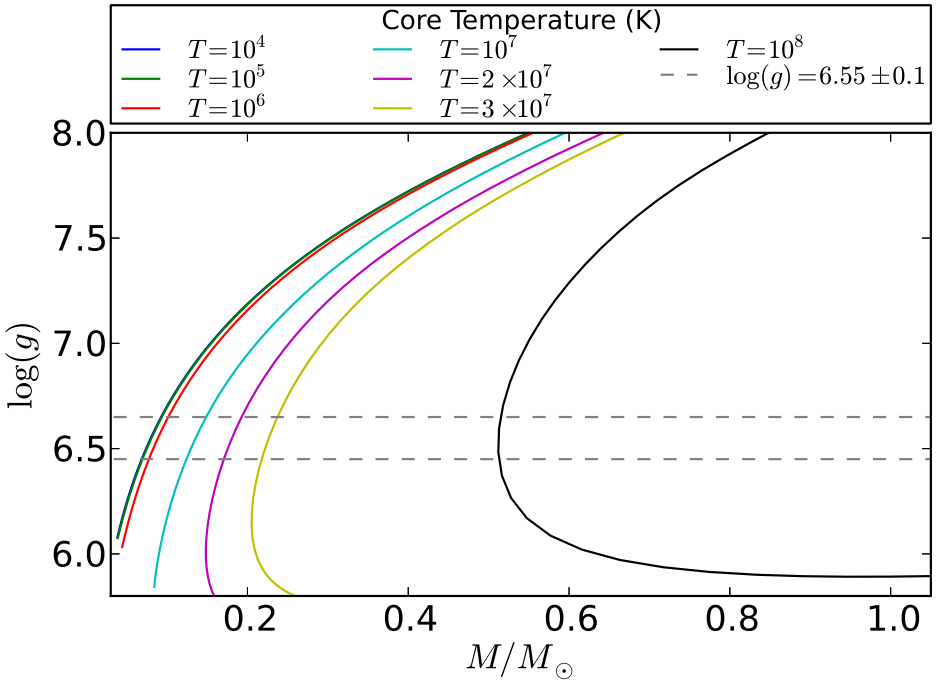

Figure 3.11: Logarithm of the surface gravity, $\log(g) = \log(GM_{\rm WD}/R^2_{\rm WD})$, as a function of the mass for ^{4}He white dwarfs for selected interior temperatures from $T = 10^4$ K to $T = 10^8$ K. The horizontal dashed lines indicate the maximum and minimum best-fit values $\log(g) = 6.55 \pm 0.1$.

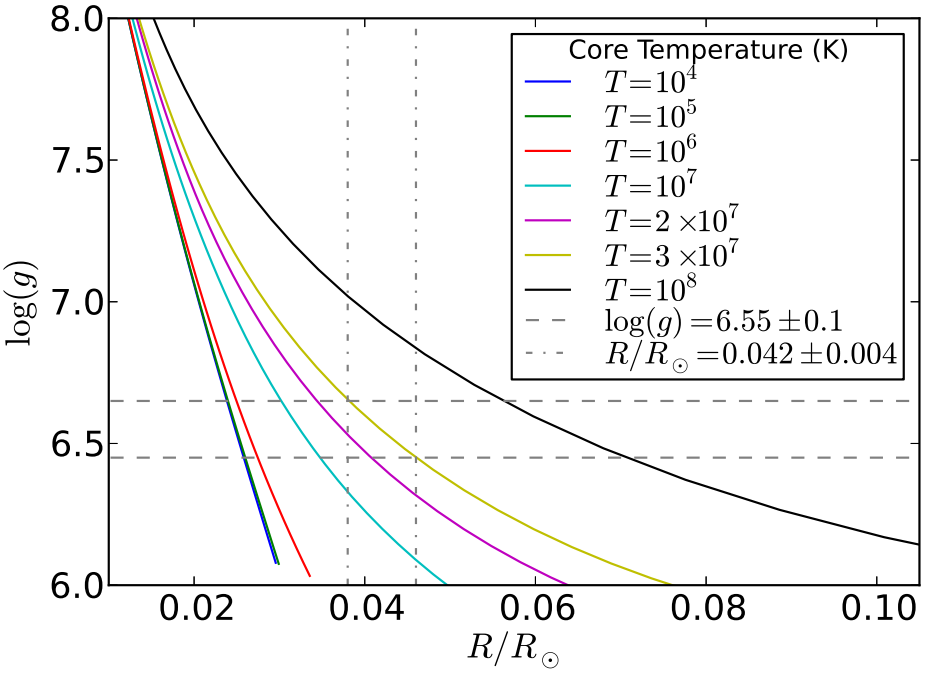

Figure 3.12: Logarithm of the surface gravity, $\log(g) = \log(GM_{\rm WD}/R^2_{\rm WD})$, as a function of the radius for ^{4}He white dwarfs for selected interior temperatures from $T = 10^4$ K to $T = 10^8$ K. The horizontal dashed and dot-dashed lines indicate the maximum and minimum best-fit values of the surface gravity, $\log(g) = 6.55 \pm 0.1$ and photometric radii $R_{\rm WD} = 0.042 \pm 0.004 R_\odot$, respectively.

thick.

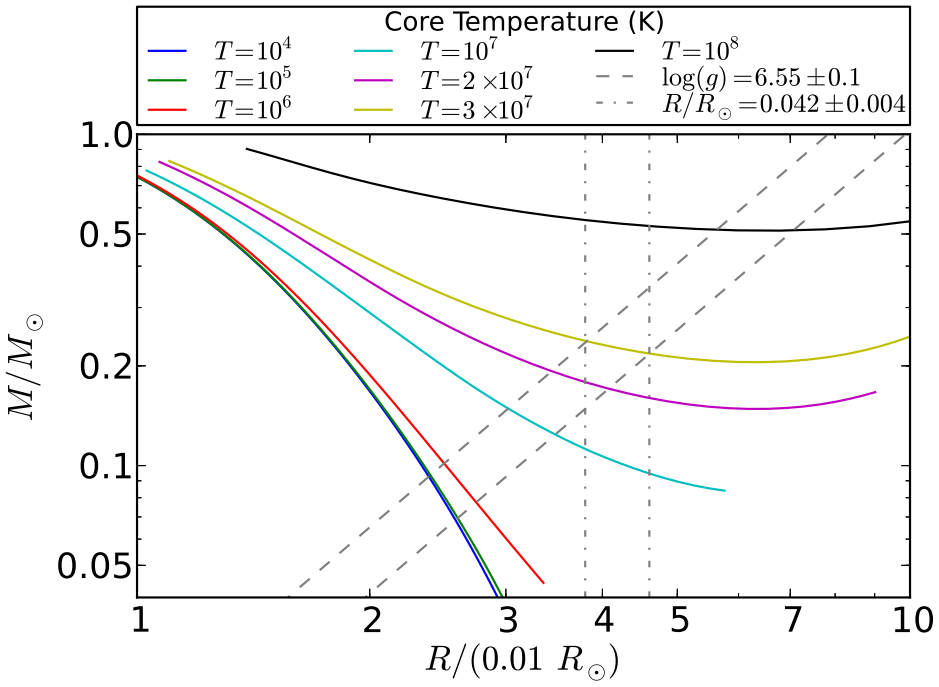

Figure 3.13: Logarithm of the surface gravity $\log(g) = \log(GM_{\rm WD}/R^2_{\rm WD})$ as a function of the radius for ^{4}He white dwarfs for selected interior temperatures from $T = 10^4$ K to $T = 10^8$ K. The dashed and dot-dashed lines indicate the maximum and minimum best-fit values of the surface gravity, $\log(g) = 6.55 \pm 0.1$ and photometric radii $R_{\rm WD} = 0.042 \pm 0.004 R_\odot$, respectively.

3.5 Conclusions

We have been generalized the Feynman-Metropolis-Teller treatment [1] of compressed matter to the case of finite temperatures. We have thus obtained the EOS formed by nuclei and electrons by solving the finite temperature relativistic Thomas-Fermi equation (3.6) within globally neutral Wigner-Seitz cells. We emphasize in this work on the electron component and the Coulomb interaction between ions and electrons fully computed within a relativistic Thomas-Fermi approach with finite sized nuclei, and therefore applicable to any relativistic regime

of the electrons and densities. This work generalizes other treatments based on either a uniform distribution of electrons or the classic Thomas-Fermi treatment; see e.g. [31]. The quantum corrections to the classic ideal ion fluid considered in this work can be straightforwardly introduced in their corresponding ranges of relevance as done in previous treatments; see e.g. [32, 33, 34, 42].

We have shown the general features of the new EOS and compared and contrasted the effects owing to the non-zero temperature with respect to the degenerate case. We have checked that the onset of the inverse β decay instability is not modified for temperatures $T \lesssim 10^8$ K and therefore the zero-temperature critical densities computed in Ref. [27] can be safely used. The enhancement and flattening of the electron density inside the cell for larger temperatures could have relevant effect in the pycnonuclear reaction rates in the interior of white dwarfs and/or in the low density layers of accreting neutron stars.

Deviations from the degenerate EOS have been shown to occur in the regions of interest of low-mass white dwarfs and in the outermost layers of neutron star crusts. Ultra-low mass white dwarfs, $M_{\rm WD} \sim 0.2 M_\odot$ [43, 30], have been found in binary systems with neutron stars companions. These objects have central densities $\lesssim 10^6$ g cm^{-3}, where the degenerate approximation breaks down and so thermal effects cannot be neglected. We have analyzed here the specific case of PSR J1738+0333, whose mass and radius was estimated in [30] using the evolutionary mass-radius relation of Panei et al. [40]. They obtained $M_{\rm WD} = 0.181^{+0.007}_{-0.005}$ M$_\odot$, $R_{\rm WD} = 0.037^{+0.004}_{-0.003}$ $R_\odot$, in agreement with the spectrometric and photometric data. We inferred for this object an internal temperature $T \approx 2$–3×10^7 K, and a mass $M_{\rm WD} \approx 0.2$ $M_\odot$ assuming for instance the photometric radius, $R = 0.042$ $R_\odot$, as the star radius. We checked also our result using the relation by Koester [41] between the internal and surface white dwarf temperatures, $T_{\rm eff}^4/g = 2.05 \times 10^{-10} T_c^{2.56}$. Using the surface temperature and the logarithm of the surface gravity obtained from the spectral analysis, $T_{\rm eff} = 9130$ K and $\log(g) = 6.55$, this relation gives $T_c \approx 2.6 \times 10^7$ K, in full agreement with our results.

Chapter 4

Globally and locally neutral neutron stars

In this chapter we present the new treatment of neutron stars, formulated by Belvedere et al.(2012), which fulfills global and not local charge neutrality. The equilibrium equations in such a model take into account the strong, weak, electromagnetic, and gravitational interactions within the framework of general relativity. The nuclear interactions are described by the exchange of the σ, ω, and ρ virtual mesons. The equilibrium conditions are given by the theoretical framework based on Einstein-Maxwell-Thomas-Fermi (EMTF) equations which conserve the "klein potentials" throughout the configuration. The solution of the EMTF coupled differential equations leads to a new structure of the star: a positively charged core at supranuclear densities, $\rho > \rho_{nuc} \sim 2.7 \times 10^{14}$ g/cm^{-3}, surrounded by an electron distribution of thickness $\gtrsim \hbar/(m_e c)$ and, at lower densities $\rho < \rho_{nuc}$, a neutral ordinary crust. Which consequently, leads a new mass-radius relation that differs from the one given by the Tolman-Oppenheimer-Volkoff equations that satisfy local charge neutrality.

4.1 General structure and composition

The neutron stars are the most compact stars in the universe. Owing to their very high densities in their cores overcoming the nuclear density, they can be treated as a unique astrophysical laboratories of superdense matter. Typical masses and

radii of these stars are of the order of $M \simeq 1.4 M_\odot$ and $R \simeq 10$ km, respectively. Since a neutron star can be subdivided into the three internal regions; the outer crust, the inner crust and the core, the structure of the neutron star depends of their composition. Below we briefly describe the structure of the neutron star.

1. **Outer crust**: extends from the bottom of the atmosphere to the layer of neutron drip density $\rho_{drip} \approx 4 \times 10^{11}$ g cm^{-3} and has a depth of a few hundred meters [36]. It is composed of ions and electrons. A very thin surface layer contains non-degenerate electron gas but in the deeper layers the electrons are degenerate. At $\rho \lesssim 10^4$ g cm^{-3} the electron plasma may be non-ideal and the ionization may be incomplete. At high densities the electron gas is almost ideal and the atoms are fully ionized, being actually bare atomic nuclei. At the base of the outer crust ($\rho = \rho_{drip}$) the neutrons start to drip out from the nuclei and form a free neutron gas.

2. **Inner crust**: extends from the density ρ_{drip} up to approximately nuclear density where the supranuclear core starts. It is composed of the electrons, free neutrons and neutron-rich atomic nuclei [44, 45]. The amount of free neutrons increases with density.

3. **Core**: It extends from approximately nuclear density all the way up to supranuclear center. It is composed mainly of neutrons n, protons p and electrons e. The composition of npe matter is determined mainly by the condition of β-equilibrium with respect to the reactions $n \rightarrow p + e + \bar{\nu}_e$, $p + e \rightarrow n + \nu_e$, where ν_e and $\bar{\nu}_e$ stand for electron neutrino and antineutrino, respectively. In the traditional literature it is also imposed the condition of local charge neutrality, which requires that the electron and proton number densities be equal, $n_p = n_e$. The electrons are ultrarelativistic while neutrons and protons, which interact via nuclear forces, constitute a strongly interacting Fermi-liquid.

4.2 Locally neutral neutron stars: the TOV equations

The structure of a non-rotating neutron star that satisfy local charge neutrality, and so it does not have any electromagnetic structure, is described by the hydrostatic equilibrium equations for a spherically symmetric body in general relativity, that is the Tolman-Oppenheimer-Volkoff (hereafter TOV) equations.

In the spherically symmetric case the spacetime metric is given by

$$ds^2 = e^{\nu(r)}c^2dt^2 - e^{\lambda(r)}dr^2 - r^2d\theta^2 - r^2\sin^2\theta d\varphi^2\,, \tag{4.1}$$

where the $\nu(r)$ and $\lambda(r)$ are only functions of the radial coordinate r.

The Einstein equations can be reduced to the hydrostatic equilibrium equations

$$\frac{d\nu(r)}{dr} = \frac{2G}{c^2}\frac{4\pi r^3 P(r)/c^2 + M(r)}{r^2\left[1-\frac{2GM(r)}{c^2r}\right]}\,, \tag{4.2}$$

$$\frac{dM(r)}{dr} = 4\pi r^2\frac{\mathcal{E}(r)}{c^2}\,, \tag{4.3}$$

$$\frac{dP(r)}{dr} = -\frac{1}{2}\frac{d\nu(r)}{dr}[\mathcal{E}(r)+P(r)]\,, \tag{4.4}$$

where we have introduced the mass enclosed at the distance r through $e^{-\lambda(r)} = 1-2GM(r)/(c^2r)$, $\mathcal{E}(r) = c^2\rho(r)$ is the energy-density and $P(r)$ is the total pressure. The TOV system of equations can be then integrated providing a closure relation between the pressure and the energy density, namely the equation of state.

As it is well known the classic work of Oppenheimer & Volkoff (1939) addresses the problem of equilibrium configurations composed only of degenerate neutrons. In the case when the protons and electrons are also considered, all the scientific literature on neutron stars assume that the condition of local charge neutrality applies identically to all points of the equilibrium configurations [46]. Therefore, the solutions in this more general case are also obtained on the base of the TOV equations.

Using the concept of Klein potentials, Rotondo et al. (2011) have recently proved the impossibility of imposing the condition of local charge neutrality in the simplest case of a self-gravitating system of degenerate neutrons, protons and electrons in β-equilibrium [47]: it has been shown that the consistent treatment of the above

system implies the solution of the general relativistic Thomas-Fermi equations, coupled with the Einstein-Maxwell ones; what they called Einstein-Maxwell-Thomas-Fermi (EMTF) system of equations, being the TOV equations thus superseded.

4.3 Globally neutral neutron stars: equilibrium equations

In this section we present the equilibrium equations of non-rotating neutron star satisfying global charge neutrality following the new approach formulated by Belvedere et al.[3].

4.3.1 Core

Since neutron stars cores have densities much larger than the nuclear density $\rho_{\text{nuc}} \sim 2.7 \times 10^{14}$ g/cm^3, approaches for the nuclear interaction between nucleons based on phenomenological potentials and non-relativistic many-body theories can not be used (see [48, 49]). A self-consistent relativistic and well-tested model for the nuclear interactions has been formulated in [50, 51, 48, 49]. Within this model the nucleons interact with σ, ω and ρ mesons through Yukawa-like couplings and assuming flat spacetime the equation of state of nuclear matter can be determined. It has been clearly stated in [47, 52] that, when we turn into the description of a neutron star configuration, the global description of the Einstein-Maxwell-Thomas-Fermi equations is mandatory. Associated to this system of equations there is a sophisticated eigenvalue problem, especially the one for the general relativistic Thomas- Fermi equation is necessary in order to fulfill the global charge neutrality of the system and to consistently describe the confinement of the ultrarelativistic electrons.

Assuming that the nucleons interact with σ, ω and ρ mesons through Yukawa-like couplings and assuming flat spacetime one can write the equation of state of nuclear matter. The relativistic mean field nuclear model of Boguta and Bodmer [53] is adopted by assuming the strong interactions between nucleons, in minimal

coupling approximation, with σ an isoscalar meson field that provides the attractive long-range part of the nuclear force; a massive vector field ω that models the repulsive short range and; in addition, a massive isovector field ρ that takes account surface as well as isospin effects of nuclei (see also [53, 54]). The self-interacting scalar field potential $U(\sigma)$ is assumed as a quartic polynom with adjustable coefficients.

The total Lagrangian density of the system is written as

$$\mathcal{L} = \mathcal{L}_g + \mathcal{L}_f + \mathcal{L}_\sigma + \mathcal{L}_\omega + \mathcal{L}_\rho + \mathcal{L}_\gamma + \mathcal{L}_{\rm int}, \tag{4.5}$$

where the Lagrangian densities for the free-fields are (we use in this section units with $\hbar = c = 1$)

$$\mathcal{L}_g = -\frac{R}{16\pi G}, \tag{4.6}$$

$$\mathcal{L}_\gamma = -\frac{1}{16\pi} F_{\mu\nu}F^{\mu\nu}, \tag{4.7}$$

$$\mathcal{L}_\sigma = \frac{1}{2}\nabla_\mu\sigma\nabla^\mu\sigma - U(\sigma), \tag{4.8}$$

$$\mathcal{L}_\omega = -\frac{1}{4}\Omega_{\mu\nu}\Omega^{\mu\nu} + \frac{1}{2}m_\omega^2\omega_\mu\omega^\mu, \tag{4.9}$$

$$\mathcal{L}_\rho = -\frac{1}{4}\mathcal{R}_{\mu\nu}\mathcal{R}^{\mu\nu} + \frac{1}{2}m_\rho^2\rho_\mu\rho^\mu, \tag{4.10}$$

where $\Omega_{\mu\nu} \equiv \partial_\mu\omega_\nu - \partial_\nu\omega_\mu$, $\mathcal{R}_{\mu\nu} \equiv \partial_\mu\rho_\nu - \partial_\nu\rho_\mu$, $F_{\mu\nu} \equiv \partial_\mu A_\nu - \partial_\nu A_\mu$ are the field strength tensors for the ω^μ, ρ and A^μ fields respectively, ∇_μ stands for covariant derivative and R is the Ricci scalar. For the fields A_μ, ω_μ, and ρ_μ the Lorenz gauge was adopted. The self-interaction scalar field potential $U(\sigma)$ is a quartic-order polynom (see e.g. [55]).

The Lagrangian density for the three fermion species is

$$\mathcal{L}_f = \sum_{i=e,N} \bar{\psi}_i \left(i\gamma^\mu D_\mu - m_i\right)\psi_i, \tag{4.11}$$

where ψ_N is the nucleon isospin doublet, ψ_e is the electronic singlet, m_i states for the mass of each particle-specie and $D_\mu = \partial_\mu + \Gamma_\mu$, being Γ_μ the Dirac spin connections.

The interacting Lagrangian density is, given by

$$\begin{aligned}\mathcal{L}_{\rm int} &= -g_\sigma\sigma\bar{\psi}_N\psi_N - g_\omega\omega_\mu J^\mu_\omega - g_\rho\rho_\mu J^\mu_\rho \\ &+ eA_\mu J^\mu_{\gamma,e} - eA_\mu J^\mu_{\gamma,N},\end{aligned} \tag{4.12}$$

where the conserved currents are

$$J^{\mu}_{\omega} = \bar{\psi}_N \gamma^{\mu} \psi_N, \tag{4.13}$$

$$J^{\mu}_{\rho} = \bar{\psi}_N \tau_3 \gamma^{\mu} \psi_N, \tag{4.14}$$

$$J^{\mu}_{\gamma,e} = \bar{\psi}_e \gamma^{\mu} \psi_e, \tag{4.15}$$

$$J^{\mu}_{\gamma,N} = \bar{\psi}_N \left(\frac{1+\tau_3}{2} \right) \gamma^{\mu} \psi_N. \tag{4.16}$$

The g_σ, g_ω and g_ρ are coupling constants of the σ, ω and ρ-fields, and e is the fundamental electric charge. The Dirac matrices γ^μ and the isospin Pauli matrices satisfy the Dirac algebra in curved spacetime (see e.g. [56] for details).

The mean-field approximation in which fermion-field operators are replaced by their expectation values is adopted (see [57] for details). Within this approximation, the full system of general relativistic equations can be written in the form

$$\mathrm{e}^{-\lambda(r)} \left(\frac{1}{r^2} - \frac{1}{r} \frac{d\lambda}{dr} \right) - \frac{1}{r^2} = -8\pi G T^0_0, \tag{4.17}$$

$$\mathrm{e}^{-\lambda(r)} \left(\frac{1}{r^2} + \frac{1}{r} \frac{d\nu}{dr} \right) - \frac{1}{r^2} = -8\pi G T^1_1, \tag{4.18}$$

$$V'' + \frac{2}{r} V' \left[1 - \frac{r(\nu' + \lambda')}{4} \right] = -4\pi e \, \mathrm{e}^{\nu/2} \mathrm{e}^{\lambda} (n_p - n_e), \tag{4.19}$$

$$\frac{d^2\sigma}{dr^2} + \frac{d\sigma}{dr} \left[\frac{2}{r} - \frac{1}{2} \left(\frac{d\nu}{dr} + \frac{d\lambda}{dr} \right) \right] = \mathrm{e}^{\lambda} \left[\partial_\sigma U(\sigma) + g_s n_s \right], \tag{4.20}$$

$$\frac{d^2\omega}{dr^2} + \frac{d\omega}{dr} \left[\frac{2}{r} - \frac{1}{2} \left(\frac{d\nu}{dr} + \frac{d\lambda}{dr} \right) \right] = -\mathrm{e}^{\lambda} \left(g_\omega J^0_\omega - m^2_\omega \omega \right), \tag{4.21}$$

$$\frac{d^2\rho}{dr^2} + \frac{d\rho}{dr} \left[\frac{2}{r} - \frac{1}{2} \left(\frac{d\nu}{dr} + \frac{d\lambda}{dr} \right) \right] = -\mathrm{e}^{\lambda} \left(g_\rho J^0_\rho - m^2_\rho \rho \right), \tag{4.22}$$

$$E^F_e = \mathrm{e}^{\nu/2} \mu_e - eV = \text{constant}, \tag{4.23}$$

$$E^F_p = \mathrm{e}^{\nu/2} \mu_p + \mathcal{V}_p = \text{constant},, \tag{4.24}$$

$$E^F_n = \mathrm{e}^{\nu/2} \mu_n + \mathcal{V}_n = \text{constant},, \tag{4.25}$$

where the last three equations are the conservation of the particle klein potentials, and we have been introduced the notation $\omega_0 = \omega$, $\rho_0 = \rho$, and $A_0 = V$ for the temporal components of the meson-fields. The chemical potential and number density of the i-specie are, respectively, given by

$$\mu_i = \partial\mathcal{E}/\partial n_i = \sqrt{(P_i^F)^2 + \tilde{m}_i^2} \tag{4.26}$$

and

$$n_i = (P_i^F)^3/(3\pi^2) \tag{4.27}$$

with Fermi momentum P_i^F.

The nucleons effective mass is

$$\tilde{m}_N = m_N + g_s\sigma, \tag{4.28}$$

the effective electron mass is

$$\tilde{m}_e = m_e \tag{4.29}$$

and the effective potentials $\mathcal{V}_{p,n}$ are given by

$$\mathcal{V}_p = g_\omega\omega + g_\rho\rho + eV\,, \tag{4.30}$$

$$\mathcal{V}_n = g_\omega\omega - g_\rho\rho\,. \tag{4.31}$$

The Klein potentials derive from the thermodynamic equilibrium conditions given by the statistical physics of multicomponent systems, applied to a system of degenerate neutrons, protons, and electrons within the framework of general relativity (see [52] for details). These constants are linked by the β-equilibrium between the matter constituents

$$E_n^F = E_p^F + E_e^F\,. \tag{4.32}$$

The electron density n_e is, via Eq. (4.23), given by

$$n_e = \frac{\mathrm{e}^{-3\nu/2}}{3\pi^2}[\hat{V}^2 + 2m_e\hat{V} - m_e^2(\mathrm{e}^\nu - 1)]^{3/2}\,, \tag{4.33}$$

where $\hat{V} \equiv eV + E_e^F$. Substituting Eq.(4.33) into Eq. (4.19) one obtains the general relativistic extension of the relativistic Thomas-Fermi equation recently introduced

for the study of compressed atoms [58, 27], see chapter 2. This system of equations has to be solved with the boundary condition of global neutrality; see [47, 52] and below for details.

The scalar density n_s, within the mean-field approximation, is given by the following expectation value

$$n_s = \langle \bar{\psi}_N \psi_N \rangle = \frac{2}{(2\pi)^3} \sum_{i=n,p} \int d^3k \frac{\tilde{m}_N}{\epsilon_i(p)}, \tag{4.34}$$

where $\epsilon_i(p) = \sqrt{p^2 + \tilde{m}_i^2}$ is the single particle energy.

The energy-momentum tensor of free-fields and free-fermions $T^{\mu\nu}$ of the system is

$$T^{\mu\nu} = T_f^{\mu\nu} + T_\gamma^{\mu\nu} + T_\sigma^{\mu\nu} + T_\omega^{\mu\nu} + T_\rho^{\mu\nu}, \tag{4.35}$$

where

$$\begin{aligned}
T_\gamma^{\mu\nu} &= -\frac{1}{4\pi}\left(F_\alpha^\mu F^{\alpha\nu} + \frac{1}{4} g^{\mu\nu} F_{\alpha\beta} F^{\alpha\beta}\right), && (4.36)\\
T_\sigma^{\mu\nu} &= \nabla^\mu \nabla^\nu \sigma - g^{\mu\nu}\left[\frac{1}{2}\nabla_\sigma \sigma \nabla^\sigma \sigma - U(\sigma)\right], && (4.37)\\
T_\omega^{\mu\nu} &= -\Omega_\alpha^\mu \Omega^{\alpha\nu} - \frac{1}{4} g^{\mu\nu} \Omega_{\alpha\beta}\Omega^{\alpha\beta} \\
&+ m_\omega^2 \left(\omega^\mu \omega^\nu - \frac{1}{2} g^{\mu\nu} \omega_\alpha \omega^\alpha\right), && (4.38)\\
T_\rho^{\mu\nu} &= -\mathcal{R}_\alpha^\mu \mathcal{R}^{\alpha\nu} - \frac{1}{4} g^{\mu\nu} \mathcal{R}_{\alpha\beta}\mathcal{R}^{\alpha\beta} \\
&+ m_\rho^2 \left(\mathcal{R}^\mu \mathcal{R}^\nu - \frac{1}{2} g^{\mu\nu} \rho_\alpha \rho^\alpha\right), && (4.39)\\
T_f^{\mu\nu} &= (\mathcal{E} + \mathcal{P}) u^\mu u^\nu - \mathcal{P} g^{\mu\nu}, && (4.40)
\end{aligned}$$

where the energy-density $\mathcal{E}$ and the pressure $\mathcal{P}$ are given by

$$\mathcal{E} = \sum_{i=n,p,e} \mathcal{E}_i, \qquad \mathcal{P} = \sum_{i=n,p,e} \mathcal{P}_i, \tag{4.41}$$

being $\mathcal{E}_i$ and $\mathcal{P}_i$ the single fermion fluid contributions

$$\begin{aligned}
\mathcal{E}_i &= \frac{2}{(2\pi)^3} \int_0^{P_i^F} \epsilon_i(p)\, 4\pi p^2 dp, && (4.42)\\
\mathcal{P}_i &= \frac{1}{3}\frac{2}{(2\pi)^3} \int_0^{P_i^F} \frac{p^2}{\epsilon_i(p)}\, 4\pi p^2 dp. && (4.43)
\end{aligned}$$

	NL3	NL-SH	TM1	TM2
m_σ (MeV)	508.194	526.059	511.198	526.443
m_ω (MeV)	782.501	783.000	783.000	783.000
m_ρ (MeV)	763.000	763.000	770.000	770.000
g_s	10.2170	10.4440	10.0289	11.4694
g_ω	12.8680	12.9450	12.6139	14.6377
g_ρ	4.4740	4.3830	4.6322	4.6783
g_2 (fm^{-1})	-10.4310	-6.9099	-7.2325	-4.4440
g_3	-28.8850	-15.8337	0.6183	4.6076
c_3	0.0000	0.0000	71.3075	84.5318

Table 4.1: Selected parameter sets of the σ-ω-ρ model.

It is important to recall that the equation of state (4.41)–(4.43) satisfies the thermodynamic law

$$\mathcal{E} + \mathcal{P} = \sum_{i=n,p,e} n_i \mu_i. \tag{4.44}$$

The coupling constants g_s, g_ω and g_ρ, and the meson masses m_σ, m_ω and m_ρ are usually fixed by fitting experimental properties of nuclei, e.g. saturation density, binding energy per nucleon (or experimental masses), symmetry energy, surface energy, and nuclear incompressibility. In Table 4.1 we present selected fits of the nuclear parameters. In particular, we show the following parameter sets: NL3 [59], NL-SH [60], TM1 [61], and TM2 [62].

The constants g_2 and g_3 that appears in the Table 4.1 are the third and fourth order constants of the self-scalar interaction as given by the scalar self-interaction potential

$$U(\sigma) = \frac{1}{2} m_\sigma^2 \sigma^2 + \frac{1}{3} g_2 \sigma^3 + \frac{1}{4} g_3 \sigma^4 \,. \tag{4.45}$$

The non-zero constant c_3 that appears in the TM1 and TM2 models corresponds to the self-coupling constant of the non-linear vector self-coupling $\frac{1}{4} c_3 (\omega_\mu \omega^\mu)^2$. They have not include such a self-coupling vector interaction in the general formulation presented above.

The core equations can be solved by numerical integration given a central density and the regularity conditions at the origin. Thus, the radius of the core $R_{\rm core}$ is given by $\mathcal{E}(r = R_{\rm core})/c^2 = \rho_{\rm nuc}$. These equations must be solved with the boundary conditions given by the fulfillment of the condition of global charge neutrality and the continuity of the Klein potentials of particles between the core and the crust.

4.3.2 Core-crust transition

The mean-field approximation for the meson-fields is not valid any longer in the crust. So, a full numerical integration of the meson-field equations of motion, taking into account all gradient terms, have to be made. We expect the core-crust transition boundary-layer to be a region with characteristic length scale of the order of the electron Compton wavelength $\sim \lambda_e = \hbar/(m_e c) \sim 100$ fm corresponding to the electron screening scale. Then, in the core-crust transition layer, the system of equations (4.17)–(4.25) reduces to

$$V'' + \frac{2}{r}V' = -e^{\lambda_{\rm core}} e J^0_{ch}\,, \tag{4.46}$$

$$\sigma'' + \frac{2}{r}\sigma' = e^{\lambda_{\rm core}}\left[\partial_\sigma U(\sigma) + g_s n_s\right]\,, \tag{4.47}$$

$$\omega'' + \frac{2}{r}\omega' = -e^{\lambda_{\rm core}}\left[g_\omega J^0_\omega - m^2_\omega \omega\right]\,, \tag{4.48}$$

$$\rho'' + \frac{2}{r}\rho' = -e^{\lambda_{\rm core}}\left[g_\rho J^0_\rho - m^2_\rho \rho\right]\,, \tag{4.49}$$

$$e^{\nu_{\rm core}/2}\mu_e - eV = \text{constant}\,, \tag{4.50}$$

$$e^{\nu_{\rm core}/2}\mu_p + eV + g_\omega\omega + g_\rho\rho = \text{constant}\,, \tag{4.51}$$

$$\mu_n = \mu_p + \mu_e + 2\,g_\rho\rho e^{-\nu_{\rm core}/2}\,, \tag{4.52}$$

due to the fact that the metric functions are essentially constant on the core-crust transition layer and thus we can take their values at the core-radius $e^{\nu_{\rm core}} \equiv e^{\nu(R_{\rm core})}$ and $e^{\lambda_{\rm core}} \equiv e^{\lambda(R_{\rm core})}$.

The system of equations of the transition layer has a stiff nature due to the existence of two different scale lengths. The first one is associated with the nuclear interactions $\sim \lambda_\pi = \hbar/(m_\pi c) \sim 1.5$ fm and the second one is due to the aforemen-

tioned screening length $\sim \lambda_e = \hbar/(m_e c) \sim 100$ fm. Thus, the numerical integration of Eqs. (4.46)–(4.52) has been performed subdividing the core-crust transition layer in the following three regions:

1. a mean-field-like region where all the fields vary slowly with length scale $\sim \lambda_e$,

2. a strongly interacting region of scale $\sim \lambda_\pi$ where the surface tension due to nuclear interactions dominate producing a sudden decrease of the proton and the neutron densities and,

3. a Thomas-Fermi-like region of scale $\sim \lambda_e$ where only a layer of opposite charge made of electrons is present producing the total screening of the positively charged core.

They have integrated numerically Eqs. (4.17)–(4.25) for the models listed in Table 4.1. The boundary conditions for the numerical integration are fixed through the following procedure. Assuming a value for the central baryon number density $n_b(0) = n_n(0) + n_p(0)$. From the regularity conditions at the origin we have $e^{-\lambda(0)} = 1$ and $n_e(0) = n_p(0)$.

The metric function ν at the origin can be chosen arbitrarily, e.g. $\nu(0) = 0$, due to the fact that the system of equations remain invariant under the shift $\nu \to \nu +$ constant. The right value of ν is obtained once the end of the integration of the core has been accomplished and duly matched to the crust, by fulfilling the following identity at the surface of the neutron star,

$$e^{\nu(R)} = e^{-\lambda(R)} = 1 - \frac{2GM(R)}{c^2 R}\,, \tag{4.53}$$

being $M(R)$ and R the total mass and radius of the star. Then, taking into account the above conditions, we solve the system (4.20)–(4.25) at the origin for the other unknowns $\sigma(0)$, $\omega(0)$, $\rho(0)$, $n_n(0)$, $n_p(0)$, $n_e(0)$.

The initial conditions for the numerical integration of the core-crust transition layer equations are determined by the final values given by the numerical integration of the core equations, i.e. taking the values of all the variables at the core-radius $R_{\rm core}$.

The equilibrium conditions given by the constancy of the Klein potentials (4.23)–(4.25) throughout the configuration, impose in the transition layer the following continuity condition

$$e^{\nu_{\rm core}/2}\mu_e^{\rm core} - eV^{\rm core} = e^{\nu_{\rm crust}/2}\mu_e^{\rm crust}. \tag{4.54}$$

where $\mu_e^{\rm core} = \mu_e(R_{\rm core})$, $eV^{\rm core} = eV(R_{\rm core})$, and $\mu_e^{\rm crust} = \mu_e(R_{\rm core} + \delta R)$, and $e^{\nu_{\rm crust}} \simeq e^{\nu_{\rm core}}$.

The electron chemical potential and the density decrease, in the boundary interface, until values $\mu_e^{\rm crust} < \mu_e^{\rm core}$ and $\rho_{\rm crust} < \rho_{\rm core}$. For each central density, an entire family of core-crust interface boundaries and, correspondingly, an entire family of crusts with different mass and thickness, exist. The configuration with $\rho_{\rm crust} = \rho_{\rm drip} \sim 4.3 \times 10^{11}$ g/cm^3 separates neutron stars with and without inner crust. In the so-called inner crust, the neutrons dripped from the nuclei in the crust form a fluid that coexist with the nuclei lattice and the degenerate electrons [63]. The presence of the neutron fluid in the crust changes the nuclear surface tension at the core radius, in close analogy to the reduction of the surface tension of the nuclei in the crust due to the presence of the dripped neutrons, see e.g. [63]) for details. This reduction of the nuclear tension is not taken into account in the nuclear parameters which are obtained to fit the properties of bare nuclei, see Table 4.1.

4.3.3 Crust

Turning now to the crust, it is clear from the recent treatment of white dwarfs [27] that also this problem can be solved by the adoption of Wigner-Seitz cells and from the relativistic Feynman-Metropolis-Teller (RFMT) approach [58] it follows that the crust is clearly neutral. Thus, the structure equations to be integrated are the TOV equations

$$\frac{d\mathcal{P}}{dr} = -\frac{G(\mathcal{E}+\mathcal{P})(M + 4\pi r^3\mathcal{P})}{r^2(1-\frac{2GM}{r})}, \tag{4.55}$$

$$\frac{dM}{dr} = 4\pi r^2\mathcal{E}, \tag{4.56}$$

where $M = M(r)$ is the mass enclosed at the radius r.

The EOS by Baym, Bethe and Pethick (BBP) [63] was adopted. The crust material is assumed to be formed by Wigner Seitz cells of nuclei surrounded by a uniform background of degenerate electrons and at densities larger than the neutron drip density also by degenerate neutrons.

In general, the matter energy density and the pressure can be written as the sum of the contribution due to baryons (neutrons and protons) and electrons as follows

$$\mathcal{E} = \mathcal{E}_e + \mathcal{E}_b, \tag{4.57}$$

$$P = P_e + P_b, \tag{4.58}$$

where the contribution due to degenerate electrons is given by

$$\mathcal{E}_e = \frac{2}{(2\pi)^3}\int_0^{P_e^F}\sqrt{p^2+m_e^2}\,4\pi p^2 dp, \tag{4.59}$$

$$P_e = \frac{1}{3}\frac{2}{(2\pi)^3}\int_0^{P_e^F}\frac{p^2}{\sqrt{p^2+m_e^2}}\,4\pi p^2 dp. \tag{4.60}$$

The total baryon energy density in this regime within the BBP model can be written as

$$\mathcal{E}_b = n_N E_N + (1 - V_N n_N)\mathcal{E}_n, \tag{4.61}$$

$$P_b = n^2\frac{\partial \mathcal{E}_b/n}{\partial n}, \tag{4.62}$$

where we have defined

$$E_N = A[(1-Y)m_n + Y m_p] + E(k,Y) + E_C + E_{surf}, \tag{4.63}$$

$$\mathcal{E}_n = n_n[E(k_n,0) + m_n], \tag{4.64}$$

and E_C and E_{surf} denote the Coulomb energy (including the lattice energy) and the surface energy of the nucleus, respectively. The number of nucleons and protons of the nucleus is denoted by A and N_p respectively, n_N is the number density of nuclei, V_N is the volume of the nucleus, the factor $1 - V_N\, n_N$ is the fraction of the total volume occupied by the neutron gas with wave number denoted by k_n. The

energy $E(k,Y)$ is given by

$$\begin{aligned} E(k,Y) &= E_k(k,Y) + \left[E(k,1/2) - \frac{3k^2}{10m_n}\right](1-3T^4+2T^6) \\ &+ \left[s\left(\frac{k}{k_0}\right)^2 - \frac{k^2}{6m_n}\right]T^2(1-T^2)^2 + \left[E(k,0) - \frac{3\cdot 2^{2/3}}{10}\frac{k^2}{m_n}\right](3T^4-2T^6) \\ &+ \left[\mu_p^{(0)} - \mu_n^{(0)} + 2^{2/3}\frac{k^2}{2m_n}\right]\frac{1}{4}(T^4-T^6) \end{aligned} \tag{4.65}$$

and the parameter T is given as a function of Y through

$$Y = \frac{1-T}{2} \equiv \frac{n_p}{n}. \tag{4.66}$$

In the above equations we have defined the quantities [63]

$$E_k(k,Y) = \frac{3\cdot 2^{2/3}}{10}\frac{k^2}{m_n}\left[Y^{5/3} + (1-Y)^{5/3}\right], \tag{4.67}$$

$$E(k,1/2) = -w_0 + \frac{K}{2k_0^2}(k-k_0)^2, \tag{4.68}$$

$$E(k,0) \simeq 19.74\tilde{k}^2 - \tilde{k}^3\left(\frac{40.4 - 11.088\tilde{k}^3}{1+2.54\tilde{k}}\right), \tag{4.69}$$

$$\mu_p^{(0)} = -\tilde{k}^3\left(\frac{218+277\tilde{k}}{1+8.57\tilde{k}^2}\right), \tag{4.70}$$

$$\mu_n^{(0)} = E(k,0) + \frac{1}{3}k\frac{\partial E(k,0)}{\partial k}, \tag{4.71}$$

where $\tilde{k} = k/(hc) \simeq 5.06\times 10^3 k$ is measured in fm^{-1}, k is measured in MeV, and the constants of the model fixed to fit experimental data on the masses of observed nuclei, are given by $w_0 = 16.5$ MeV, $k_0 = 1.43$ fm[1] , $K = 143$ MeV, and $s = 33$ MeV.

The equilibrium conditions of the system in this regime can be summarized as

$$E_{surf} = 2E_C, \tag{4.72}$$

$$\mu_n^{(N)} - \mu_p^{(N)} = \mu_e - (m_n - m_p), \tag{4.73}$$

$$\mu_n^{(N)} = \mu_n^{(G)}, \tag{4.74}$$

$$P^{(N)} = P^{(G)}, \tag{4.75}$$

where $\mu_n^{(N,G)}$ is the neutron chemical potential in nuclei and in the gas outside nuclei, and $\mu_p^{(N)}$ is the proton chemical potential inside nuclei. Here the chemical

potential of protons and neutrons does not include their rest-masses, whereas the electron chemical potential μ_e does. The pressure on a nucleus is denoted by $P^{(N)}$ and $P^{(G)}$ is the outside neutron pressure.

For the EOS of the inner crust was constructed a polytropic-like form using the numerical solutions. Denoting the pressure at nuclear density ρ_0 by P_0 , and the pressure at neutron drip density ρ_{drip} by P_{drip} an accurate formula describing the $P-\rho$ relation for the inner crust within the BBP model is

$$P = K_1 + K_2\rho^{\Gamma},\ k_1 = P_{drip} - K_2\rho_{drip}^{\Gamma},\ K_2 = \frac{P_0 - P_{drip}}{\rho_0 - \rho_{drip}},\ \Gamma \simeq 1.6926. \tag{4.76}$$

4.4 Comparison with traditional TOV treatment

In the traditional TOV treatment local charge neutrality as well as the continuity of the pressure and the density in the core-crust transition are assumed. This leads to explicit violation of the constancy of the Klein potentials throughout the configuration (see e.g. [47]). In such a case there is a smooth transition from the core to the crust without any density discontinuity and therefore the density at the edge of the crust is $\sim \rho_{\rm nuc} \sim 2.7 \times 10^{14}$ g/cm^3. The so-called inner crust in those configurations extends in the range of densities $\rho_{\rm drip} \lesssim \rho \lesssim \rho_{\rm nuc}$ while, at densities $\rho \lesssim \rho_{\rm drip}$, there is the so-called outer crust. In Fig. 4.1, the density profiles of configurations obtained from the traditional TOV treatment and with the treatment presented here are compared and contrasted.

The markedly differences both in mass and in the thickness of the crust between the ones obtained from the traditional TOV treatment and the new configurations presented here, leads to a very different mass-radius relations which we compare and contrast in Fig. 4.2.

4.5 Conclusions

We presented here the treatment of globally neutral neutron stars, formulated by Belvedere et al.(2012) [3]. We have shown the equilibrium equations that take into

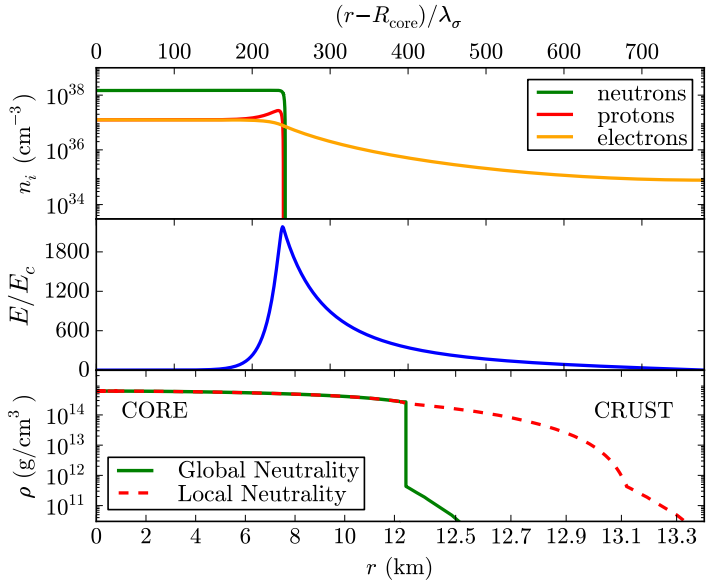

Figure 4.1: Upper panel: electric field in the core-crust transition layer, in units of the critical field E_c. Middle panel: particle density profiles in the core-crust boundary interface, in units of cm^{-3}. Lower panel: density profile inside a neutron star with central density $\rho(0) \sim 5\rho_{\rm nuc}$. The structural differences between the solution obtained from the traditional TOV equations (locally neutral case) and the globally neutral solution formulated by Belvedere et al.(2012).

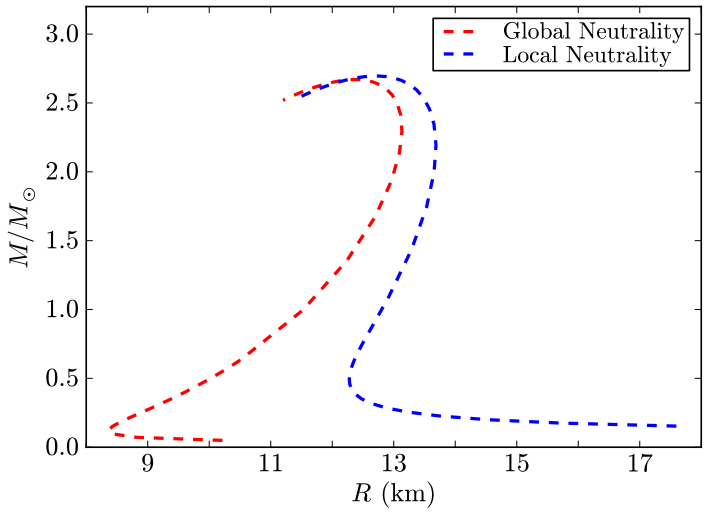

Figure 4.2: Mass-radius relation obtained with the traditional locally neutral TOV treatment case and the global charge neutrality configurations, with $\rho_{\text{crust}} = \rho_{\text{drip}}$ [3]. Configurations lying between the red and blue curves possess inner crust.

account the strong, weak, electromagnetic, and gravitational interactions within the framework of general relativity. The equilibrium conditions based on EMTF equations were also shown. This new treatment leads a new structure of the neutron star, which consequently, leads a new mass-radius relation. We compared and contrasted with the TOV-like neutron stars that satisfy local charge neutrality.

Chapter 5

Neutron star thermal evolution equations

Some properties of neutron stars, such as the EOS and the composition in their cores are still uncertain. All the microscopic calculations are model dependent an give us a variety of possible EOS with different compositions of the core. Since the thermal evolution of a neutron star is strongly correlated to the composition and EOS, simulating the neutron star cooling is one of the potential methods to probe the interior structure of these objects. As we will see in this chapter, the theoretical cooling curves depend on the adopted stellar interior, emissivities, heat capacity and thermal conductivity.

Neutron stars are born with temperatures around 10^{11} K, but gradually cool down in a process realized by two channels: neutrino emission from the stellar body and heat conduction from the internal layers in the surface resulting in a photon emission. We are neglecting the possible reheating mechanisms, the magnetic fields, and the superfluidity effects. All the considerations about the internal structure, EOS and the mass-radius relation are discussed in the chapter4 where we presented the new formulation of non-rotating neutron stars taking into account all the fundamental interactions and fulfilling global charge neutrality (Belvedere et al. 2012). The goal of this part of the work is to compute the cooling curves, namely the thermal evolution, of the neutron stars with global neutrality and to compare them with the locally neutral neutron star (TOV-like) cooling curves.

5.1 Basic Concepts

5.1.1 Observations

The detection of the thermal radiation is a complicated problem. Only midle-age ($t \sim 10^3 - 10^4$ yr) neutron stars can give us a reliably detected thermal radiation. This happens due to the complication in the extraction of the thermal radiation component from the observed spectra. For example, in young pulsars ($t < 10^3$ yr) processes in their magnetospheres may result in a strong nonthermal emission obscuring the thermal radiation. In the case of old pulsars ($t > 10^6$ yr), hot polar spots due to the pulsar activity produce radiation stronger than the thermal emission from the rest of the cooler stellar surface.

The thermal surface photon luminosity is given by

$$L = 4\pi R^2 \sigma T_s^4, \tag{5.1}$$

where σ is the Stefan-Boltzman constant, T_s and L are the effective surface temperature and luminosity as measured in the source rest-frame. The gravitationally redshifted luminosity and effective temperature observed at infinity, are

$$L^\infty = L e^{\nu(R)}, \tag{5.2}$$

$$T_s^\infty = T_s e^{\nu(R)/2}, \tag{5.3}$$

where $e^{\nu(R)} = g_{00}(R) = 1 - r_g/R$, with $g_{00}(R)$ the $0-0$ component of the metric and the Schwarzschild radius $r_g = 2M$, being M and R, the mass and radius of the star.

In order to compare observations with theory we need two important parameters of these stars, namely the effective surface temperature T_s and age t. In the Table 5.1 and Fig.5.1 taken from Yakovlev at al. 2004 [64], we can see the age and surface temperature of some isolated neutron stars and also where they can be found in the cooling curve, i.e. T_s-T diagram. These are the observed data that will be compared with the results of our simulations.

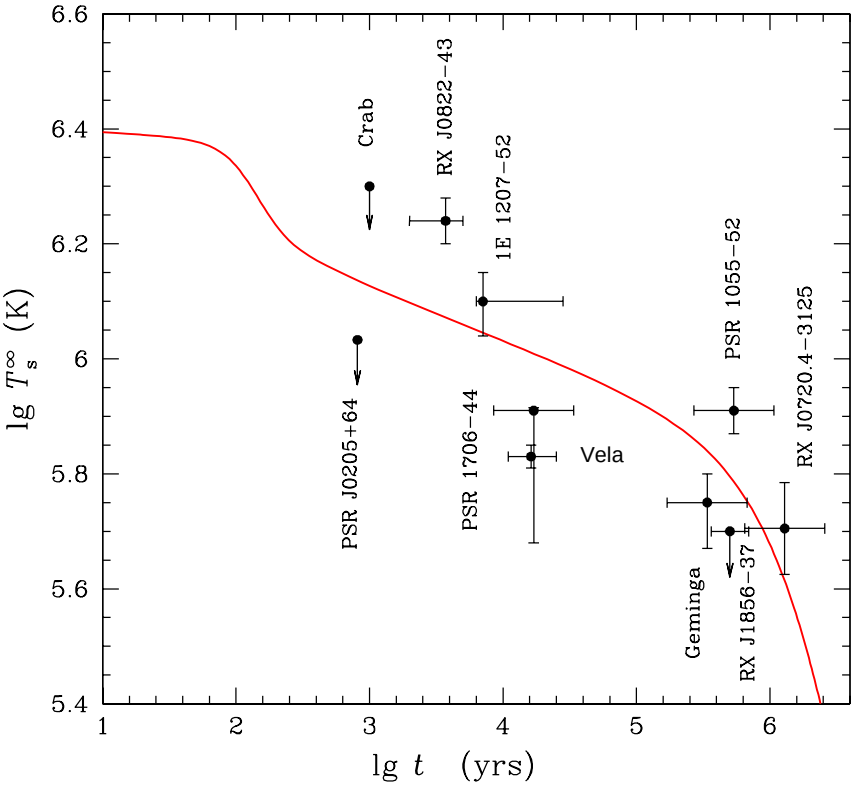

Figure 5.1: Observations of surface temperatures and upper bounds for several isolated neutron stars. The solid line is the basic theoretical cooling curve of a nonsuperfluid neutron star with $M = 1.3\,M_\odot$ (Taken from Yakovlev et al.(2004)).

Table 5.1: Observational limits on surface temperatures of isolated neutron stars (Taken from Yakovlev et al.(2004)).

Source	t [kyr]	T_s^∞ [MK]	Confid.	References
PSR J0205+6449	0.82	<1.1 [b)]		Slane et al. (2002)
Crab	1	<2.0 [b)]	99.7%	Weisskopf et al. (2004)
RX J0822–4300	2–5	1.6–1.9 [a)]	90%	Zavlin et al. (1999)
1E 1207.4–5209	$\gtrsim 7$	1.1–1.5 [a)]	90%	Zavlin et al. (1998)
Vela	11–25	0.65–0.71 [a)]	68%	Pavlov et al. (2001)
PSR B1706–44	~ 17	$0.82^{+0.01}_{-0.34}$ [a)]	68%	McGowan et al. (2004)
Geminga	~ 340	$0.56^{+0.07}_{-0.09}$ [b)]	90%	Halpern & Wang (1997)
RX J1856.4–3754	~ 500	<0.5	–	Pavlov & Zavlin (2003)
PSR B1055–52	~ 530	~ 0.7 [b)]	–	Pavlov (2003)
RX J0720.4–3125	~ 1300	~ 0.5 [a)]	–	Motch et al. (2003)

[a)] Inferred using a hydrogen atmosphere model

[b)] Inferred using the black-body spectrum

5.1.2 Thermal evolution equations

The general relativistic equations of thermal evolution that governs the cooling theory include the energy balance and the energy transport equations [65]. Following Gudmundsson et al.1983 [66], it is convenient to separate the neutron star in two parts: the hight density interior, which we shall call isothermal core[1], containing practically all the mass and thermal energy of the star, and an insulating envelope, which surrounds the core and which has no sources or sinks of energy. In what follows we will denote surface values by the subscript s and inner boundary values (at

[1]We call this region isothermal core although in the early, $t < 10 - 100$ yr, thermal evolution of the neutron star the full isothermality of this part is not achieved; see section6.1 for details.

the envelope-isothermal core boundary) by subscript b. In this physical separation the redshifted temperature, $Te^{\nu/2}$, in the core is uniform, whereas in the envelope there are temperature gradients.

At the temperatures of interest here ($T \lesssim 10^9$ K), neutrinos have a mean free path much larger than the radius of the star, and thus leave the star once they are produced. Thus, do not transport energy from one part to another.

The energy transport equation is so given by

$$\frac{L_d e^{\nu/2}}{4\pi r^2 \kappa} = -\sqrt{1-2m/r}\,\frac{\partial(Te^{\nu/2})}{\partial r}, \tag{5.4}$$

where L_d is the luminosity due the thermal conduction and radiation and κ is the thermal conductivity. Notice that an isothermal configuration, within the general relativistic framework, is defined by $e^{\nu/2}T =$ constant, insted of $T =$ constant.

We can write the neutrino luminosity equation as

$$\frac{\partial(L_\nu e^{\nu})}{\partial r} = -\frac{4\pi r^2}{\sqrt{1-2m/r}}\epsilon_\nu e^{\nu}, \tag{5.5}$$

where ϵ_ν is the neutrino emissivity per unit of volume. In non accreting neutron stars, there is no nuclear burning, and the equation of energy conservation can be written as

$$\frac{\partial(Le^{\nu})}{\partial r} = -\frac{4\pi r^2}{\sqrt{1-2m/r}}c_v\frac{\partial(Te^{\nu/2})}{\partial t}, \tag{5.6}$$

where L is the net luminosity, $L = L_d - L_\nu$; c_v is the specific heat per unit volume and t is the time measured by an observer at infinity, which is at rest with respect to the star. So, the energy balance equation is given by

$$\frac{\partial(L_d e^{\nu})}{\partial r} = -\frac{4\pi r^2}{\sqrt{1-2m/r}}\left[\epsilon_\nu e^{\nu/2} + c_v\frac{\partial(Te^{\nu/2})}{\partial t}\right]. \tag{5.7}$$

We have two boundary conditions required by the equations (5.4) and (5.7). The corresponding boundary conditions for L_d at the center, $r = 0$, is

$$L_d(r=0) = 0, \tag{5.8}$$

and the boundary condition associated with the temperature T_b at the inner boundary, $r = R_b$ to the luminosity l_b in this layer

$$T_b = T_b(L_d). \tag{5.9}$$

The location of this inner boundary layer is chosen such that L_b is equal to the total photon luminosity of the star at the surface, $L_b = L_d(r = R) \equiv L \equiv 4\pi R^2 \sigma T_s^4$. Therefore, we can write the equation (5.9) as $T_b = T_b(T_s)$; this "$T_b - T_s$" relationship is discussed further in the chapter 6.

In our calculations, following the results of [67, 68, 69] we set the envelope-core boundary at a density of $10^{10}\ g\,cm^{-3}$, and our results of thermal evolution will be presented using the effective temperature at infinity, T_s^∞ given by Eq.5.3 and related with the luminosity at infinity L^∞ through the radiation radius $R^\infty \equiv Re^{-\nu(R)/2}$ by

$$L^\infty \equiv 4\pi R^{\infty 2} \sigma T_s^{\infty 4}. \tag{5.10}$$

In the following sections, we present the main physical properties that determine the cooling theory, as well as a briefly review of the main cooling regulators, i.e. the neutrino emissivities, ϵ_ν, specific heat, c_v, and thermal capacity, κ.

5.1.3 Physical properties that determine the cooling

The cooling of neutron stars is mainly determined by the neutrino emissivity, heat capacity and thermal conductivity. All these ingredients depend on the composition and the stellar interior. The superfluidity, the magnetic fields and the presence of light elements on the surface are also important regulators which however we will not consider here. In this work we include all the relevant process of neutrino emission: in the core we consider the direct and modified Urca processes, neutron-neutron (nn), proton-proton (pp) and neutron-proton (np) Bremsstrahlung and in the crust, plasmon decay, e^-e^+ pair annihilation, and electron-nucleus (eN) Bremstrahlung. The heat capacity is given by electrons, protons and neutrons in the core and by electrons, atomic nuclei and free neutrons in the crust as well as the thermal conductivity in the core is a sum of the conductivities of electrons and neutrons instead in the crust is assumed to be as a result of the electrons scattering off atomic nuclei [70, 65].

The aim of the cooling theory is to calculate the thermal evolution, i.e. the evolution of the temperature with time (cooling curves) and compare with the observations. We can divide the cooling curve in three main different cooling phases:

1. The thermal relaxation phase ($t \lesssim 10 - 100yr$): the heat flows inward from the crust to the core on a conduction time-scale, as a cooling wave propagates from the core to the crust. During this stage the crust is hotter than the core, and they remain thermally decoupled. At the end of this phase, the scenario is a neutron star with an isothermal core, at $r < R_b$, and a radiative envelope, at $R_b \leq r \leq R$, where R_b is the boundary radius of the isothermal core with the envelope and corresponds to a density $\rho_b \approx 10^{10}\ g\,cm^{-3}$. More details will be given in the section 6.1.

2. The neutrino cooling phase ($t \lesssim 10^5 yr$): in this phase the neutrino emission from the stellar interior is the mainly responsable to produce the cooling, whereas the surface temperature adjust to the internal one. Namely, $L_\nu \gg L_\gamma$ where $L_\gamma = L_d$ is the photon luminosity.

3. The photon cooling phase ($t \gtrsim 10^5 yr$): during the photon cooling phase the neutron star cools mainly by photon emission from the surface. Namely, $L_\nu \ll L_\gamma$.

Further details about the cooling curves and the different phases can be found in the chapter 6.

5.2 Neutrino emission process

The dominant cooling mechanism is the neutrino emission from the interior of the neutron star. There are several processes that produces neutrino in their interiors, we are going to briefly describe the most important here.

Since the core and the crust have different compositions, the neutrino emission processes in the crust or in the core have to be studied separately.

5.2.1 In the core

We can write the total neutrino emissivity in the core, ϵ_ν^{core}, as

$$\epsilon_\nu^{core} = \epsilon_{\nu,DU} + \epsilon_{\nu,MU} + \epsilon_{\nu,BR}, \tag{5.11}$$

where $\epsilon_{\nu,DU}$, $\epsilon_{\nu,MU}$ and $\epsilon_{\nu,BR}$ are the neutrino emissivities due to the direct Urca (DU), modified Urca (MU) and Bremsstrahlung processes (BR).

Direct Urca process

The called Urca reactions are

$$n \rightarrow p + e + \bar{\nu}_e, \tag{5.12}$$

$$p + e \rightarrow n + \nu_e, \tag{5.13}$$

which bring nucleons into beta-equilibrium, where the chemical potentials satisfy the equality $\mu_n = \mu_p + \mu_e$ ([71]).

The emissivities for this process are given by [72]

$$\epsilon_{\nu,DU} = 4.0 \times 10^{27} \left(\frac{Y_e n_B}{n_0} \right) \frac{m_n^* m_p^*}{m_n^2} T_9^6 \, \Theta \; erg \, cm^{-3} \, s^{-1}, \tag{5.14}$$

where $Y_e = n_e/n_B$ is the electron fraction, n_B is the baryon number density, and $n_0 = 0.16 \; fm^{-3}$ is the equilibrium density of nuclear matter, T_9 is the temperature in units of 10^9 K, m_n^* and m_p^* are the effective neutron and proton mass respectively. Θ is the threshold factor, that can be 1 or 0 depending if the reaction takes place or not.

This is the simplest and most powerful neutrino emission process. The direct Urca processes, are only possible in neutron stars if the proton fraction exceeds a critical threshold. Otherwise, the energy and momentum cannot be conserved simultaneously for these reactions. So, the Direct Urca Process can only take place if the following triangle inequality is satisfied [71]

$$K_{Fn} < K_{Fp} + K_{Fe}, \tag{5.15}$$

where K_n^F, K_p^F, and K_e^F are the Fermi momentum of the neutron, proton and electron respectively.

Modified Urca process

If the proton fraction is below the threshold given by the inequality (5.15), the direct Urca process is not possible. In this case is necessary a bystander particle to allow

the momentum conservation. This processes was proposed by Chiu and Salpeter (1964). The called modified Urca processes are described by the reactions [71]

$$n + n \rightarrow n + p + e^{-} + \bar{\nu},$$

$$p + n \rightarrow p + p + e^{-} + \bar{\nu}.$$

The emissivities are given by

$$\epsilon_{\nu,MU,n} = 8.55 \times 10^{21} \left(\frac{m_n^*}{m_n}\right)^3 \left(\frac{m_p^*}{m_p}\right) \left(\frac{n_e}{n_0}\right)^{1/3} T_9^8 \, \alpha_n \beta_n \; erg \, cm^{-3} \, s^{-1}, \tag{5.16}$$

$$\epsilon_{\nu,MU,p} = 8.53 \times 10^{21} \left(\frac{m_p^*}{m_p}\right)^3 \left(\frac{m_n^*}{m_n}\right) \left(\frac{n_e}{n_0}\right)^{1/3} T_9^8 \, \alpha_p \beta_p \, F_p \; erg \, cm^{-3} \, s^{-1}, \tag{5.17}$$

where

$$F_p = \frac{(n_e^{1/3} + 3n_p^{1/3} - n_n^{1/3})^2}{(8 n_e^{1/3} n_p^{1/3})}, \tag{5.18}$$

and $\alpha_n = \alpha_p = 1.76 - 0.63(n_n/n_0)^{-2/3}$ and $\beta_n = \beta_p = 0.68$.

Nucleon-nucleon Bremsstrahlung process

Neutrinos can be generated by nucleon-nucleon scattering in the core, this process is called nucleon-nucleon Bremsstrahlung. This reactions becomes possible when neutral currents are considered and have been studied by Flowers et al. (1975) and Friman and Maxwell (1979). The nucleon-nucleon Bremsstrahlung reactions are [71]

$$n + n \rightarrow n + n + \nu + \bar{\nu},$$
$$n + p \rightarrow n + p + \nu + \bar{\nu},$$
$$p + p \rightarrow p + p + \nu + \bar{\nu}.$$

The emissivities are given by

$$\epsilon_{\nu,BR,nn} = 7.33 \times 10^{19} \left(\frac{m_n^*}{m_n}\right)^4 \left(\frac{n_n}{n_0}\right)^{1/3} T_9^8 \; erg \, cm^{-3} \, s^{-1}, \tag{5.19}$$

$$\epsilon_{\nu,BR,pp} = 1.70 \times 10^{19} \left(\frac{m_p^*}{m_p}\right)^4 \left(\frac{n_p}{n_0}\right)^{1/3} T_9^8 \; erg \, cm^{-3} \, s^{-1}, \tag{5.20}$$

$$\epsilon_{\nu,BR,np} = 7.33 \times 10^{19} \left(\frac{m_n^* m_p^*}{m_n m_p}\right)^2 \left(\frac{n_p}{n_0}\right)^{1/3} T_9^8 \; erg\, cm^{-3}\, s^{-1}. \tag{5.21}$$

Summarizing, the processes that we have in the core are: modified Urca and nucleon-nucleon Bremsstrahlung and the direct Urca where the triangle inequality (5.15) is satisfied.

5.2.2 In the crust

As we saw in the chapter 4, the main differences between the globally neutral neutron star and the TOV-like neutron stars are in the mass and thickness of the crust. The crust is composed by neutrons, electrons and ions in the inner crust and by electrons and ions in the outer crust. Since the number density of neutrons in the inner crust is smaller than the electron density in most of the inner crust and much more massive than the electrons, the contribution of the neutrons to the emission properties of the inner crust are usually neglected. Therefore, the total neutrino emissivities in the crust is given by

$$\epsilon_\nu^{crust} = \epsilon_{\nu,BR} + \epsilon_{\nu,pair} + \epsilon_{\nu,pl}, \tag{5.22}$$

where we are considering the emissivities of the electron Bremsstrahlung process, $\epsilon_{\nu,BR}$, the $e^- e^+$ annihilation, $\epsilon_{\nu,pair}$, and due the plasmon decay $\epsilon_{\nu,pl}$, which we describe below.

Electron Bremsstrahlung

The electron Bremsstrahlung is one of the major energy loss process in the neutron star crust. Here, the neutrinos are emitted due the electromagnetic interactions of electrons with the atomic nuclei. The mechanism was proposed by Pontecorvo (1959) and by Gandel'man and Pinaev (1959), and it can be written as

$$e + (Z, A) \rightarrow e + (Z, A) + \nu + \bar{\nu}. \tag{5.23}$$

The neutrino emissivity due the electron Bremsstrahlung, according to Kaminker et al. [73] is given by

$$\epsilon_{\nu,BR} = 10^x \; erg\, cm^{-3}\, s^{-1}, \tag{5.24}$$

where $x = 11.204 + 7.304\tau + 0.2976r - 0.37\tau^2 + 0.188\tau r - 0.103r^2 + 0.0547\tau^2 r - 6.77\log(1 + 0.228\rho/\rho_0)$ and $\tau \equiv \log T_8$, $\rho_0 = 2.8 \times 10^{14}\ g\ cm^{-3}$, $r \equiv \ln \rho_{12}$ with $\rho_{12} = \rho/10^{12}$, and ρ is the rest-mass density.

e^-e^+ Annihilation

The positrons and electrons annihilate producing neutrino pair emission in a process that can be written as

$$e + e^+ \rightarrow \nu + \bar{\nu}. \tag{5.25}$$

This process is most efficient at high temperature plasmas and low densities. It was proposed by Chiu and Morrison (1960) and independently by M. Levine (1964). The neutrino emissivity from e^-e^+ annihilation has a complicated expression, see e.g. [74], but for our purpose it is enough to adopt

$$\epsilon_{\nu,pair} \approx Q_c \equiv \frac{G_F^2}{\hbar}\left(\frac{m_e c}{\hbar}\right)^9 \approx 1.023 \times 10^{23}\, erg\, cm^{-3}\, s^{-1}, \tag{5.26}$$

where Q_c is the Compton neutrino emissivity and G_F is the Fermi weak interaction constant.

Plasmon decay

A free electron cannot emit a neutrino pair, it is forbidden by the energy momentum conservation. However, such a process is allowed if the electron interacts with the surrounding medium. Plasmon decay is an example of this process [71]. Following a treatment of the proper collective modes in terms of the plasmons, we can write the process as

$$\Gamma \rightarrow \nu + \bar{\nu}, \tag{5.27}$$

where Γ is the plasmon. This mechanism is efficient at hight temperatures but not at high densities. It was first considered in detail by Inman and Ruderman (1964) and the neutrino emissivity is given by

$$\epsilon_{\nu,pl} = 0.9248\frac{Q_c}{96\pi^4\alpha}\left(\frac{T}{T_r}\right)^9 (16.23 f_p^6 + 4.604 f_p^{7.5}) e^{-f_p}, \tag{5.28}$$

where the electron relativistic temperature $T_r = m_e c^2/k_B \approx 5.93 \times 10^9\ K$, and the electron plasma parameter f_p is given by

$$f_p \equiv \frac{\hbar w_{pe}}{k_B T} = \frac{\hbar\sqrt{4\pi e^2 n_e/\mu_e}}{k_B T}, \tag{5.29}$$

being μ_e the electron chemical potential and $w_{pe} = \sqrt{4\pi e^2 n_e/\mu_e}$ is the electron plasma frequency.

5.3 Heat capacity

The heat capacity per unit volume of the particle specie j is

$$c_{v,j} = \frac{k_B^2}{3\hbar^3} T \mu_j K_{Fj}, \tag{5.30}$$

where $\mu_j = \sqrt{K_{Fj}^2 + m_j^{*2}}$ is the chemical potential and K_{Fj} is the Fermi momentum.

The heat capacity in the core is the sum of the contributions from neutrons, protons and electrons. In the crust it is given by neutrons, electrons and atomic nuclei (vibration of ions in Coulomb lattice). The explicit expression for the heat capacity of the core and crust are presented below [64, 70].

5.3.1 In the core

The total heat capacity per unit volume can be written as

$$c_v^{core} = c_{v,e} + c_{v,p} + c_{v,n}, \tag{5.31}$$

where $c_{v,e}$ is the specific heat for the electrons, $c_{v,p}$ for the protons and $c_{v,n}$ for the neutrons. The specific heat for the electrons is given by

$$c_{v,e} = \frac{K_B^2}{3\hbar^3}\, T \sqrt{K_{Fe}^2 + m_e^2}\, K_{Fe}, \tag{5.32}$$

and the one for protons and neutrons can be written as

$$c_{v,i} = \frac{k_B^2}{3\hbar^3}\, T \sqrt{K_{Fi}^2 + m_i^{*2}}\, K_{Fi},\ i = p, n. \tag{5.33}$$

5.3.2 In the crust

The total heat capacity per unit volume in the crust is given by

$$c_v^{crust} = c_{v,e} + c_{v,n} + c_{v,ion}, \tag{5.34}$$

with $c_{v,e}$ and $c_{v,n}$ have the same expression as the specific heat of the electrons and neutrons in the core given by the Eqs.5.32 and 5.33 respectively, and $c_{v,i}$ is the specific heat contribution from the plasmon which we adopt from [75]. At low temperatures, when $T \ll T_p$ electrons dominate ($T_p = \hbar w_{ion}/k_B$ is the ion plasma temperature and $w_{ion} = (4\pi e^2 n_{ion} Z^2/m^*_{ion})^{1/2}$ is the ion plasma frequency), but the phonon contribution can became important where $T \simeq 10^8 - 10^9$ K. For a temperature $T \lesssim 0.45 T_p$ the contributions from lattice is given by

$$c_{v,ion} = \frac{2\pi^2}{15}\left(\frac{T^3}{\nu_l^3} + \frac{2T^3}{\nu_t^3}\right), \tag{5.35}$$

with the longitudinal velocity of the lattice phonon denoted as ν_l and the transverse velocity as ν_t.

If the strong interactions between the neutrons and the ion lattice are not taken into account, the velocities can be easily calculated as $\nu_l = \sqrt{K_{ion-e}/\rho}$, where the bulk-modulus of the electron-ion system is $K_{ion-e} = \rho\partial(P_{ion} + P_e)/\partial\rho$ and the ion mass density $\rho = A\, m_n\, n_{ion}$, where A is the number of bound nucleons in the ion. Since, $P_e \gg P_{ion}$, we can write the velocities

$$\nu_l = \sqrt{\frac{\partial P_e}{\partial \rho}} = \frac{w_{ion}}{K_{TFe}}, \tag{5.36}$$

and

$$\nu_t = \sqrt{\frac{\Sigma}{\rho}} = a\frac{w_{pion}}{q_D}, \tag{5.37}$$

where $n_{ion} = 3/4\pi a^3$ is the number density of ions, m^*_{ion} is the effective mass, the electron screening momentum $K_{TFe} = \sqrt{4e^2/\pi} K_{Fe}$, the ion Debye momentum is $q_D = (6\pi^2 n_{ion})^{1/3}$, Σ is the shear modulus of the lattice and the constant $a = 0.4$ is obtained by numerical calculations of a Coulomb crystal. We have that $\nu_l \gg \nu_t$, then

the contributions from the longitudinal modes to $c_{v,ion}$ can be neglected. According to this, the lattice contribution can be written as

$$c_{v,ion} = \frac{12\pi^4}{5} n_{ion} \left(\frac{T}{0.45 T_p} \right)^3 . \tag{5.38}$$

5.4 Thermal Conductivity

5.4.1 In the core

For the thermal conductivity in the core we adopt the results by Flowers and Itoh (1981) [76]. For $T < T_F^p$, where T_F^p is the proton Fermi temperature, the thermal conducitivity is well fitted by

$$\kappa^{core} = 10^{23} \rho_{14} \, T_8^{-1} \, erg \, cm^{-1} \, s^{-1} \, K^{-1}, \tag{5.39}$$

where $\rho_{14} = \rho / 10^{14}$ and $T_8 = T / 10^8$.

5.4.2 In the crust

When the interior temperature of the neutron star, T, is smaller than the critical temperature for the onset of superfluidity, T_c, the number of thermally excited neutrons is exponentially suppressed and we can neglect the contributions to the thermal conductivity by the neutrons in the inner crust (more details can be found in [75]). The dependence of the critical temperature with the density was computed by Page and Reddy (2012) and found that the critical temperature for the crust is around 10^9 K. Since the neutron stars are born with temperatures around 10^{11} K but rapidly cool down to temperatures less than 10^9 K (as we will see in the section 6.1), the relation $T \ll T_c$ is always satisfied. So the conductivity in the crust is given only by electron-ion scattering.

The general formula of the thermal conductivity can be written as [65]

$$\kappa^{crust} = \frac{c_v v l}{3}, \tag{5.40}$$

where c_v is the specific heat, v is the particle velocity and λ the transport mean free path.

Using Eq.(5.30) and $l = v/\nu_e$, where ν_e is the effective relaxation frequency which depends on the ions properties at each density [77], the thermal conductivity in the crust can be written as

$$\kappa^{crust} = \frac{\pi^2 K_B^2 T n_e}{3\sqrt{(m_e^2 + k_e^2)}\nu_e}. \tag{5.41}$$

Since the frequency ν_e depends on several electron scattering mechanisms such as electron-ion, electron-electron, and electron-impurity scatterings no simple analytic form can be found. We use in this work the numerical results of [78].

5.5 Conclusion

The theoretical cooling curves depend on the adopted stellar interior, the neutrino emissivities, the heat capacity and the thermal conductivity. In this chapter we presented all the main regulators of the cooling theory. We reviewed all the relevant process of neutrino emission; in the core, the direct and modified Urca processes, neutron-neutron (nn), proton-proton (pp) and neutron-proton (np) Bremsstrahlung and in the crust, plasmon decay, e^-e^+ pair annihilation, and electron-nucleus (eN) Bremstrahlung. The heat capacity is given by electrons, protons and neutrons in the core and by electrons, atomic nuclei and free neutrons in the crust as well as the thermal conductivity in the core is a sum of the conductivities of electrons and neutrons instead in the crust is assumed to be as a result of the electrons scattering off atomic nuclei [70].

Chapter 6

Neutron star cooling curves

As we already mentioned in the chapter 5, the main goal of the cooling theory is to calculate the $T_s^\infty(t)$ or $L_\gamma^\infty(t)$ diagrams, and compare them with observations. In the cooling curve we can distinguish three different cooling stages: the thermal relaxation phase, the neutrino cooling phase, and the photon cooling phase, e.g. see section 5.1.3 and Fig.6.1.

In this chapter we present more details about the cooling stages and the results of our cooling simulations of the new model of neutron star, satisfying global charge neutrality instead of local charge neutrality (see chapter 4). We compute the cooling curves considering the isothermal approximation as well as using a more complete cooling theory that includes the thermal relaxation phase. Our results are compared with the observed data taken from Yakovlev et al. (2004) shown in the table 5.1.

6.1 Thermal relaxation phase

At birth, the neutron star core starts to cool quickly by neutrino emission, while the crust stays hot. So, at the beginning there exist a large temperature gradient inside the star. The heat gradually flows from the crust to core as a cooling wave propagation from the core to the crust. The time needed for the neutron star to become isothermal (apart from a non-isothermal thin envelope), is called thermal relaxation time. Consequently, the thermal relaxation time, t_w, is defined as a time for the cooling wave to reach the star surface.

Lattimer et al.[79] found by numerical simulations a scaling relation for the re-

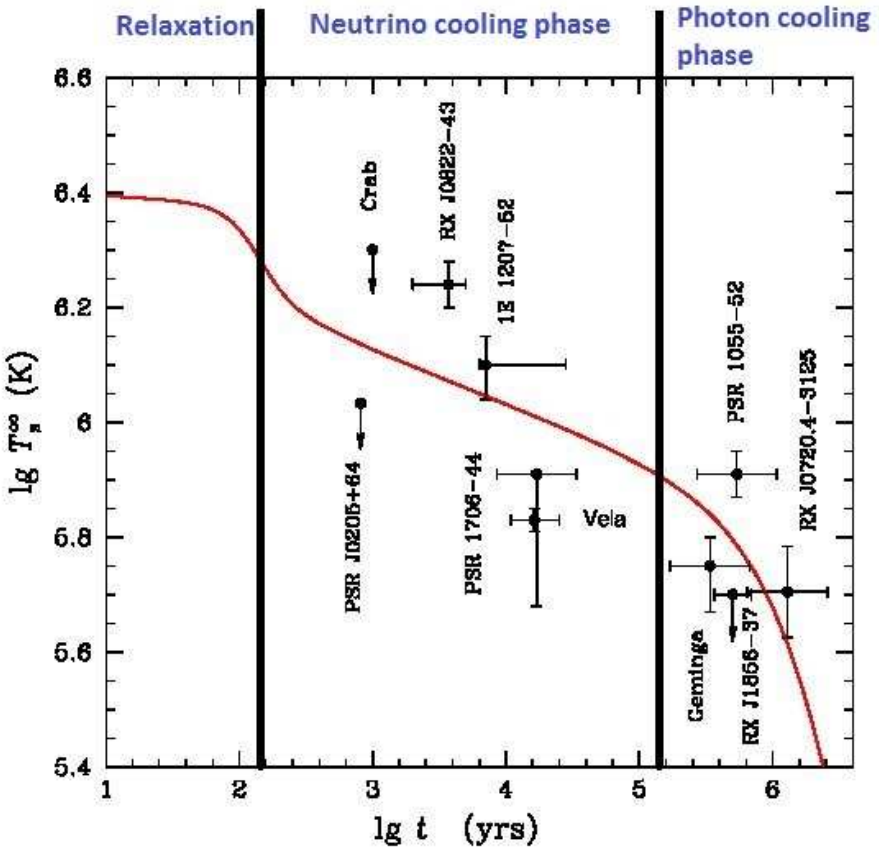

Figure 6.1: The basic theoretical cooling curve of a nonsuperfluid neutron star with $M = 1.3\,M_\odot$ (Taken from Yakovlev et al.(2004)) and the respective cooling phases.

laxation time, t_w, and the crust thickness, ΔR_{crust}

$$t_w \approx \alpha t_1, \tag{6.1}$$

where

$$\alpha = \left(\frac{\Delta R_{crust}}{1\,km}\right)^2 (1 - r_g/R)^{-3/2}, \tag{6.2}$$

and t_1 is the normalized relation time which depends on the microscopic properties of matter, such as the thermal conductivity and heat capacity [79].

This results can be understood as follows. We can write the dependence of t_w on the heat capacity, c_v, and thermal conductivity, κ using the general formula of the thermal conductivity Eq.(5.40) and the velocity $v = l/t_w$. The thermal relaxation time is then given by the simple estimate [70]

$$t_w = C_v l^2/\kappa, \tag{6.3}$$

where l is the width of a uniform slab, so $l = \Delta R_{crust}/\sqrt{1 - r_g/R}$. The other factor $\sqrt{1 - r_g/R}$ comes from the gravitational time dilatation.

As an example we show in Fig.6.2, taken from Gnedin et al. (2001), the thermal relaxation phase of a 1.7 $M_\odot$ neutron star. We can notice that, until the age of $1\,yr$, the region around $4 \times 10^{11}\ g\,cm^{-3}$ cools more effectively. The inner crust remains hotter if we compare with the outer crust that cools to 10^9 just in some days. After the first year, the gradient between the core and crust is wasted, as the cooling wave reaches the surface and the star forms an isothermal state in $50\,yr$.

Therefore, we can probe the internal properties of the neutron star crust observing the epoch of the thermal relaxation. In Fig.6.3, also taken from Gnedin et al.(2001), we can check the sensitivity of the relaxation time to test the variations of the physical properties, of the crust of a neutron star with $1.5\,M_\odot$. The values of t_w and t_1 are presented in the Tab.6.1.

6.2 Neutrino and photon cooling phases

At the end of the thermal relaxation phase, the neutron star thermal structure is composed by an isothermal core and a radiative thin envelope. The subsequent

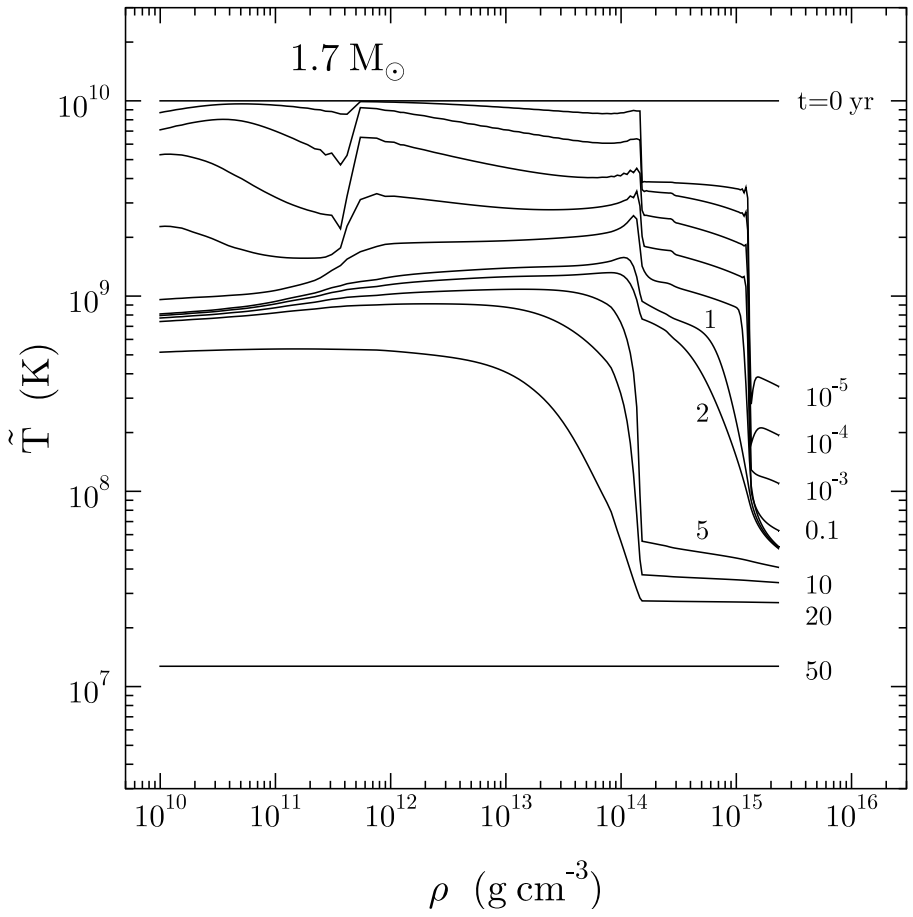

Figure 6.2: The gravitationally redshifted temperature $\tilde{T} = T\sqrt{1 - r_g/R}$ profiles in the 1.7 $M_\odot$ neutron star without superfluid effects. Contours are at 0, 10^{-5}, 10^{-4}, 10^{-3}, 10^{-2}, 10^{-1}, 2, 5, 10, 20, and 50 yr. This figure was taken from Gnedin et al.(2001).

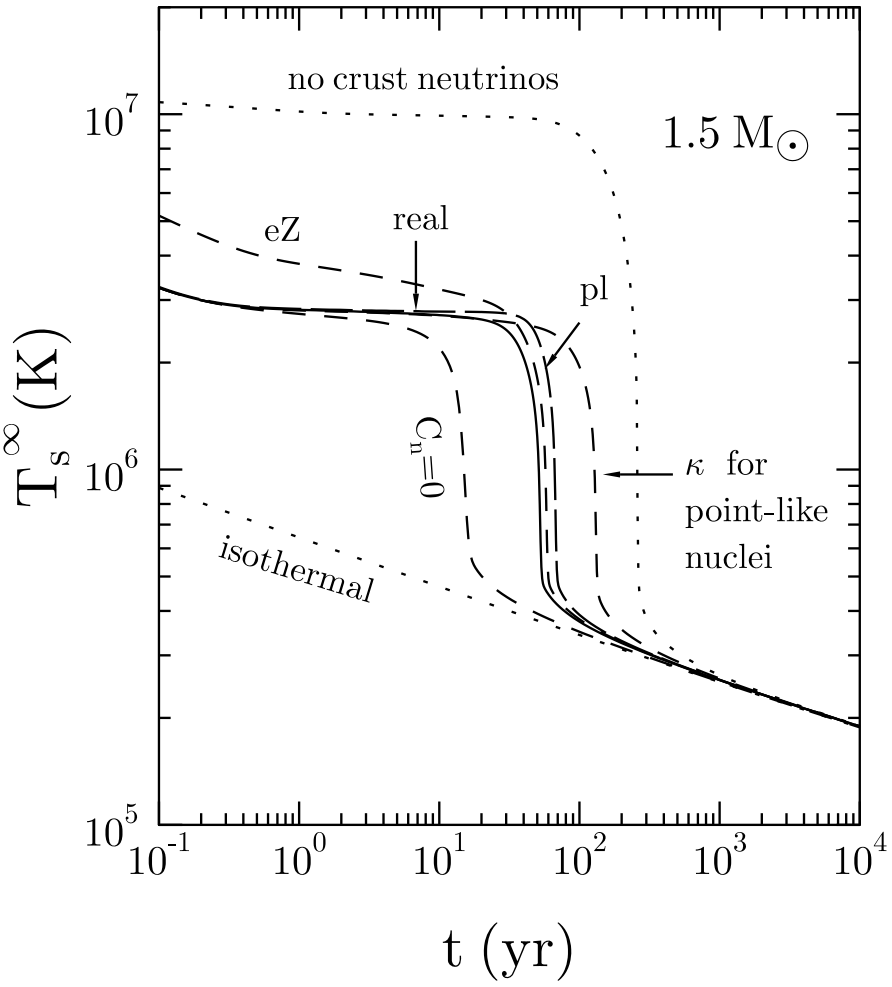

Figure 6.3: Thermal relaxation for the 1.5 $M_\odot$ model of Gnedin et al. (2001) without superfluid effects. Solid line: the real cooling curve. Dotted lines: switched off neutrino emission from the crust (upper) or infinite thermal conductivity at $\rho > 10^{10}$ g cm^{-3} (lower). The dashed curve $C_n = 0$: removed neutron heat capacity in the crust. Another dashed curve: the thermal conductivity κ in the crust is for point-like nuclei. Two other dashed lines: removed all neutrino mechanisms in the crust except either plasmon decay (pl) or electron-nucleus bremsstrahlung (*eZ*).

Table 6.1: Relaxation time t_w and normalized time t_1 for neutron stars with different crust models

test crust model	t_w^a (yr)	t_1^a (yr)	t_1^b (yr)
real model, no SF	52.4	28.8	33.9
no crust neutrinos	253.5	139.2	134.9
only plasmon decay neutrinos	67.6	37.1	41.6
only eZ neutrino bremsstr.	58.3	32.0	34.5
no neutron heat capacity	15.3	8.4	6.7
cond. for point-like nuclei	131.8	72.4	102.3
real model, weak crust SF	20.2	11.1	3.3
no Cooper neutrinos	29.0	15.9	19.0
weak core+crust SF	22.3	12.2	25.7
real model, strong crust SF	15.0	8.2	6.7
no Cooper neutrinos	15.5	8.5	6.9
strong core+crust SF	10.7	5.9	5.8

[a] for the 1.5 $M_\odot$ model, with $\alpha = 1.821$

[b] for the 1.3 $M_\odot$ model, with $\alpha = 2.875$

thermal evolution (cooling) of the neutron star can be divided in a "neutrino cooling phase“ followed by a ”photon cooling phase“, in which the dominant sink of energy is the neutrino emission from the isothermal core or the photons from the envelope, respectively.

6.2.1 Neutrino cooling phase: slow and fast cooling

In order to understand in simple terms this part of the thermal evolution, let us write the energy balance equation (5.7) in the Newtonian limit

$$\frac{\partial L_d}{\partial r} = -4\pi r^2 \left(\epsilon_\nu + c_v \frac{dT}{dt} \right), \tag{6.4}$$

where we have used the fact that at this stage the system is isothermal and so the temperature depends only on time. Integration of the above equation in space leads to

$$C_v \frac{dT}{dt} = -L_\nu - L_\gamma, \tag{6.5}$$

where $L_\gamma \equiv L_d(R) = 4\pi R^2 \sigma T_s^4$ is the surface photon luminosity, $L_\nu = \int \epsilon_\nu d^3r$ is the total neutrino luminosity, and $C_v = \int c_v d^3r$ is the total heat capacity.

We define the neutrino cooling phase as the stage during the thermal evolution of the neutron star where $L_\nu \gg L_\gamma$. In this phase we have that Eq.(6.5) becomes approximately

$$C_v \frac{dT}{dt} \approx -L_\nu. \tag{6.6}$$

As we have seen in the previous chapter, the neutrino emissivities in the supranuclear core (which are dominant) are proportional to the interior temperature to some power n whose value depends on the process. So we have $\epsilon_\nu \propto T^n$, see Eqs.(5.14) and (5.16-5.21).

On the other hand, the heat capacity per unit volume of degenerate fermion gas is proportional to the temperature, so we have $c_v \propto T$; see Eq.(5.30).

Therefore, assuming a system at constant density we can write the total neutrino luminosity and heat capacity as

$$L_\nu = NT^n, \tag{6.7}$$

$$C_v = CT, \tag{6.8}$$

where N and C are constants. Introducing Eqs.(6.7) and (6.8) into Eq.(6.6) we obtain

$$\frac{dT}{dt} = -\frac{N}{C} T^{n-1}, \tag{6.9}$$

from which we have after integration

$$T = T_0 \left[1 + \frac{N}{C}(n-2)T_0^{n-2}(t-t_0)\right]^{-\frac{1}{n-2}}, \tag{6.10}$$

where T_0 is the temperature at the initial time t_0.

Since in this neutrino cooling phase, $T \propto t^{-\frac{1}{n-2}}$, the velocity at which the neutron star cools is dictated by the value of the index n. The direct Urca process has $n = 6$ while the modified Urca and Bremsstrahlung have $n = 8$, so for these cases we obtain that the temperature decreases with time as $T \propto t^{-1/4}$ and $T \propto t^{-1/6}$, respectively. This implies that if the direct Urca process is active the neutron star cools much faster. For this reason, the direct Urca process is often known in the literature as a fast cooling mechanism and, correspondingly, the modified Urca, the Bremsstrahlung and any other mechanism with $n > 6$ are called slow cooling mechanisms.

6.2.2 Photon cooling phase

The neutrino luminosity L_ν has a strong dependence on the interior temperature; see Eq.(6.7). So the luminosity L_ν decreases strongly even for a small decrease of temperature. It is thus expected that at some point of the neutrino cooling phase the neutrino luminosity be of the order of the photon luminosity L_γ, and for further decrease of the temperature, $L_\gamma \gg L_\nu$. This latter stage is known as photon cooling phase.

In this case the balance equation (6.5) can be written approximately as

$$C_v \frac{dT}{dt} \approx -L_\gamma. \tag{6.11}$$

The photon luminosity is $L_\gamma = 4\pi R^2 \sigma T_s^4$ where T_s is the surface temperature of the neutron star, which is related to the interior temperature of the isothermal core by some $T_s - T$ relation that depends on the physics of the envelope.

Embracing the physics of the envelope in an index Λ such that $T_s \propto T^{0.5+\Lambda}$, the photon luminosity can be written in terms of the interior temperature as

$$L_\gamma = 4\pi R^2 \sigma T_s^4 = \frac{S}{C} T^{1+4\Lambda}, \tag{6.12}$$

where we have used Eq.(6.8). Integrating Eq.(6.12) from some time $t = t_1$ at which $T(t_1) = T_1$, we obtain

$$T = T_1 \left[1 + \frac{4\Lambda S}{C}(t - t_1)\right]^{-\frac{1}{4\Lambda}}. \tag{6.13}$$

As we will see below, Eq.(6.15), for neutron star envelopes $\Lambda \ll 1$ thus the thermal evolution during this photon cooling phase is very sensitive to the envelope physics through Λ and S.

6.3 The heat-blanketing envelope and $T_b - T_s$ relation

The problems of solving the hydrostatic equilibrium and thermal evolution equations, can be simplified by dividing the neutron star into two regions [66]: the interior ($r < R_b$), which we call isothermal core and the "heat-blanketing" envelope ($R_b \leq r \leq R$).

The heat-blanketing envelope is an upper thin layer in which a strong temperature gradient exists. It is defined as the layer extending from the surface, deep to the boundary density ρ_b, above which the star is isothermal. At this point the luminosity in the envelope is equal to the surface photon luminosity, $L_b(R_b) = L_d(R) = L$. The surface photon luminosity is related with the effective surface temperature by the equation (5.10). Therefore, these boundary conditions give us a relation between the temperature, at the isothermal core-envelope boundary at $r = R_b(\rho = \rho_b)$, T_b, and the surface temperature, T_s. This relationship is called "$T_b - T_s$ relation".

As shown by Gudmundsson et al. [66], we can reduce the full set of structure and thermal evolution equations to a single one in the envelope. This equation, which determines the thermal structure of the envelope, can be written as

$$\frac{dT}{dP} = \frac{3}{16}\frac{k}{T^3}\frac{T_s^4}{g_s}, \tag{6.14}$$

where P is the total pressure and k is the total opacity of the stellar matter.

Numerical calculations of this relation, obtained by integration of this equation, were first presented by Gudmundsson et al. [80, 66]. The following $T_b - T_s$ relation

for a heat blanketing iron envelope was obtained

$$T_b = 1.288 \times 10^8 (T_{s6}^4 / g_{s14})^{0.455} \ K, \tag{6.15}$$

where g_{s14} is the surface gravity $g_s = \frac{GM}{R^2}\sqrt{1 - r_g/R}$ in units of $10^{14}\ cm\,s^{-2}$ and $T_{s6} = T_s/(10^6\ \mathrm{K})$. This relation is accurate within 1.5% for $3.2 \times 10^5 g_{s14}^{1/4} \lesssim T_s \lesssim 3.2 \times 10^5 g_{s14}^{1/4}$ or equivalently $1.6 \times 10^7\ \mathrm{K} \lesssim T_b \lesssim 10^9\ \mathrm{K}$. Therefore, the index Λ in Eq. (6.12)

Potekhin et al.[78] extended these results to lower temperatures considering also light elements in the composition of the envelope. Since the thermal conductivity of the light element is higher than that of iron, a light element envelopes produces a higher effective temperature T_s and a higher luminosity L for a given isothermal core temperature T_b.

Hereafter we use the heat-blanketing envelope $T_s - T_b$ relation by Gudmundsson et al.[80] given by Eq.(6.15).

6.4 Results

In this section we present our results of the thermal evolution of globally neutral neutron stars. We also computed the fraction of the core where the direct Urca process is active for the case of the NL3 parameterization of the σ-ω-ρ nuclear model. As a first step towards the full calculation of the thermal evolution, we computed their evolution in the isothermal stage, which follows the thermal relaxation phase and we contrast the cooling curves with some observational data of middle-ages isolated neutron stars. Then, we present the our full cooling curves considering also the early phases where the star is far from isothermality and which reveals crucial information from the properties of the crust of the neutron star.

6.4.1 Occurrence of the direct Urca process

As shown in section 5.2.1 the direct Urca process, $n \to p + e + \bar{\nu}_e$ and $p + e \to n + \nu_e$, is possible in neutron star cores only if the fraction of particles involved in the reaction are such that the energy and momentum can be conserved simultaneously.

The process is then possible if the triangle inequality, $K_{Fn} < K_{Fp} + K_{Fe}$, is satisfied, where $K_{F,n,p,e}$ are the Fermi momenta of neutrons, protons, and electrons, respectively.

We computed the region in the core of the globally neutral neutron stars shown in Fig. 4.1 where the direct Urca process occurs. In Fig. 6.4 we show the size and mass fraction of the neutron star core where the process occurs as a function of the total mass of the star.

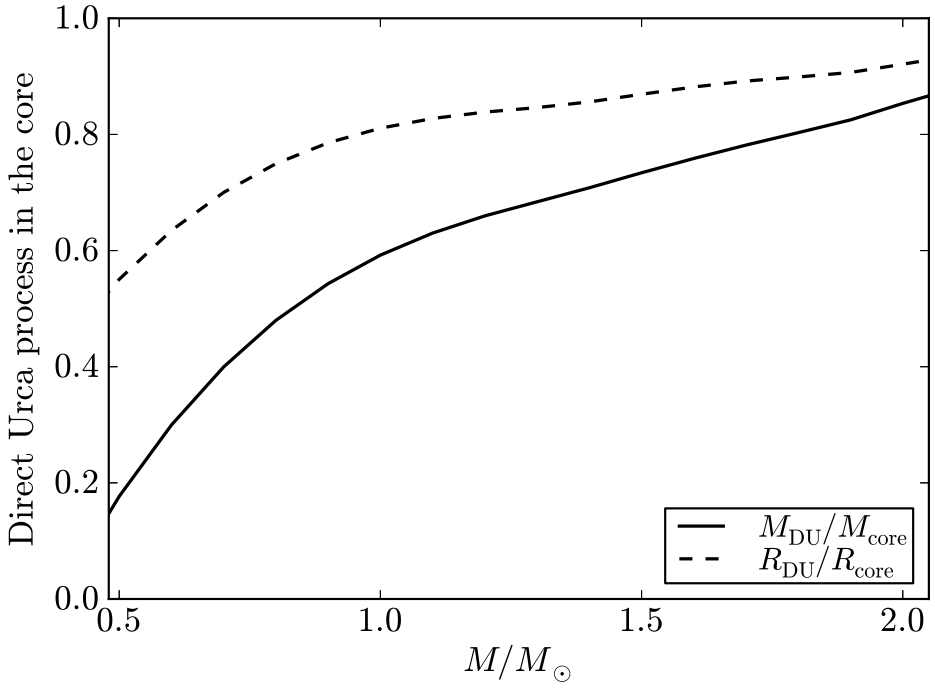

Figure 6.4: Fraction of the mass and size of the core of a globally neutral neutron star where the direct Urca process occurs.

6.4.2 Isothermal approximation

Most of the available observational data on the surface temperature of isolated neutron stars correspond to middle-ages, $t \sim 10^4$–10^6 yr, see e.g. [64]. By that times, the neutron star has already passed the thermal relaxation phase following the neutron star birth. The temperature gradient between the core and the crust has vanished and the thermal structure of the neutron star can be described as formed

by an isothermal core and a thin insulating envelope from where photons scape. The isothermal core extends from the center up to a boundary layer at density $\rho_b \approx 10^{10}$ g cm^{-3} [66], and the envelope is found at the lower density layers and where large temperature gradients exist.

The thermal relaxation epoch in which the isothermal core with temperature T_b is developed is of the order of $\Delta t \lesssim 100$ yr (see e.g. [70]), a time well within the ages of the observed isolated neutron stars, $t \sim 10^4$–10^6 yr. Therefore, lacking observational data at the early phases, we can start our thermal evolution, as a first approximation, from the point where the star already has reached the isothermality, so without considering the relaxation phase.

In the isothermal core, the energy balance and transport equations (5.4) and (5.7) become

$$\epsilon_\nu e^\nu + c_v \frac{\partial (T e^{\nu/2})}{\partial t} = 0, \quad \frac{\partial e^{\nu/2} T}{\partial r} = 0. \tag{6.16}$$

Considering all the neutrino emission processes and heat capacity discussed in the chapter 5, we computed the cooling curves by integrating numerically Eq. (6.16) with initial condition the temperature T_b. The surface temperature is calculated using the $T_b - T_s$ relation by [66] given by Eq.(6.15).

In the following we show our results for the surface temperature as observed at infinity, $T_s^\infty = e^{\nu(R)/2} T_s$ where $e^{\nu(R)/2} = \sqrt{1 - 2M/R}$. In Fig. 6.5 we show the surface temperature T_s as a function of the time t for a global neutrality neutron star with and without considering the occurrence of the direct Urca process in the core. It can be seen that when active, the direct Urca reactions make the star to cool faster with respect to the case when they are absent. The reason for this is, that this process has a neutrino emissivity $\epsilon_\nu \propto T^6$ while the other processes have $\epsilon_\nu \propto T^8$, which leads via Eq. (6.16), to $T \propto t^{-1/4}$ and $\propto t^{-1/6}$ respectively; see discussion in section 6.5 for details. The corresponding neutrino and photon luminosities are shown in Figs. 6.6 and 6.7, respectively.

We show in Fig. 6.8 the cooling curves for selected neutron star masses, 1.4 $M_\odot$ and 2.0 $M_\odot$, at the same central temperature, while Fig. 6.9 shows the evolution of a neutron star with 1.4 $M_\odot$ for two different central temperature, $T = 3 \times 10^9$ K and

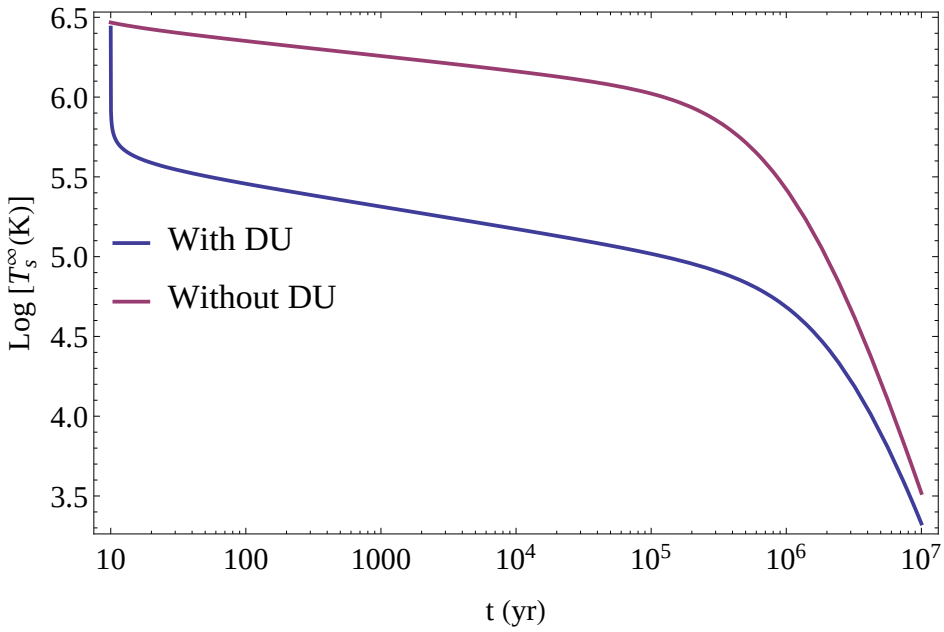

Figure 6.5: Surface temperature at infinity T_s^∞ as a function of time t in yr with (blue curve) and without (red curve) considering Direct Urca process (DU).

$T = 5 \times 10^9$ K. We contrast our theoretical curves with some isolated neutron stars observational data taken from Ref. [64].

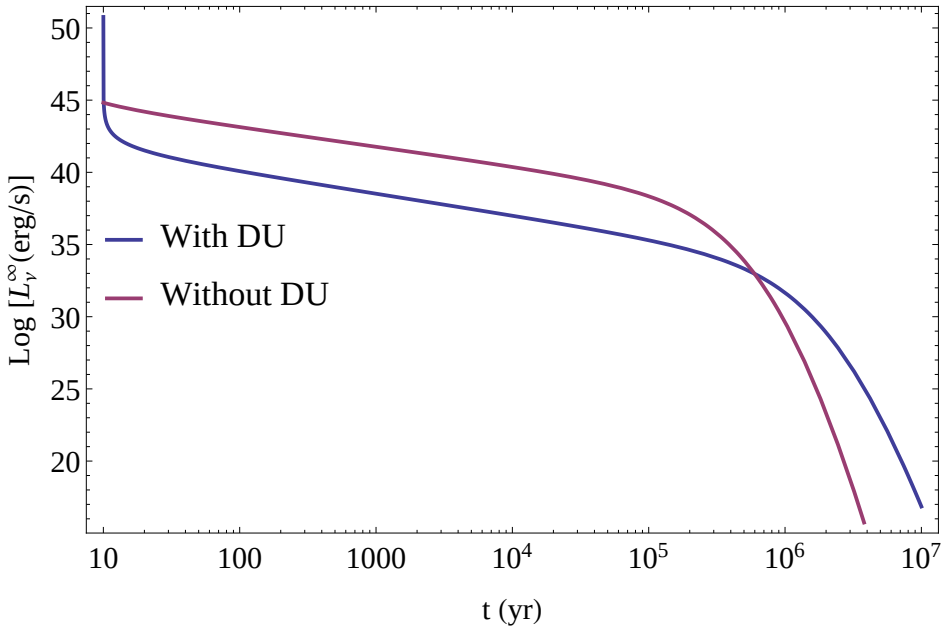

Figure 6.6: The logarithm of the neutrino lumminosity L_ν^∞ as a function of the time t (in yr) considering direct Urca process (DU), blue curve, and without considering the direct Urca, red curve.

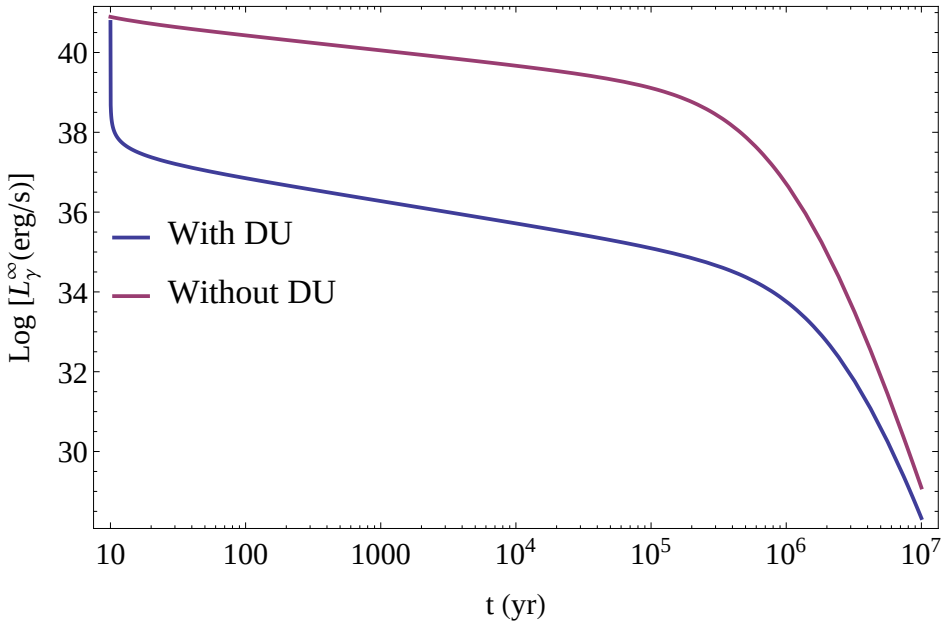

Figure 6.7: The logarithm of the photon lumminosity L_γ^∞ as a function of the time t (in yr) considering direct Urca process (DU), blue curve, and without considering the direct Urca, red curve.

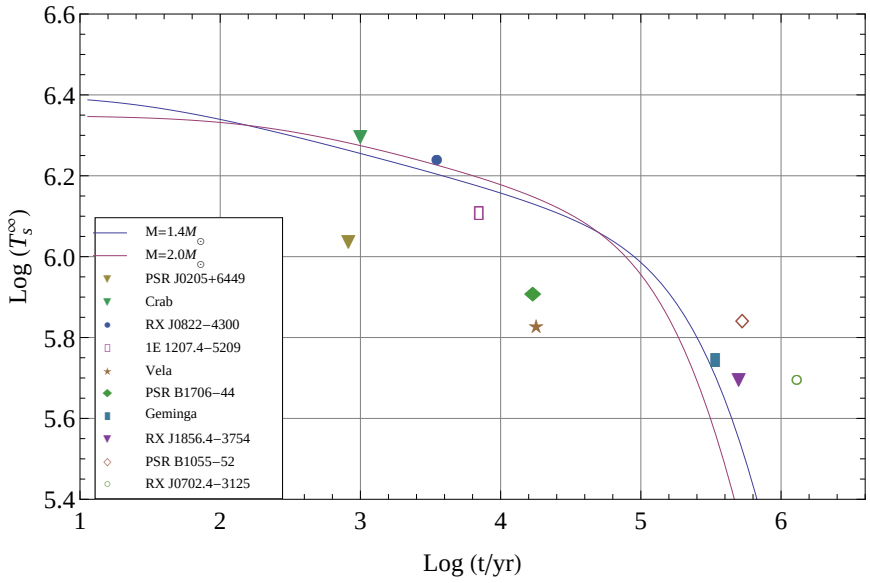

Figure 6.8: Surface temperature at infinity T_s^∞ as a function of time t in yr for two neutron star with slected masses, 1.4 $M_\odot$ and 2.0 $M_\odot$, at the same central temperature $T = 3 \times 10^9$ K.

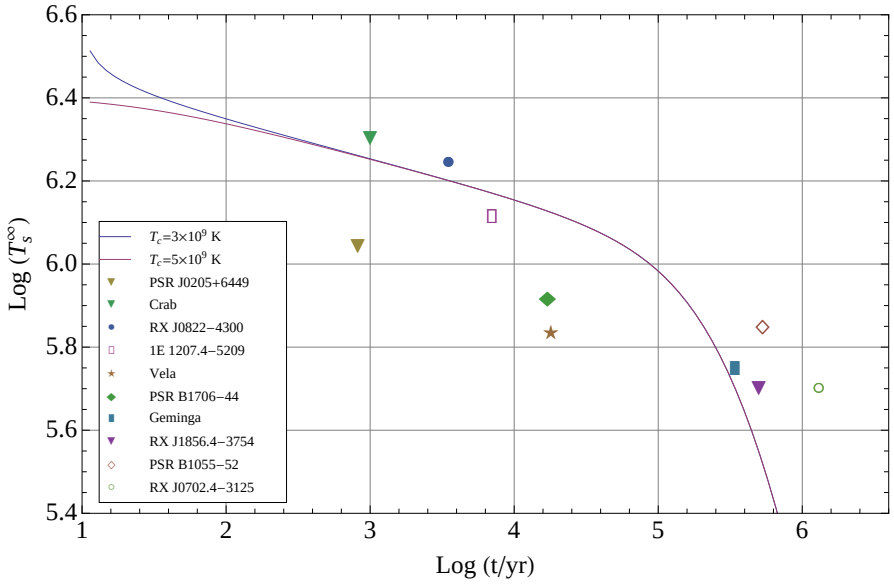

Figure 6.9: Surface temperature at infinity T_s^∞ as a function of time t for neutron star with selected central temperatures $T = 3 \times 10^9$ K and $T = 5 \times 10^9$ K, and mass 1.4 $M\odot$.

6.4.3 Full cooling curves

Now we present the complete thermal evolution of the globally neutral neutron star. The isothermal approach was abandoned and all the thermal evolution equations have been solved numerically. The thermal relaxation phase is present, which is crucial to reveal informations from the properties of the crust of the star. Then we can compare and contrast the differences between the cooling evolution of the globally and locally neutral neutron star since, as we have shown in chapter 4, the main difference between them is in the mass and size of the crust.

As we mentioned in the chapter 4, the new structure of the globally neutral neutron stars is very different from the traditional configurations obtained through the TOV equations (see Fig. 4.1): the core is positively charged as a consequence of the balance between gravitational and Coulomb forces that results in the appearance of a Coulomb potential energy $eV \sim m_\pi c^2$ deep. The core-crust transition starts at $\rho = \rho_{\rm nuc}$. The transition is marked by the existence of a thin, ΔR ∼few hundreds fm, electron layer fully screening the core charge. In this transition layer the electric field becomes overcritical, $E \sim m_\pi^2 c^3/(e\hbar)$, and the particle densities decrease until the base of the crust, which is reached when global charge neutrality is achieved. Consequently, the core is matched to the crust at a density $\rho_{\rm crust} \leq \rho_{\rm nuc}$; in Fig. 6.10 we present the density profiles of globally neutral neutron star with mass $M\ approx 1.4\ M_\odot$ for selected values of the density at the base of the crust, $\rho_{\rm crust}$.

Configurations with $\rho_{\rm crust} > \rho_{\rm drip}$ possess both inner and outer crust while in the cases with $\rho_{\rm crust} \leq \rho_{\rm drip}$ the neutron star have only outer crust. In the limit $\rho_{\rm crust} \to \rho_{\rm nuc}$, both ΔR and E of the transition layer vanish, and the solution approaches the one given by local charge neutrality (see Figs. 3 and 5 in [3]). All the above features lead to a new mass-radius relation of neutron stars; see [3] and Fig. 4.2.

Using a Fortran 90 code provided by Prof. R. Negreiros we computed the full cooling curves for globally neutral neutron star with mass $1.4\,M_\odot$ for different values of $\rho_{\rm crust}$. In the Fig. 6.11 we can see the surface temperature at infinity T_s^∞ as a function of time t in yr for the neutron star configurations shown in Fig. 6.10 and

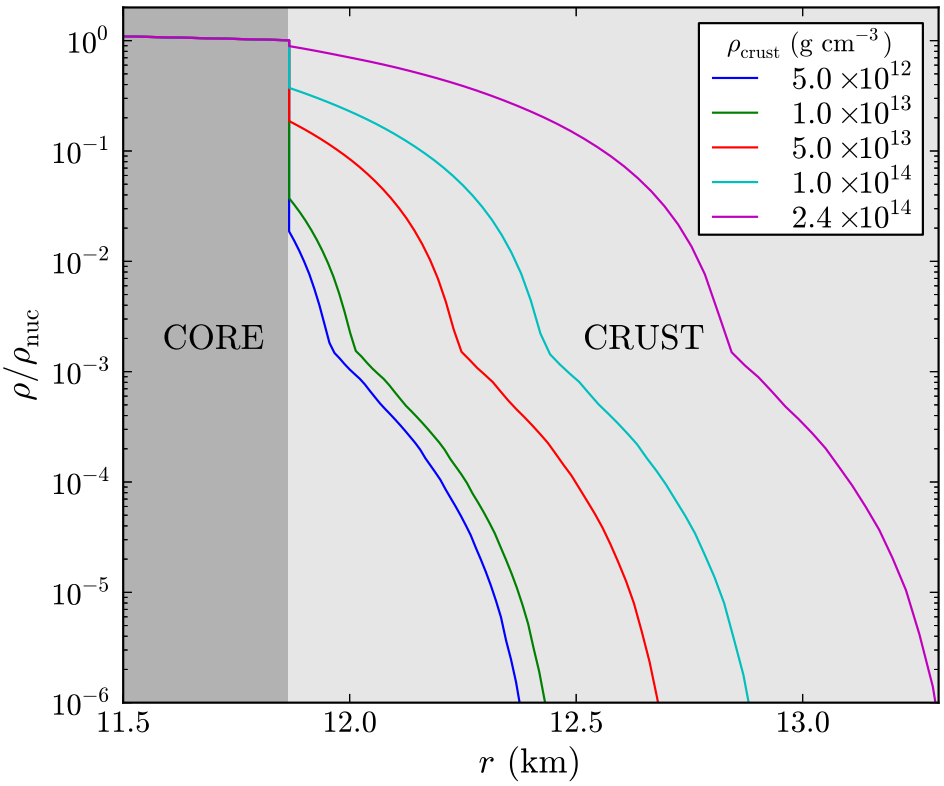

Figure 6.10: Density profiles of globally neutral neutron star with mass $M \approx 1.4\ M_{\odot}$ for selected values of the density at the base of the crust, $\rho_{\rm crust}$. Notice that the transition to the crust occurs at the nuclear saturation density, $\rho_{\rm nuc}$.

the Fig. 6.12 show the temperature at the base of the crust as a function of t for the same configurations. The Fig. 6.13 is an enlargement of the evolution of the surface temperature, T_s^∞, around its drop at the end of the thermal relaxation phase, for the neutron stars shown in Fig. 6.12. We can see in this figure that the time to the temperature drop is different for the star with densities higher and lower than 5×10^{13} g cm^{-3}.

For stars with $\rho \lesssim 5 \times 10^{13}$ g cm^{-3}: the thicker the crust the shorter relaxation time. In the case of stars with $\rho > 5 \times 10^{13}$ g cm^{-3}: the thicker the crust the longer the relaxation time. Since the latter behavior is in agreement with the results of Lattimer [79] given by Eq. (6.1) and Eq. (6.2), the former behavior found at densities $\rho \lesssim 5 \times 10^{13}$ g cm^{-3}, is in clear contrast. The reason for this is that in a very thin crust with a small or absent inner crust, some neutrino emission processes are blocked. This leads to a crust that is kept hotter for longer times.

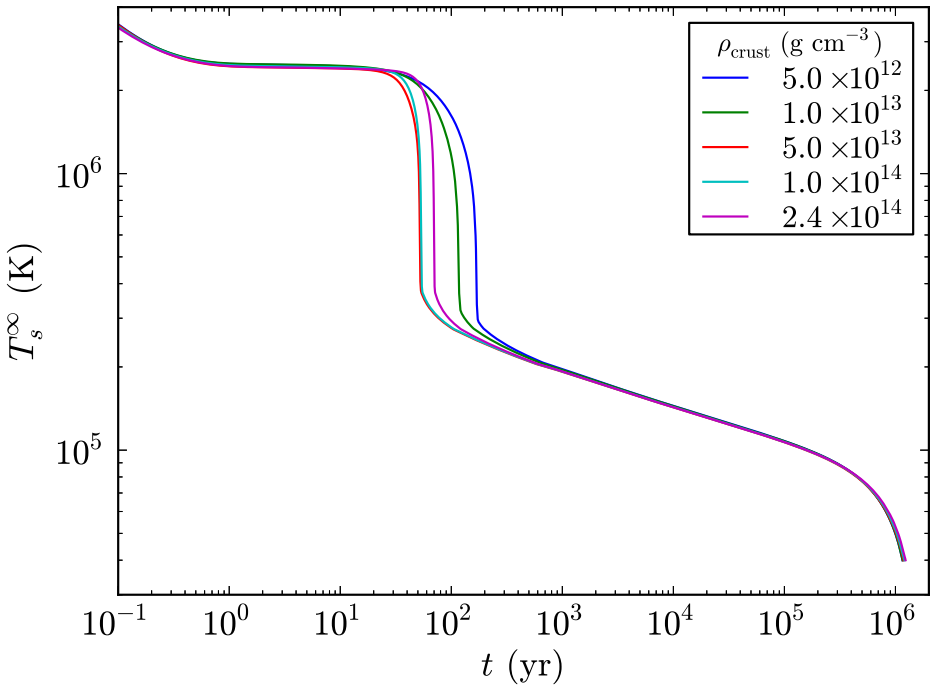

Figure 6.11: Surface temperature at infinity T_s^∞ as a function of time t in yr for the neutron star configurations shown in Fig. 6.10.

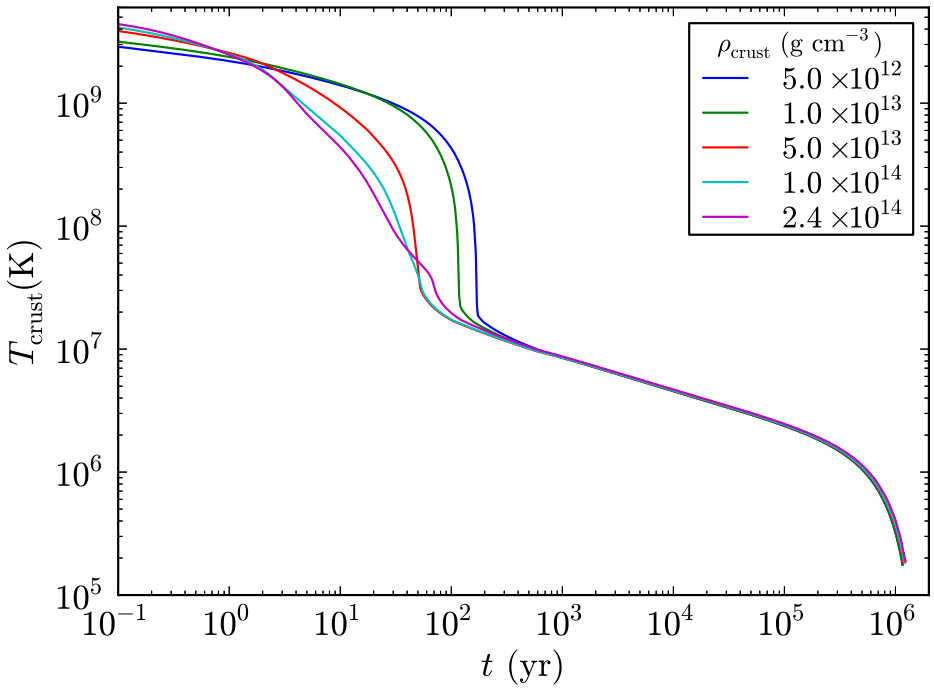

Figure 6.12: Temperature at the base of the crust as a function of time t in yr for the neutron star configurations shown in Fig. 6.10.

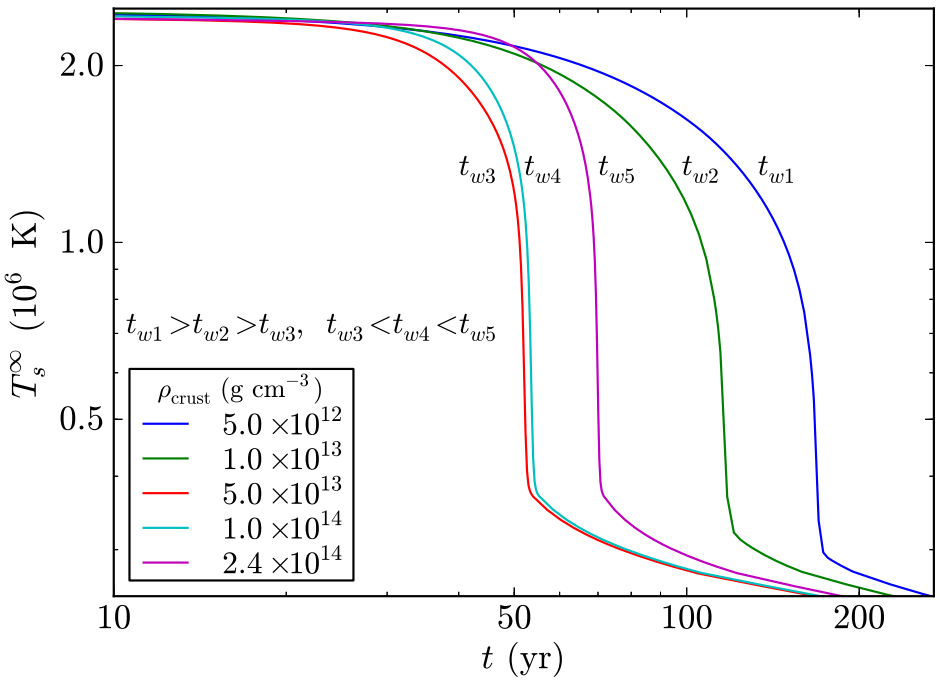

Figure 6.13: Enlargement of the evolution of the surface temperature, T_s^∞, around its drop at the end of the thermal relaxation phase, for the neutron stars shown in Fig. 6.12.

6.5 Conclusions

We presented in this chapter the results of our cooling simulations of globally neutral neutron star. The cooling curves have been computed considering the isothermal approximation, which was not take into account the thermal relaxation phase, as well as considering the complete cooling theory.

The size and mass fraction of the neutron star core where the direct Urca is active for the case of NL3 parametrization of the σ-ω-ρ nuclear model was also computed.

Considering the isothermal approximation, our results for the surface temperature T_s as a function of the time t for a global neutrality neutron star with and without considering the occurrence of the direct Urca process in the core have been shown. As was expected, the direct Urca reactions make the star to cool faster with respect to the case when they are absent. The corresponding neutrino and photon luminosities were also shown.

The full cooling curves were computed using a Fortran 90 code provided by Prof. R. Negreiros and we noticed different behavior at the end of the thermal relaxation phase, where the temperature drop, for the star with densities higher and lower than 5×10^{13} g cm^{-3}. We concluded that in a very thin crust with a small or absent inner crust, some neutrino emission processes are blocked keeping the crust hotter for longer times.

Chapter 7

Conclusion

In the chapter 2 we presented the recently description of a compressed atom within the global approach of the relativistic Feynman, Metropolis and Teller treatment [1] considering a Wigner-Seitz cell and applied to the construction of white dwarfs in the framework of general relativity. This treatment was the first approach of white dwarfs taking account gravitational, weak, strong and electromagnetic interactions. The results of the relativistic FMT treatment have been compared and contrasted with the results of the non-relativistic models of Chandrasekhar and Hamada and Salpeter [7].

We have been generalized, in the chapter 3, such a relativistic Feynman-Metropolis-Teller treatment [1] to the case of finite temperatures. We have thus obtained the EOS of a system of nuclei and electrons by solving the finite temperature relativistic Thomas-Fermi equation (3.6) within globally neutral Wigner-Seitz cells. We have shown the general features of the new EOS and compared and contrasted the effects owing to the non-zero temperature with respect to the degenerate case. We have checked that the onset of the inverse β decay instability is not modified for temperatures $T \lesssim 10^8$ K and therefore the zero-temperature critical densities computed in Ref. [27] can be safely used. The enhancement and flattening of the electron density inside the cell for larger temperatures could have relevant effect in the pycnonuclear reaction rates in the interior of white dwarfs and/or in the low density layers of accreting neutron stars.

Deviations from the degenerate EOS have been shown to occur for masses $< 0.7 M_\odot$ (or densities $\rho < 10^7$ g cm^{-3}) therefore of interest for low-mass white dwarfs

and the outermost layers of neutron star crusts. We have analyzed the specific case of the ultra low-mass white dwarf companion of the pulsar PSR J1738+0333. We inferred for this object an internal temperature $T \approx 2$–3×10^7 K, and a mass $M_{\rm WD} \approx 0.2\ M_\odot$ assuming for as radius the photometric value, $R = 0.042\ R_\odot$; in full agreement with the previous estimate, $M_{\rm WD} = 0.181^{+0.007}_{-0.005}\,{\rm M}_\odot$ and $R_{\rm WD} = 0.037^{+0.004}_{-0.003}\ R_\odot$, obtained in [30] using the evolutionary mass-radius relation of Panei et al. [40]. We checked also our result using the relation by Koester [41] between the internal and surface white dwarf temperatures, $T_{\rm eff}^4/g = 2.05 \times 10^{-10} T_c^{2.56}$. Using the surface temperature and the logarithm of the surface gravity obtained from the spectral analysis, $T_{\rm eff} = 9130$ K and $\log(g) = 6.55$, this relation gives $T_c \approx 2.6 \times 10^7$ K, also in line with our predictions.

In the chapter 4 we turned to neutron stars. We described the treatment of globally neutral neutron stars formulated by Belvedere et al.(2012) [3]. We have shown the equilibrium equations that take into account the strong, weak, electromagnetic, and gravitational interactions within the framework of general relativity. The equilibrium conditions based on Einstein-Maxwell-Thomas-Fermi equations were also shown. This new treatment leads a new structure of the neutron star, which consequently, leads a new mass-radius relation. We compared and contrasted with the TOV-like neutron stars that satisfy local charge neutrality.

In the chapter 5 we presented all the main regulators of the thermal evolution of neutron stars. The theoretical cooling curves depend on the adopted stellar interior, the neutrino emissivities, the heat capacity and the thermal conductivity. We reviewed all the relevant processes of neutrino emission; in the core, the direct and modified Urca processes, neutron-neutron (nn), proton-proton (pp) and neutron-proton (np) Bremsstrahlung and in the crust, plasmon decay, $e^- e^+$ pair annihilation, and electron-nucleus (eN) Bremstrahlung. The heat capacity is given by electrons, protons and neutrons in the core and by electrons, atomic nuclei and free neutrons in the crust as well as the thermal conductivity in the core is a sum of the conductivities of electrons and neutrons instead in the crust is assumed to be as a result of the electrons scattering off atomic nuclei [70].

We presented in the chapter 6 the results of our cooling simulations of globally

neutral neutron stars. The cooling curves have been computed first considering the isothermal approximation, and then accounting for the thermal relaxation phase, in which the core and the crust of the neutron star are thermally decoupled.

The size and mass fraction of the neutron star core where the direct Urca is active for the case of NL3 parametrization of the σ-ω-ρ nuclear model was also computed.

Considering the isothermal approximation, our results for the surface temperature T_s as a function of the time t for a globally neutral neutron star with and without considering the occurrence of the direct Urca process in the core have been shown. As expected, the direct Urca reactions make the star to cool faster with respect to the case when they are absent. The corresponding neutrino and photon luminosities were also shown.

In the case of the full cooling curves with the initial relaxation phase, we noticed a different behavior of the thermal relaxation time, t_w, as a function of the crust thickness, ΔR, with respect to known results in the literature [79], where $t_w \propto \Delta R^2$. We find that for neutron stars with densities at the base of the crust lower than 5×10^{13} g cm^{-3}, t_w decreases with increasing ΔR, while for densities larger than this value the traditional result is recovered. We concluded that in a very thin crust with a small or absent inner crust, some neutrino emission processes are blocked keeping the crust hotter for longer times. It is clear that the above result tell us that accurate observations of the relaxation phase of neutron stars would lead to valuable information on the properties of the crust which, in turn, as we have shown in this work give us information on the properties of the core-crust transition.

Conference presentations and submitted articles

Oral presentations and posters

1. The Relativistic Feynman Metropolis Teller Theory at zero and finite temperatures. Third Galileo-Xu Guangqi meeting, Beijing, China, 11th-15th October, 2011. (Poster)

2. Electrodynamics of Neutrons Stars. Erasmus Mundus School, Nice, France, 5th - 13th September, 2011. (oral presentation)

3. On the Relativistic Feynman-Metropolis-Teller Equation of state at Finite Temperatures and low densities White Dwarfs. Marcel Grossmann meeting, Stockholm, Sweeden, 1st - 7th July, 2012. (Oral presentation)

4. Relativistic Feynman-Metropolis-Teller Equation of state at Finite Temperatures. Erasmus Mundus School, Nice, France, 3rd âĂŞ 19th September, 2012. (Oral presentation)

5. The Relativistic Feynman-Metropolis-Teller Equation of state at Finite Temperatures and low densities White Dwarfs. Erasmus Mundus School, Nice, France, 3rd âĂŞ 19th September, 2012. (oral presentation)

6. On the cooling of neutron stars. Current Issues on Relativistic Astrophysics - November 5-6, 2012 - Seoul (South Korea) (oral presentation)

7. On the Relativistic Feynman-Metropolis-Teller treatment at Finite Temperatures and low densities White Dwarfs. Compact Stars in QCD phase diagram III- December 12-15, 2012 Guaruja, SP (Brazil) (oral presentation)

8. Finite Temperature Effects in the White Dwarf Structure in General Relativity. Texas Symposium- December 16-21, 2012 âĂŞ Sao Paulo (Brazil) (Poster)

9. Cooling of globally neutral neutron star. Erasmus Mundus School - Nice, 15-30 May 2013 (oral presentation)

10. On the cooling of globally neutral neutron stars. 1st URCA meeting on relativistic astrophysics - 24-29 June 2013, Rio de Janeiro, Brazil (oral presentation)

Proceedings

1. Title: The relativistic Feynmam-Metropolis-Teller theory at zero and finite temperatures. Authors: Sheyse Martins de Carvalho, Jorge A. Rueda, M. Rotondo, Carlos Arguelles, Remo Ruffini. International Journal of modern physics: conference series. In: Third Galileo-Xu Guangqi Meeting, 2011.

2. Title: On the Relativistic Feynman-Metropolis-Teller Equation of state at Finite Temperatures and low densities White Dwarfs. Authors: S. Martins de Carvalho, M. Rotondo, J. Rueda and R. Ruffini. In: XIII Marcel Grossmann Meeting, 2012.

Work in progress

1. Title: On the cooling of globally neutral neutron stars. Authors: S. M. de Carvalho, J. A. Rueda and R. Ruffini. Submitted to the Journal of the Korean Physical Society.

2. Title: The relativistic Feynman-Metropolis-Teller treatment at finite temperatures. Authors: S.M. de Carvalho, M. Rotondo, Jorge A. Rueda and R. Ruffini. Submitted to the Physical Review C.

3. Title: Thermal evolution of globally and locally neutral neutron stars. Authors: R. Negreiros, S. M. de Carvalho, J. A. Rueda and R. Ruffini. To be submitted to the Astronomy & Astrophysics.

Bibliography

[1] M. Rotondo, J. A. Rueda, R. Ruffini, and S.-S. Xue. Relativistic Thomas-Fermi treatment of compressed atoms and compressed nuclear matter cores of stellar dimensions. *Phys. Rev. C*, 83(4):045805, April 2011.

[2] P.-E. Tremblay, P. Bergeron, and A. Gianninas. An Improved Spectroscopic Analysis of DA White Dwarfs from the Sloan Digital Sky Survey Data Release 4. *ApJ*, 730:128, April 2011.

[3] R. Belvedere, D. Pugliese, J. A. Rueda, R. Ruffini, and S.-S. Xue. Neutron star equilibrium configurations within a fully relativistic theory with strong, weak, electromagnetic, and gravitational interactions. *Nucl. Phys. A*, 883:1–24, June 2012.

[4] G. Audi, A. H. Wapstra, and C. Thibault. The Ame2003 atomic mass evaluation (II). Tables, graphs and references. *Nuclear Physics A*, 729:337–676, December 2003.

[5] A. H. Wapstra and K. Bos. The 1977 Atomic Mass Evaluation: Parts I through III. *Atomic Data and Nuclear Data Tables*, 19:175–+, 1977.

[6] S. L. Shapiro and S. A. Teukolsky. *Black holes, white dwarfs, and neutron stars: The physics of compact objects*. 1983.

[7] T. Hamada and E. E. Salpeter. Models for Zero-Temperature Stars. *ApJ*, 134:683–+, November 1961.

[8] E. E. Salpeter. Energy and Pressure of a Zero-Temperature Plasma. *ApJ*, 134:669–+, November 1961.

[9] R. H. Fowler. On dense matter. *MNRAS*, 87:114–122, December 1926.

[10] E. C. Stoner. The limiting density of White Dwarfs. *Philosophical Magazine (Series 7)*, 7:63–70, 1929.

[11] S. Chandrasekhar. The Maximum Mass of Ideal White Dwarfs. *ApJ*, 74:81–+, July 1931.

[12] L. D. Landau. On the theory of stars. *Phys. Z. Sowjetunion*, 1:285–288, 1932.

[13] A. S. Eddington, Sir. On "relativistic degeneracy,". *MNRAS*, 95:194–206, January 1935.

[14] Y. I. Frenkel. *Zeit. fur Phys.*, 50:234, 1928.

[15] R. Ruffini. On the critical mass: the case of white dwarfs. In H. Gursky, R. Ruffini, & L. Stella, editor, *Exploring the universe: a Festschrift in honor of Riccardo Giacconi*, 2000.

[16] G. Bertone and R. Ruffini. Equilibrium configurations of relativistic white dwarfs. *Nuovo Cimento B Serie*, 115:935–+, July 2000.

[17] R. P. Feynman, N. Metropolis, and E. Teller. Equations of State of Elements Based on the Generalized Fermi-Thomas Theory. *Phys. Rev.*, 75:1561–1573, May 1949.

[18] L. D. Landau and E. M. Lifshitz. *Statistical physics. Part1*. Pergamon Press, Oxford, 1980.

[19] J. Ferreirinho, R. Ruffini, and L. Stella. On the relativistic Thomas-Fermi model. *Phys. Lett. B*, 91:314–316, April 1980.

[20] R. Ruffini and L. Stella. Some comments on the relativistic Thomas-Fermi model and the Vallarta-Rosen equation. *Phys. Lett. B*, 102:442–444, July 1981.

[21] P. A. M. Dirac. *Proc. Cambridge Phil. Soc.*, 26:376–+, 1930.

[22] A. B. Migdal, V. S. Popov, and D. N. Voskresenskiĭ. The vacuum charge distribution near super-charged nuclei. *Soviet Journal of Experimental and Theoretical Physics*, 45:436–+, March 1977.

[23] J. C. Slater and H. M. Krutter. The Thomas-Fermi Method for Metals. *Phys. Rev.*, 47:559–+, 1935.

[24] R. C. Tolman. Static Solutions of Einstein's Field Equations for Spheres of Fluid. *Physical Review*, 55:364–373, February 1939.

[25] J. R. Oppenheimer and G. M. Volkoff. On Massive Neutron Cores. *Phys. Rev.*, 55:374–381, February 1939.

[26] B. K. Harrison, M. Wakano, and J. A. Wheeler. *Onzieme Conseil de Physisque de Solvay*, 1958.

[27] M. Rotondo, J. A. Rueda, R. Ruffini, and S.-S. Xue. Relativistic Feynman-Metropolis-Teller theory for white dwarfs in general relativity. *Phys. Rev. D*, 84(8):084007, October 2011.

[28] K. Boshkayev, J. A. Rueda, R. Ruffini, and I. Siutsou. On General Relativistic Uniformly Rotating White Dwarfs. *ApJ*, 762:117, January 2013.

[29] J. Antoniadis, P. C. C. Freire, N. Wex, T. M. Tauris, R. S. Lynch, M. H. van Kerkwijk, M. Kramer, C. Bassa, V. S. Dhillon, T. Driebe, J. W. T. Hessels, V. M. Kaspi, V. I. Kondratiev, N. Langer, T. R. Marsh, M. A. McLaughlin, T. T. Pennucci, S. M. Ransom, I. H. Stairs, J. van Leeuwen, J. P. W. Verbiest, and D. G. Whelan. A Massive Pulsar in a Compact Relativistic Binary. *Science*, 340:448, April 2013.

[30] J. Antoniadis, M. H. van Kerkwijk, D. Koester, P. C. C. Freire, N. Wex, T. M. Tauris, M. Kramer, and C. G. Bassa. The relativistic pulsar-white dwarf binary PSR J1738+0333 - I. Mass determination and evolutionary history. *MNRAS*, 423:3316–3327, July 2012.

[31] A. Thorolfsson, O. E. Roegnvaldsson, J. Yngvason, and E. H. Gudmundsson. Thomas-Fermi Calculations of Atoms and Matter in Magnetic Neutron Stars. II. Finite Temperature Effects. *ApJ*, 502:847, August 1998.

[32] W. Stolzmann and T. Bloecker. Thermodynamical properties of stellar matter. I. Equation of state for stellar interiors. *A&A*, 314:1024–1040, October 1996.

[33] G. Chabrier and A. Y. Potekhin. Equation of state of fully ionized electron-ion plasmas. *Phys. Rev. E*, 58:4941–4949, October 1998.

[34] A. Y. Potekhin and G. Chabrier. Equation of state of fully ionized electron-ion plasmas. II. Extension to relativistic densities and to the solid phase. *Phys. Rev. E*, 62:8554–8563, December 2000.

[35] E. E. Salpeter and H. M. van Horn. Nuclear Reaction Rates at High Densities. *ApJ*, 155:183, January 1969.

[36] S. L. Shapiro and S. A. Teukolsky. *Black holes, white dwarfs, and neutron stars: The physics of compact objects*. 1983.

[37] L. R. Gasques, A. V. Afanasjev, E. F. Aguilera, M. Beard, L. C. Chamon, P. Ring, M. Wiescher, and D. G. Yakovlev. Nuclear fusion in dense matter: Reaction rate and carbon burning. *Phys. Rev. C*, 72(2):025806, August 2005.

[38] A. Y. Potekhin and G. Chabrier. Thermonuclear fusion in dense stars. Electron screening, conductive cooling, and magnetic field effects. *A&A*, 538:A115, February 2012.

[39] D. Koester. White Dwarf Spectra and Atmosphere Models. *arXiv:0812.0482*, December 2008.

[40] J. A. Panei, L. G. Althaus, and O. G. Benvenuto. Mass-radius relations for white dwarf stars of different internal compositions. *A&A*, 353:970–977, January 2000.

[41] D. Koester. Convective Mixing and Accretion in White Dwarfs. *A&A*, 52:415, November 1976.

[42] A. Y. Potekhin and G. Chabrier. Equation of state for magnetized Coulomb plasmas. *A&A*, 550:A43, February 2013.

[43] J. Antoniadis, P. C. C. Freire, N. Wex, T. M. Tauris, R. S. Lynch, M. H. van Kerkwijk, M. Kramer, C. Bassa, V. S. Dhillon, T. Driebe, J. W. T. Hessels, V. M. Kaspi, V. I. Kondratiev, N. Langer, T. R. Marsh, M. A. McLaughlin, T. T. Pennucci, S. M. Ransom, I. H. Stairs, J. van Leeuwen, J. P. W. Verbiest, and D. G. Whelan. *Science*, 340:6131, 2013.

[44] J. W. Negele and D. Vautherin. Neutron star matter at sub-nuclear densities. *Nuclear Physics A*, 207:298–320, June 1973.

[45] C. J. Pethick, D. G. Ravenhall, and C. P. Lorenz. The inner boundary of a neutron-star crust. *Nuclear Physics A*, 584:675–703, February 1995.

[46] P. Haensel, A. Y. Potekhin, and D. G. Yakovlev, editors. *Neutron Stars 1 : Equation of State and Structure*, volume 326 of *Astrophysics and Space Science Library*, 2007.

[47] M. Rotondo, Jorge A. Rueda, R. Ruffini, and S.-S. Xue. *Phys. Lett. B*, 701:667–671, 2011.

[48] R. L. Bowers, J. A. Campbell, and R. L. Zimmerman. Relativistic Many-Body Theory for Strongly Interacting Matter. *Phys. Rev. D*, 7:2278–2288, April 1973.

[49] R. L. Bowers, J. A. Campbell, and R. L. Zimmerman. Model Equation of State for Strongly Interacting Superdense Matter. *Phys. Rev. D*, 7:2289–2299, April 1973.

[50] H.-P. Duerr. Relativistic Effects in Nuclear Forces. *Physical Review*, 103:469–480, July 1956.

[51] J. D. Walecka. A theory of highly condensed matter. *Annals of Physics*, 83:491–529, 1974.

[52] J. A. Rueda, R. Ruffini, and S.-S. Xue. The Klein first integrals in an equilibrium system with electromagnetic, weak, strong and gravitational interactions. *Nucl. Phys. A*, 872:286–295, December 2011.

[53] J. Boguta and A. R. Bodmer. Relativistic calculation of nuclear matter and the nuclear surface. *Nuclear Physics A*, 292:413–428, December 1977.

[54] P. Ring. Relativistic mean field theory in finite nuclei. *Progress in Particle and Nuclear Physics*, 37:193–263, 1996.

[55] T. D. Lee and G. C. Wick. Vacuum stability and vacuum excitation in a spin-0 field theory. *Phys. Rev. D*, 9:2291–2316, April 1974.

[56] T. D. Lee and Y. Pang. Fermion soliton stars and black holes. *Phys. Rev. D*, 35:3678–3694, June 1987.

[57] R. Ruffini and S. Bonazzola. Systems of Self-Gravitating Particles in General Relativity and the Concept of an Equation of State. *Physical Review*, 187:1767–1783, November 1969.

[58] M. Rotondo, J. A. Rueda, R. Ruffini, and S.-S. Xue. Relativistic Thomas-Fermi treatment of compressed atoms and compressed nuclear matter cores of stellar dimensions. *Phys. Rev. C*, 83(4):045805–+, April 2011.

[59] G. A. Lalazissis, J. König, and P. Ring. New parametrization for the Lagrangian density of relativistic mean field theory. *Phys. Rev. C*, 55:540–543, January 1997.

[60] M. M. Sharma, M. A. Nagarajan, and P. Ring. Rho meson coupling in the relativistic mean field theory and description of exotic nuclei. *Physics Letters B*, 312:377–381, August 1993.

[61] Y. Sugahara and H. Toki. Relativistic mean-field theory for unstable nuclei with non-linear σ and ω terms. *Nuclear Physics A*, 579:557–572, October 1994.

[62] D. Hirata, H. Toki, and I. Tanihata. Relativistic mean-field theory on the xenon, cesium and barium isotopes. *Nuclear Physics A*, 589:239–248, February 1995.

[63] G. Baym, H. A. Bethe, and C. J. Pethick. Neutron star matter. *Nucl. Phys. A*, 175:225–271, November 1971.

[64] D. G. Yakovlev and C. J. Pethick. Neutron Star Cooling. *ARA&A*, 42:169–210, September 2004.

[65] Rodrigo Picanco Negreiros. Numerical Study of the Properties of Compact Stars (PhD thesis) . 2009.

[66] E. H. Gudmundsson, C. J. Pethick, and R. I. Epstein. Structure of neutron star envelopes. *ApJ*, 272:286–300, September 1983.

[67] K. Nomoto and S. Tsuruta. Cooling of young neutron stars and the Einstein X-ray observations. *ApJL*, 250:L19–L23, November 1981.

[68] A. Ray. Thermal conduction across neutron star crusts and cooling of young neutron stars. *Nuclear Physics A*, 356:523–532, March 1981.

[69] M. B. Richardson, H. M. van Horn, K. F. Ratcliff, and R. C. Malone. Neutron star evolutionary sequences. *ApJ*, 255:624–653, April 1982.

[70] O. Y. Gnedin, D. G. Yakovlev, and A. Y. Potekhin. Thermal relaxation in young neutron stars. *MNRAS*, 324:725–736, June 2001.

[71] D. G. Yakovlev, A. D. Kaminker, O. Y. Gnedin, and P. Haensel. Neutrino emission from neutron stars. *Phys. Rep.*, 354:1–155, November 2001.

[72] M. Prakash, M. Prakash, J. M. Lattimer, and C. J. Pethick. Rapid cooling of neutron stars by hyperons and Delta isobars. *ApJL*, 390:L77–L80, May 1992.

[73] A. D. Kaminker and P. Haensel. Neutrino emission due to electron bremsstrahlung in superfluid neutron-star cores. *Acta Physica Polonica B*, 30:1125–1148, April 1999.

[74] D. G. Yakovlev, A. D. Kaminker, O. Y. Gnedin, and P. Haensel. Neutrino emission from neutron stars. *Phys. Rep.*, 354:1–155, November 2001.

[75] D. Page and S. Reddy. Thermal and transport properties of the neutron star inner crust. *ArXiv e-prints*, January 2012.

[76] E. Flowers and N. Itoh. Transport properties of dense matter. III - Analytic formulae for thermal conductivity. *ApJ*, 250:750–752, November 1981.

[77] J. M. Ziman. "ordinary" Transport Properties and the Shape of the Fermi Surface. In W. A. Harrison and M. B. Webb, editors, *The Fermi Surface*, page 296, 1960.

[78] A. Y. Potekhin, G. Chabrier, and D. G. Yakovlev. Internal temperatures and cooling of neutron stars with accreted envelopes. *A&A*, 323:415–428, July 1997.

[79] J. M. Lattimer, K. A. van Riper, M. Prakash, and M. Prakash. Rapid cooling and the structure of neutron stars. *ApJ*, 425:802–813, April 1994.

[80] E. H. Gudmundsson, C. J. Pethick, and R. I. Epstein. Neutron star envelopes. *ApJL*, 259:L19–L23, August 1982.